MINETA NATIONAL TRANSIT RESEARCH CONSORTIUM

Electrical and Thermal Modeling of a Large-Format Lithium Titanate Oxide Battery System

MNTRC Report 12-32

MNTRC
MINETA NATIONAL TRANSIT RESEARCH CONSORTIUM

PENNSTATE
1855

MINETA TRANSPORTATION INSTITUTE
LEAD UNIVERSITY OF MNTRC

The Norman Y. Mineta International Institute for Surface Transportation Policy Studies was established by Congress in the Intermodal Surface Transportation Efficiency Act of 1991 (ISTEA). The Institute's Board of Trustees revised the name to Mineta Transportation Institute (MTI) in 1996. Reauthorized in 1998, MTI was selected by the U.S. Department of Transportation through a competitive process in 2002 as a national "Center of Excellence." The Institute is funded by Congress through the United States Department of Transportation's Research and Innovative Technology Administration, the California Legislature through the Department of Transportation (Caltrans), and by private grants and donations.

The Institute receives oversight from an internationally respected Board of Trustees whose members represent all major surface transportation modes. MTI's focus on policy and management resulted from a Board assessment of the industry's unmet needs and led directly to the choice of the San José State University College of Business as the Institute's home. The Board provides policy direction, assists with needs assessment, and connects the Institute and its programs with the international transportation community.

MTI's transportation policy work is centered on three primary responsibilities:

Research

MTI works to provide policy-oriented research for all levels of government and the private sector to foster the development of optimum surface transportation systems. Research areas include: transportation security; planning and policy development; interrelationships among transportation, land use, and the environment; transportation finance; and collaborative labor-management relations. Certified Research Associates conduct the research. Certification requires an advanced degree, generally a Ph.D., a record of academic publications, and professional references. Research projects culminate in a peer-reviewed publication, available both in hardcopy and on TransWeb, the MTI website (http://transweb.sjsu.edu).

Education

The educational goal of the Institute is to provide graduate-level education to students seeking a career in the development and operation of surface transportation programs. MTI, through San José State University, offers an AACSB-accredited Master of Science in Transportation Management and a graduate Certificate in Transportation Management that serve to prepare the nation's transportation managers for the 21st century. The master's degree is the highest conferred by the California State University system. With the active assistance of the California Department of Transportation, MTI delivers its classes over a state-of-the-art videoconference network throughout the state of California and via webcasting beyond, allowing working transportation professionals to pursue an advanced degree regardless of their location. To meet the needs of employers seeking a diverse workforce, MTI's education program promotes enrollment to under-represented groups.

Information and Technology Transfer

MTI promotes the availability of completed research to professional organizations and journals and works to integrate the research findings into the graduate education program. In addition to publishing the studies, the Institute also sponsors symposia to disseminate research results to transportation professionals and encourages Research Associates to present their findings at conferences. The World in Motion, MTI's quarterly newsletter, covers innovation in the Institute's research and education programs. MTI's extensive collection of transportation-related publications is integrated into San José State University's world-class Martin Luther King, Jr. Library.

REPORT 12-32

ELECTRICAL AND THERMAL MODELING OF A LARGE-FORMAT LITHIUM TITANATE OXIDE BATTERY SYSTEM

Timothy Cleary, M.S.
Harshad Kunte, M.S.
Jim Kreibick

April 2015

A publication of

**Mineta National Transit
Research Consortium**

College of Business
San José State University
San José, CA 95192-0219

TECHNICAL REPORT DOCUMENTATION PAGE

1. Report No. CA-MNTRC-14-1150	**2. Government Accession No.**	**3. Recipient's Catalog No.**

4. Title and Subtitle Electrical and Thermal Modeling of a Large-Format Lithium Titanate Oxide Battery System	**5. Report Date** April 2015 **6. Performing Organization Code**
7. Authors Timothy Cleary, M.S., Harshad Kunte, M.S., and Jim Kreibick	**8. Performing Organization Report** MNTRC Report 12-32
9. Performing Organization Name and Address Mineta National Transit Research Consortium College of Business San José State University San José, CA 95192-0219	**10. Work Unit No.** **11. Contract or Grant No.** DTRT12-G-UTC21
12. Sponsoring Agency Name and Address U.S. Department of Transportation Office of the Assistant Secretary for Research and Technology (OST-R), University Transportation Centers Program 1200 New Jersey Avenue, SE Washington, DC 20590 The Thomas D. Larson Pennsylvania Transportation Institute Pennsylvania State University 201 Transportation Research Building University Park, PA 16802-4710	**13. Type of Report and Period Covered** Final Report **14. Sponsoring Agency Code**

15. Supplemental Notes

16. Abstract

The future of mass transportation is clearly moving towards the increased efficiency of hybrid and electric vehicles. Electrical energy storage is a key component in most of these advanced vehicles, with the system complexity and vehicle cost shifting from combustion engines to battery and electric drive systems.

To assist engineers and technicians in this transfer, the Battery Application Technology Testing and Energy Research Laboratory (BATTERY) of the Thomas D. Larson Pennsylvania Transportation Institute in the College of Engineering at The Pennsylvania State University partnered with an advanced bus manufacturer to study lithium titanate oxide battery chemistry for use in transit buses. The research team found, other than proprietary data/models, scant technical information or research on electrical and thermal modeling of this advanced chemistry.

The research team developed lithium titanate oxide modules to study their characteristic behaviors and produce state-of-charge estimators capable of running on the limited embedded processing power and memory of a typical battery management system. The team also investigated the thermal performance of this chemistry in the large format, producing a physics-based empirical thermal model for use in system-level simulations. This model predicts pack-level thermal behavior by reporting the minimum, maximum, and average temperatures within a system typically used for large automotive applications, as testing was concentrated on transit bus usage profiles.

This work supports battery system integration and management. The tools produced are intended to assist automotive engineers to achieve optimal system performance and ultimately a more efficient vehicle.

17. Key Words Lithium-Titanate-Oxide (LTO); State-of-Charge (SOC); Thermal management; Liquid cooling; LTO characterization	**18. Distribution Statement** No restrictions. This document is available to the public through The National Technical Information Service, Springfield, VA 22161

19. Security Classif. (of this report) Unclassified	**20. Security Classif. (of this page)** Unclassified	**21. No. of Pages** 91	**22. Price** $15.00

Form DOT F 1700.7 (8-72)

Library of Congress Catalog Card Number:
2015933910

To order this publication, please contact:

Mineta National Transit Research Consortium
College of Business
San José State University
San José, CA 95192-0219

Tel: (408) 924-7560
Fax: (408) 924-7565
Email: mineta-institute@sjsu.edu

transweb.sjsu.edu/mntrc/index.html

ACKNOWLEDGMENTS

This report and the supporting work were sponsored by the Mineta National Transit Research Consortium (MNTRC) under a University Transportation Centers grant from the U.S. Department of Transportation Research and Innovative Technology Administration (RITA), with matching equipment, supplies, and personnel time provided by a manufacturer of advanced buses.

The Pennsylvania State University's Thomas D. Larson Pennsylvania Transportation Institute administratively supported this work by making facilities and personnel available. The Larson Institute research team expresses special thanks to David Klinikowski, director of the Larson Institute's Federal Transit Administration-sponsored Bus Research and Testing Center, for his oversight and guidance during this project, and to Dennis Kovalick, manager of the Penn State test track, and the bus testing personnel for their assistance in configuring the vehicle testing lab at the test track to accommodate the research. Thanks also to professor Chris Rahn and senior research associate Joel Anstrom of the Larson Institute's Vehicle Systems and Safety Program, who supplied technical guidance during this project.

The Larson Institute-administered Mid-Atlantic Universities Transportation Center earlier assisted the researchers to acquire a walk-in, temperature- and humidity-controlled chamber, which proved useful in the research and will support future endeavors at Penn State.

The research team also thanks MNTRC executive director Karen Philbrick, Ph.D., for her leadership and guidance; communications director Donna Maurillo, MSTM, for public outreach and for additional editorial support; research coordinator Joseph Mercado for publication support; and Frances Cherman for website support.

TABLE OF CONTENTS

LIST OF FIGURES

EXECUTIVE SUMMARY

Electrical energy storage is a key component in many of today’s advanced vehicles. Lithium titanate offers considerable power density along with high stability and long cycle life relative to other carbon-based lithium battery systems. To assist engineers in implementing lithium titanate battery systems into heavy vehicles, the Penn State research team, with support from MNTRC and research sponsors, tested a system and presented the resulting data and models.

This report covers the electrical and thermal characterization of large-format lithium titanate battery systems, including the test setup, testing procedures, and analysis used to develop and validate electrical and thermal models. The electrical model includes a voltage response and improved state-of-charge estimator that can be deployed on a relatively low-cost embedded system. The thermal model is intended for off-vehicle simulations, yet with further development, it can support onboard advanced thermal management.

During the testing and early analysis, a sensor sensitivity study was also performed. This work presents a quantifiable measure of estimation error due to poor sensor accuracy and its effects on commonly used state-of-charge estimators.

I. INTRODUCTION

This report was written for a broad audience, covering the introduction to battery systems and management of these systems, as well as some of the detailed analysis required to properly integrate and control advanced-chemistry electrical energy storage systems.

After an introduction to the test setup and typical management systems, the report primarily covers a sensitivity study and engineering systems-level investigation into some of the problems faced by battery systems. It then shows the procedure and analysis performed to solve some of these problems. Specifically, the testing and analysis were planned to develop an equivalent circuit, dual polarization model, then to use an extended Kalman filtering and voltage observer to improve state-of-charge estimation followed by physic-based, empirical thermal modeling. This results in a module capable of looking forward and predicting minimum, maximum, and average temperatures within the battery system based on expected electrical loading.

A battery management system is necessary to safely operate a vehicle with large onboard electrical energy storage including hundreds of cells. For the long-term success of electric and hybrid electric vehicles using this chemistry, it is necessary to educate the workforce responsible for the design, integration, and maintenance of these high-power/high-energy systems. This work was designed to support that education effort.

II. TEST SETUP

The research team performed all testing within the Battery Application Technology Testing and Energy Research Laboratory (BATTERY) facilities at the Thomas D. Larson Pennsylvania Transportation Institute (Larson Institute) of the College of Engineering at The Pennsylvania State University's (Penn State) University Park campus.

Initially, the team investigated its existing laboratory equipment. They performed an evaluation to determine if the electrical and thermal loading necessary to characterize the battery under test conditions could be performed using this equipment. The research partners also performed a study investigating the particular sensitivities to measurable parameters. As a result, they determined the required thermal and electrical sensor resolutions. Equipment and measurement devices were appraised. Finally, to prepare for testing, the research team calibrated and purchased new equipment.

This section of the report details the equipment and laboratory configuration used during the research.

LTO BATTERY PACK AND MODULE

The research team's industry partner donated a full-scale, eight-module, 50-ampere hours (Ah) lithium titanate oxide (LTO) battery pack and a single 50-Ah module with custom battery management system (BMS). The modules in the pack and the separate module were identical and assumed to be at 100 percent state of health (SOH) upon delivery.

Single Module

A ten-cell LTO module with heat sink was used for module-level research. This module is made of ten prismatic LTO cells, all in a series configuration. Each identical cell is designed to have 50 Ah of capacity and a nominal voltage of 2.3 Volts (V) direct current (DC), resulting in a module nominal voltage of 23 VDC. The research team limited maximum and minimum system currents to +/- 300 amperes continuous and +/- 500 amperes peak (ten-second pulses), remaining within the manufacturer's recommended use. The physical arrangement of these cells within a module can be described as a stacked system. Cells are stacked on top of one another, with heat sink material distributed between select cells and ultimately connected to a short sidewall of the module. The short sidewall serves as the module heat sink and is opposite the cell and module terminals. With both terminals located on the same short sidewall of the prismatic cell, a concentration of heat on this terminal side due to increased current densities is expected. The module measures approximately 25.3 kg in weight and 280 mm x 305 mm x 155 mm in length, width, and height. With a measured capacity of 47.8 Ah @ 50 A, and 23 VDC nominal voltage, the module has a calculated energy density of 43.5 Wh/kg.

Eight-Module LTO Battery Pack

The donated battery pack contains eight series modules identical to the single module detailed above. With an eight-module series configuration, the resulting nominal pack voltage is 184 VDC with a rated capacity of 50 Ah or 9.2 kilo-Watt hours (kWh). Cooling this pack is achieved simply by convection from a module heat sink to a liquid-cooled pack heat sink. Heat generated within the battery pack is then dissipated by way of a laboratory cooling system plumbed to the pack.

AEROVIRONMENT POWER PROCESSORS

Power cycling of each battery system was performed using one of two AeroVironment power processing machines. The AV900, a 250-kW machine, was used for pack-level testing, while an ABC150, a 125-kW machine, was used for module-level testing.

AV900

The AeroVironment AV900 was selected for pack-level testing, as it is easily capable of the high powers required to fully exercise the eight-module/80-cell pack. Figure 1 shows the AV900 machine used during this research. With testing never exceeding the recommended current limitation of 300A, the maximum required power-under-pulse power testing was approximately 67.2 kW. With a maximum allowable cell voltage of 2.8 VDC, the maximum required power is determined by the following calculation.

$$MaxPower = Max\ Cell\ Voltage\ \ x\ \ \#\ cells\ \ x\ \ Max\ Current \tag{1}$$

ABC150

An AeroVironment ABC150 power processing machine was selected for use in module-level testing. This machine is capable of 125 kW. With a maximum module voltage of 28 VDC and maximum charge/discharge current of 300 A, the required power is well within the machine’s capabilities.

Each of these machines is controlled by either an automatic or manual mode. In automatic mode, the resident AeroVironment software, using a programming script, was relied on to automate the electrical loading profile. When the machines were in a manual mode, researchers used the machines’ face screens and manual PC interface to select mode (current, voltage, or power) and value of the required loading. These machines are capable of accepting dynamic commands for current, voltage, or power with a rather fast 0.25-second full power ramp rate.

Figure 1. AV900

ENVIROMENTAL TESTING CHAMBER

This study involved a variety of environmental loading conditions to accurately characterize the system and to extract modeling parameters. To maintain these various conditions, a temperature-controlled chamber was required with the volume and range to cover the operation span of LTO cells as well as the typical North American climate. The team had earlier worked to procure such a walk-in, temperature- and humidity-controlled chamber.

This ESPEC EWPX499-6CAL chamber is capable of controlling temperature from -65˚ to 85˚ Celsius with reasonable fluctuations and gradients. Although this study did not require controlling humidity, the team believes future work involving BMS research and evaluation will require this ability.

Figure 2. Temperature-Controlled Test Chamber

After the test chamber installation (Figure 2) was complete, immediate progress was made to install sensors and supporting equipment. Figure 3 shows the eight-module battery pack under test, with heat lamps generating a simulated hot road surface.

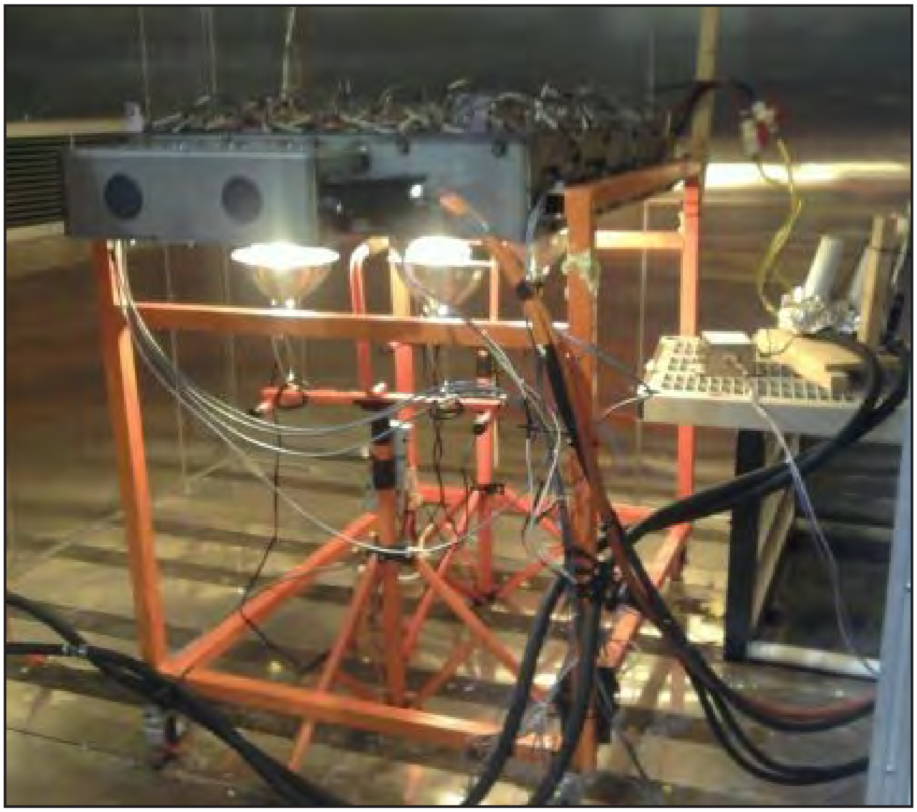

Figure 3. Heat Lamp Setup inside Test Chamber

Full insulation of the battery system was required for some testing, such as specific heat value investigations and the determination of heat transfer coefficients. A module-level example of this can be seen in Figure 4.

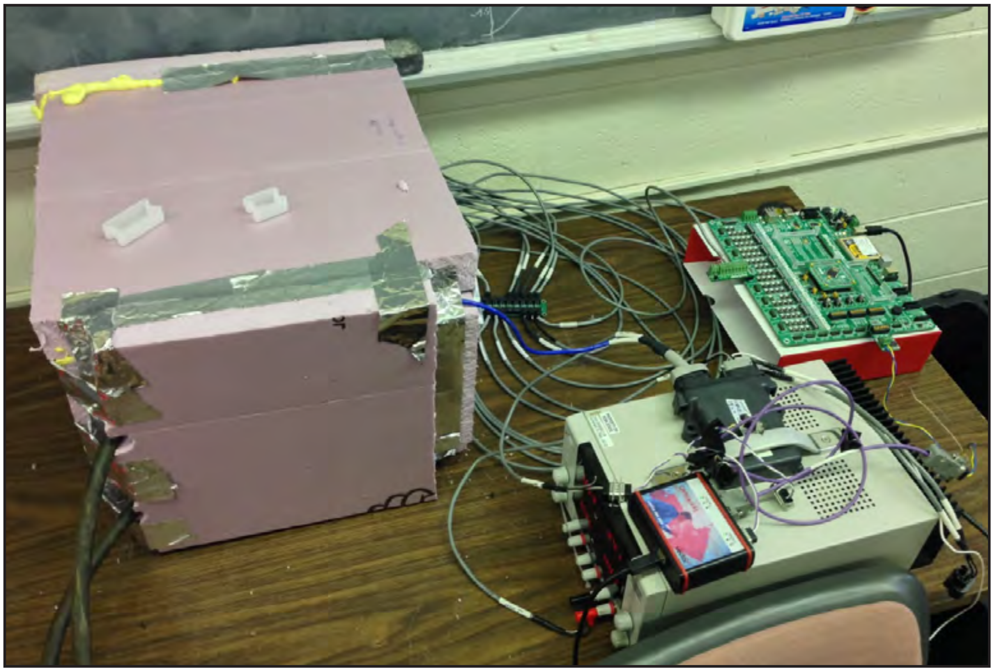

Figure 4. Insulated Module Test Setup

VOLTAGE AND CURRENT SENSORS

The full battery system tested was capable of measuring its own voltage and current values. To verify these values and offer independent evaluation, however, high-accuracy sensors were chosen based on the sensitivity study performed prior to testing.

A closed-loop inductive transducer was selected to obtain a high level of confidence in current sensor accuracy. Many different sensors were evaluated, but the LEM CAB 300 was selected for the low linearity error and for its system integration benefits. This particular sensor communicates measurements digitally using a controller area network (CAN) instead of using the typical analog voltage or current signal. This CAN node sensor performed the conversion to a digital signal locally before broadcasting its reading, in turn reducing the number of long analog measurement sense lines between the data acquisition system and the sensor.

A voltage LEM CV3-500 voltage transducer was selected to achieve an independent measure of voltage similar to the CAB300 current sensor. This voltage transducer generates a low-voltage DC signal that is then measured by one of the laboratory's xPC system's analog input channels. Figure 5 shows the two CAB300 current sensors and CV3-500 voltage transducer housed in a high-voltage-rated enclosure. Although both the battery system and AeroVironment systems measure only one current, the high-voltage sensor cabinet contains two current sensors, one for each pole, to decrease measurement error.

Beyond the LEM CAB 300 current sensor and LEM CV3-500 voltage transducer, both the battery pack and AeroVironment components measure and broadcast current and voltage readings on a CAN bus.

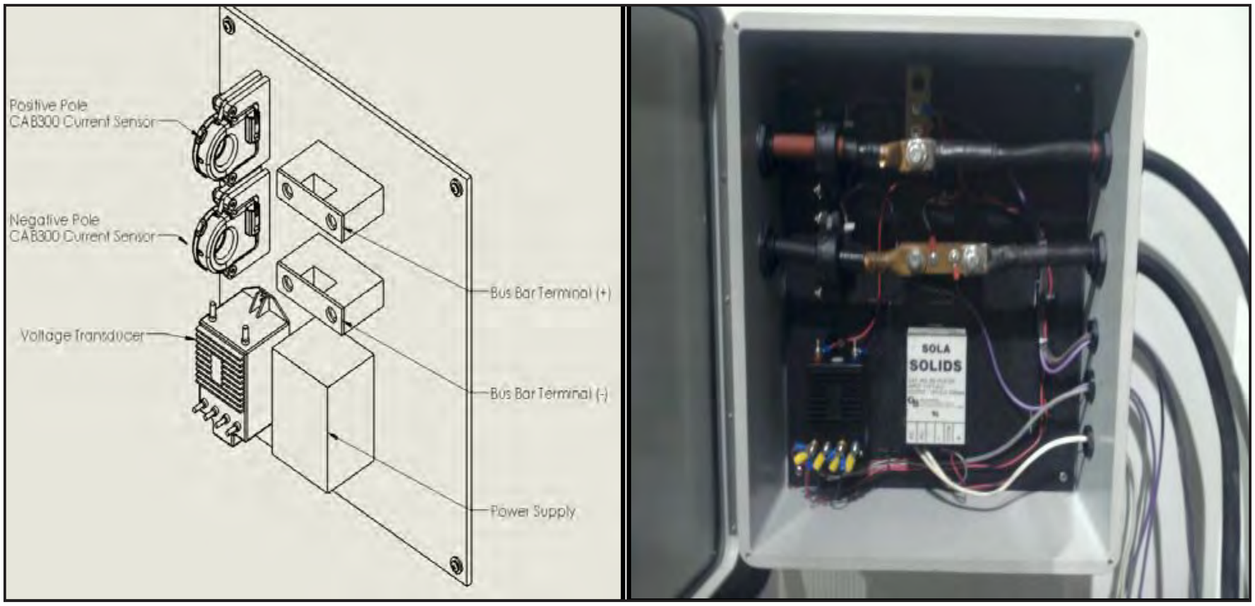

Figure 5. High Voltage Sensor Cabinet

SURFACE TEMPERATURE SENSORS

A main research objective was to provide an accurate and validated thermal model of the large-format LTO modules under test. To monitor the battery system's minimum/maximum and gradient temperatures, it was necessary to distribute multiple sensors throughout the battery pack. Temperature sensor resolution and accuracy were key components in the sensor/model sensitivity study. The research team determined that Maxim DS18B20 single-wire temper sensors met requirements for measuring the module surface temperature in the sensitivity study.

The research team added eight surface-mount DS18B20 single-wire digital temperature sensors to each module. Combined with the three manufacturer-installed temperature sensors embedded within each module, the eight-module battery pack contained a total of 88 temperature sensors.

The DS18B20 sensors provide 12-bit readings in a -55 to 125˚C range, resulting in a resolution of 0.044˚C (Maxim Integrated, 2008). Digital communication and each temperature sensor's unique 64-bit ROM value serial code allowed for a large string of sensors on the same one-wire bus. This simplified integration and data acquisition. At a battery pack level, there were 64 temperature sensors, eight per module, secured to the top and heat sink side of each module. These additional 64 sensors are shown to provide an adequate surface temperature profile during thermal testing. To ensure that each temperature sensor was attached with the same thermal contact resistance, a 3M PTFE thermally conductive adhesive tape with high electrical insulation resistance was utilized for each sensor location.

LIQUID COOLING SYSTEM

The liquid-cooled battery pack under test required a system to pump liquid and to dissipate heat from electrical loading of the cells. In the process of mapping the thermal and electrical performance of the LTO modules, controlled heat extraction and monitoring was necessary.

A 50/50 mix of ethylene glycol and distilled water was used to fill the liquid system, which included the liquid-cooled heat sink within the pack and heat extraction system (Figure 6). The heat extraction system is composed of an electronic pump, forced-air-cooled radiator, and flow meter device. An EMP WP29 electronic, CAN controlled liquid pump was selected for its ability to operate at a wide range of speeds and loads as well as its speed control response and stability. Then a standard forced-air-cooled radiator was added to dissipate heat into ambient air. Finally, a FTP4705 flow meter with square wave output was used to allow for closed-loop control of liquid flow. The pump and flow meter are controlled and monitored by the laboratory xPC machine.

Figure 6. Heat Extraction System

Pack-level heat generation data were collected using two resistance temperature detectors (RTD) at the entrance and exit of the LTO pack. These sensors were determined to be the most sensitive, requiring the highest resolution of the temperature sensors in this setup during the sensitivity study. The platinum RTDs used in this setup have the high accuracy and precision required to properly capture the small temperature delta resulting from relatively low heat generation and a weak heat extraction system.

Each of the RTD sensors was fully emerged in the flowing liquid coolant using a Thermowell assembly. A filtering amplifier with CAN communication was used to measure RTS resistance and broadcast the scaled temperature data. The non-insulated RTDs and Thermowell setup can be seen in Figure 7. Note that during thermal testing, these sensors and coolant lines were fully insulated to ensure minimal heat transfer between the liquid and the controlled environment of the test chamber.

Figure 7. RTD Setup on Heat Extraction System

DATA ACQUISITION AND TESTING AUTOMATION

Data acquisition and testing automation are accomplished primarily through CAN communication. This is a common serial communication interface used in automotive applications. Many of the components used in this research, including the industry partner-provided BMS, were already set up for this interface. Each component is either directly or indirectly connected to one of the laboratory's CANs. For the components without their own CAN node, the xPC (Mathworks) machine serves as a gateway. The xPC machine was also used, with compiled Simulink® (Mathworks) code, to control the electronic pump, maintaining a constant flow rate. This setup used the pump and flow meter to perform closed-loop control of the liquid flow rate through the pack.

Vector hardware and software were used to record, monitor, and control all systems of the test setup. A Vector CANtech VN1630 unit with high-speed supported hardware and CANoe software (Vector CANtech, Inc.) was used with a Microsoft Windows 7 Professional PC, while compiled Simulink® code ran on another PC system in the laboratory. Figure 8 lists the four CAN channels used during testing and the components on each channel. Note that the components not listed here – for example, the flow meter and voltage transducer – are part of the xPC machine's analog or digital input channels. The xPC machine then broadcasts the scaled data, such as flow rate and pack voltage, to be recoded on the CAN bus. The VN1630 four-channel unit and Windows 7 PC were used to log all CAN traffic, thus acting as the logging device for all data, equipment, and tests.

Channel	Bus Speed	Equipment on Bus
1	125 kbps	LTO Pack, AV900, xPC Machine
2	500 kbps	CAB 300 Positive Pole
3	250 kbps	RTD Scanner, EMP W29 Pump
4	500 kbps	CAB 300 Negative Pole, 18B20 Temperature Scanner

Figure 8. Laboratory CAN Bus Channels

Because of the various bus speeds and conflicting CAN IDs, several channels were required to record all test data. One four-channel VN1630 device was used to record all four channels of CAN data, all on the same time scale.

Before each test, the laboratory PCs were verified to be recoding and controlling as intended. During testing, these machines controlled the programmed test and displayed real time data to the research group. At the end of each test, data were archived to the local machines and an offsite secure server maintained by Penn State.

As discussed above, AeroVironment Remote Operating System (ROS) was relied upon to automate the testing and electrical loading of the pack under test. The details of each test, including capacity, Hybrid Pulse Power Characterization (HPPC), and Federal Urban Dynamometer schedule (FUDS), and the functions used within each, can be found in Appendix A – AeroVironment Test Scripts and Functions.

III. BATTERY MANAGEMENT SYSTEM SOC ESTIMATION

BATTERY MANAGEMENT SYSTEMS

A Battery Management System (BMS) is an embedded device with sensors and actuators dedicated to ensuring the safe and optimal operation of a battery. When advanced chemistry electrical energy storage systems are integrated in heavy vehicles, the BMS serves as the component controller, similar to an engine control unit or automatic transmission controller of a conventional vehicle. A BMS is integrated into the vehicle's control system and communicates summary battery data supporting vehicle decisions. For example, a series hybrid may start or stop its engine-generator system or auxiliary power unit based on data received from the battery system. In the case of a pure electric vehicle, the fuel gauge would be replaced by data generated by the BMS.

Another feature often integrated into the BMS is the ability to track battery use and recommend maximum available loading to assist in the battery's longevity. Vehicle manufacturers and transit authorities, among others, are interested in the most fuel-efficient and cost-effective means of transporting passengers. Electric and hybrid electric vehicles offer unique opportunities to manage and recapture energy. Although each system and vehicle route has a unique optimal solution, a vehicle and its component controllers can be continually striving for the most efficient performance.

As with many electronic control systems, a BMS can be broken down into its two key components, hardware and software.

Hardware

To access real-world parameters a BMS utilizes voltage, current, and temperature sensors distributed throughout the battery system. Typically, a voltage sensor is attached to each cell or virtual cell, which consists of multiple cells grouped together in parallel forming one series element. Paralleling cells is often done to increase battery system capacity and available power, effectively multiplying these parameters by each parallel cell.

While each series string of cells may have a current sensor, it is typically necessary for at least the overall system's current to be measured, especially when SOC estimation is critical.

Temperature sensors are usually distributed throughout the pack and should be located in sensitive areas, close to the highest source of heat generation.

Typically, a BMS will have at least one supervisory controller and distributed systems. These distributed systems are usually the devices measuring cell voltages and temperatures and reporting this information back to the supervisory controller over a digital interface, some form of serial communication such as RS232, RS485, or CAN. The distributed device will also balance a cell by either shorting a resistor across its terminals to slowly drain a high cell (an example of a passive management system), or in a more efficient use of energy, shuttling charge from high cells to low cells. Likely, a relatively small central energy storage buffer would also be common among these distributed devices.

Software

BMS hardware is rather straightforward, but that is not the case when it comes to the software managing cell balance or predicting state-of-charge and state-of-health.

At its core, a BMS will monitor cell voltages, pack or string current, and various temperature sensors. All these data are then fed to the supervisory control system, which in turn makes decisions about which cells to balance and whether to keep the high-power connection to the outside systems enabled/disabled (circuit open or closed), while also determining an estimation of SOC. Advanced systems even estimate SOH based on usage tracked over the life of the system or intentions charge/discharge power acceptance limits to maintain maximum longevity of the system.

The means for determining which cells to actively balance are based either on the average and outlying voltage measurements or, in an advanced system, on averaged and outlying SOC estimations. In chemistries with very flat charge/discharge curves, making the balancing decision becomes difficult when only cell voltage data are available. For this reason and to determine real-time available energy, SOC prediction is utilized.

Several methods can be employed for predicting a battery’s SOC. Rarely is it possible to measure it during operation, so a prediction or estimation is necessary for most applications. This report presents some of the common and advanced methods for estimating SOC, then it applies them to the tested LTO battery. Improvements in SOC estimation also assist in the effort to improve SOH estimations in advanced systems.

BATTERY CHARACTERIZATION

This report investigates lithium titanate oxide battery chemistry by studying ten-cell modules in an eight-series module and a single-module configuration. The cells in each of these battery systems are configured in series. No parallel-cell modules or packs were used in this research. Using an eight-series module system, the research team performed testing to capture an initial characterization of this chemistry. These tests included capacity, USABC Hybrid Pulse Power Characterization, and Federal Urban Dynamometer schedule testing at various controlled ambient temperatures ranging from -20° to 40° Celsius. The researchers performed capacity tests over a range of constant current values including 50, 150, and 300 amperes, while HPPC tests followed the USABC manuals as closely as possible.

The results of these tests are presented and analyzed in the following sections.

SOC PREDICTION METHODS

State-of-charge is the percentage of battery capacity remaining relative to the same fully charged battery. Depth of discharge (DOD) is similar but indicates the percentage of capacity that has been removed from a battery, again relative to a fully charged battery. SOC is analogous to the term “glass half-full,” while DOD is “glass half-empty.” These are critical parameters for users sensitive to an energy storage system’s instantaneous capacity. Yet an accurate SOC value cannot be determined without some understanding of a battery system's SOH. Some of the following SOC estimation methods perform better than others given the variance in capacity and power acceptance. These variances are difficult to distinguish in real time but are based on either battery age or environmental conditions. This section will present two common methods of estimating SOC that are often combined, open circuit voltage (OCV) mapping and Coulomb counting. This section will then present the application of a Kalman filtering method, including a Luenberger observer, and ultimately a validated equivalent circuit model (ECM) in combination with an extended Kalman filter, as the resulting ECM shows non-linearity.

Voltage

SOC can be determined based solely on a pack voltage measurement. This method is the simplest but most inaccurate, especially for advanced lithium chemistries such as LTO. This method uses OCV, which is a fixed map of voltage versus SOC. This map is populated with data gathered during a low C-rate discharge, making the assumption that the low C-rate causes an equivalent Ohmic voltage drop that is negligible. These data also present a profile in which the limits of a battery's voltage at maximum and minimum SOC, as well as the indexed SOC between, can be determined.

The research team performed a 1C discharge to determine the LTO pack's OCV map. Figure 9 indicates that the pack under test has a maximum voltage of 212.70 and minimum voltage of 161.2 based on the exponential zones at each end of the cycle defining the limitations. Dividing the time between the start and finish into ten equal sections and noting the voltage at each interval generates an OCV map for 10 percent steps in SOC.

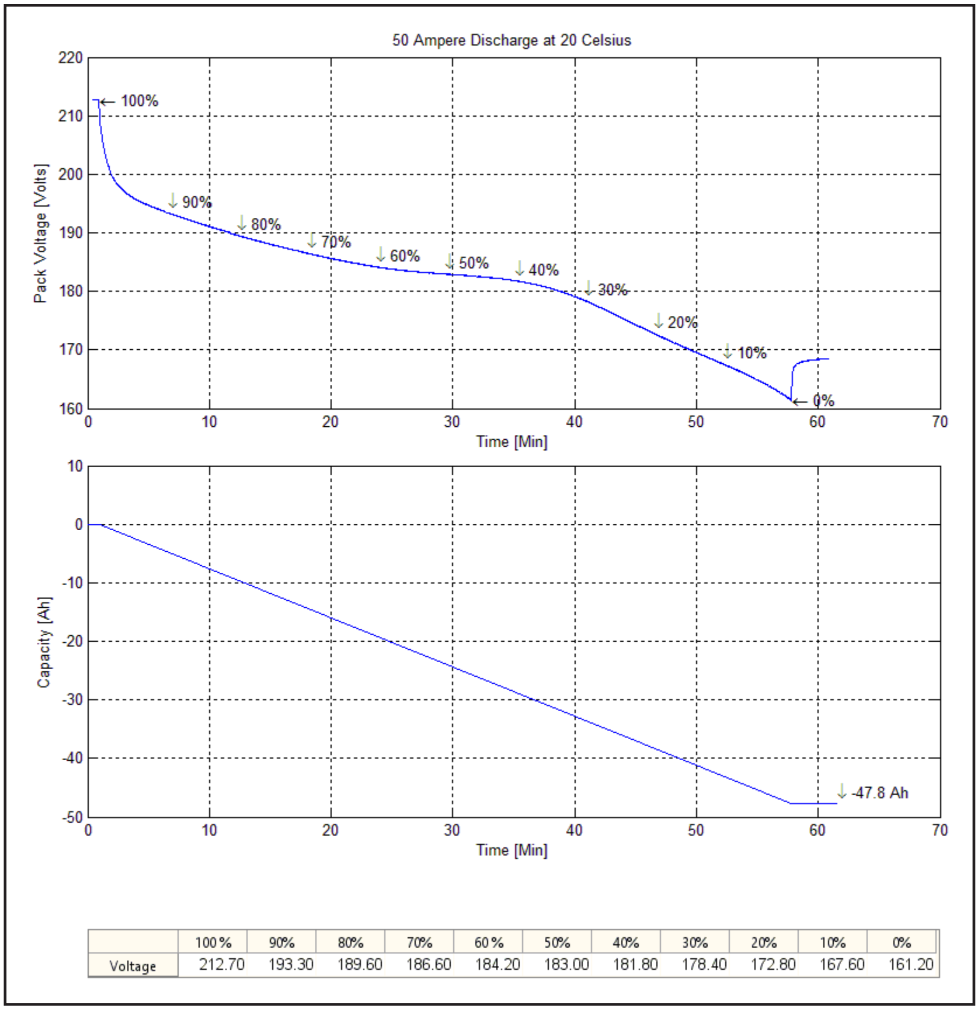

	100 %	90%	80%	70%	60 %	50%	40%	30%	20%	10%	0%
Voltage	212.70	193.30	189.60	186.60	184.20	183.00	181.80	178.40	172.80	167.60	161.20

Figure 9. Discharge (1C) to Determine OCV and Capacity

Using an OCV map is reasonable only after a substantial time without loading the system. Even at that point, an OCV map is not reliable, as the variance in voltage measurements, especially in the flat area of the voltage curve, is sensitive to inaccuracy due to the small change in voltage relative to SOC. Typically this is used only after a several-minute period at or below a negligible load. Because an OCV map is developed using low C-rate loading, it is accurate only at low or no loading. A feasible but complicated option is sometimes used. This involves defining several voltage curve maps at various loading conditions or even a simple series resistance model. However, as the battery ages, these values will be increasingly inaccurate. As SOH decreases and effective series resistance (ESR) grows, the voltage drop under load will be greater for each loading scenario.

Figure 10 shows three different discharge rates and the associated voltage curves. Note that the variation in system capacity at these three rates is greater than 10 percent over a 50-, 100-, and 150-ampere discharge. This variation is not captured even with multiple OCV maps.

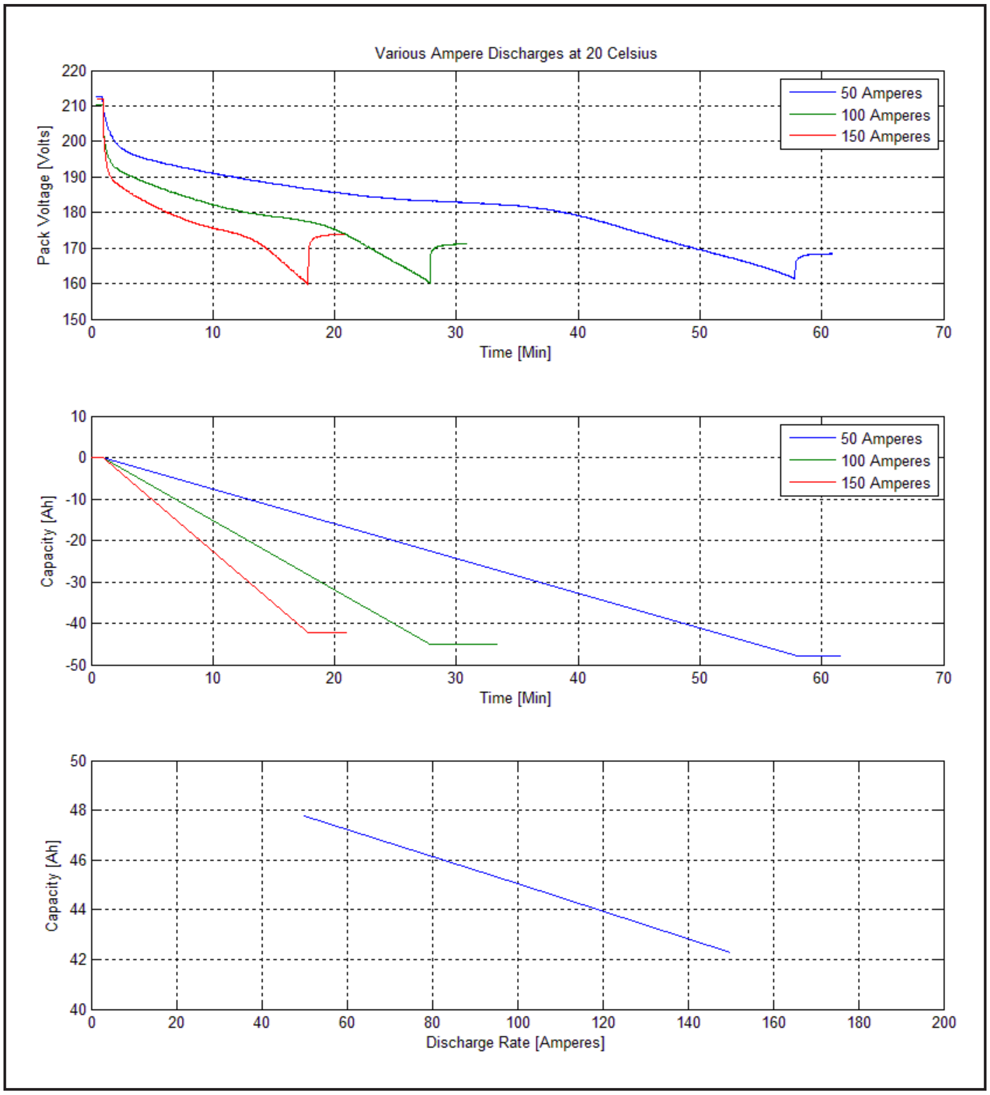

Figure 10. Various Constant Current Discharge Rates

Coulomb Counting

Coulomb counting is the integration of current over time to determine an estimate for SOC. In its simplest form, it involves only integration of current, but in practice, corrections to this estimate are performed based on a relaxed voltage. The combined current/voltage method relies on the accuracy of pack current and voltage sensors as well as an assumption of pack capacity. Initial and corrected values are determined by referencing an OCV table. The conditions of this reference are limited by the same issues presented above in the voltage-only method.

Capturing the variation in capacity shown in Figure 10 due to loading and adapting for various Ohmic voltage drops is not possible with simple OCV or even Coulomb counting.

Luenberger Observer

As seen earlier, techniques such as Coulomb counting and voltage lookup, while easy to understand and implement, are severely limited in capability and accuracy. These techniques suffer from a few key drawbacks.

As previously stated, Coulomb counting and voltage lookup methods are very sensitive to noise on the current and voltage sensors. Good quality filtering of the current/voltage signal is required to overcome this issue. On several occasions, this results in lower accuracy because of inaccuracies induced by filtering current. In turn, this results in SOC estimation inaccuracies.

Also, the accuracy of these methods during a given operating session depends heavily on the accuracy of the initial value of estimated SOC, typically determined using the OCV method discussed above. If the initial values are incorrect, the estimate continues to diverge further.

Finally, voltage lookup can be based only on terminal voltage measured during vehicle operation. However, most voltage versus SOC data is available with OCV instead of terminal voltage, as discussed above. Obtaining the OCV from the terminal voltage during vehicle operation is difficult and severely prone to errors. It requires an accurate real-time measurement of the impedance offered by the battery. This is difficult to obtain on a vehicle and varies not only with loading and environment but also over the battery life.

Keeping these factors in mind, several solutions have been proposed using Luenberger observers based on linearized state-space models of Li-ion batteries. These state-space models first must be obtained experimentally. One of the commonly used techniques is to obtain the voltage versus current frequency response of the cells in the pack. This frequency response V(s)/I(s) is essentially a measure of the impedance of the cell over a range of operating frequencies. The frequency response can be obtained using electrochemical impedance spectroscopy (EIS) tests.

Two key advantages of using observers over previously discussed techniques are that the techniques such as Kalman filtering can be used to increase the robustness of the observer to sensor noise from the voltage and current sensors on the battery (Plett, 2004). Plett was the first to describe this technique applied to equivalent circuit models of batteries. Smith, et al. performed further work using Kalman filtering (Smith, et al., 2010).

The Luenberger observer compares the measured value of the voltage to that output from the state-space model and attempts to minimize the error between the two. As a result, it is robust to errors in initial values of SOC. Even if the initial values of estimated SOC are different from the actual value, the estimated value converges to the actual value in a short time after the start of vehicle/battery operation (Piller, et al., 2001) (Pop, et al., 2005).

Luenberger observers can be implemented on the firmware of the battery management system in an economical manner. However, the cost of this implementation rises rapidly as hardware costs rise and as the state-space model complexity increases.

EIS Testing and Impedance Transfer Function

The frequency response of a cell can be used to understand its dynamic behavior. To this end, bode plots can be used to understand dynamic behavior of the battery pack.

A commonly used technique is performing EIS testing of the cell type being used. The EIS results are essentially a Nyquist plot of the impedance transfer function, i.e., the ratio of voltage and current over time as seen in the following equation.

$$Z(s) = \frac{V(s)}{I(s)} \tag{2}$$

Most automotive applications operate in the range from direct current up to the 10-Hertz (Hz) operating frequency regime. Thus, performing the EIS testing in this frequency domain is sufficient to capture all relevant dynamic responses of the cell. Furthermore, an equivalent circuit model can be fit to the impedance transfer function obtained from the EIS testing. It is important to note that low- to mid-frequency responses can be captured with sufficient accuracy using equivalent circuit models consisting of resistors and capacitors. Inductive elements are required in the equivalent circuit model to capture features in frequency regimes higher than 100 Hz, which is beyond that of most automotive applications.

An important observation regarding the Nyquist plot obtained from EIS testing from nanostructured LTO is that the charge-transfer resistance is much lower than that in which no nanoparticles are used. Work by Lu (2012) on EIS characterization of LTO nanostructure-based cells shows the nature of the Nyquist plot obtained for this chemistry and the layout of the equivalent circuit.

The impedance transfer function is one that has its numerator order lesser than or equal to that of the denominator. The equality arises when the transfer function captures direct feed-through terms, such as contact resistance between cell terminals and leads, etc. The coefficients of this transfer function depend on the parameters of the cell under study and will directly influence the entries of the state-space model.

Design of the Full State Observer

To construct the state-space model from the impedance transfer function, the transfer function’s poles and residues must be identified. One technique is to define the transfer function in the MATLAB environment and use the RESIDUE command to convert between partial fraction expansion and polynomial coefficients, with its inputs as the numerator and denominator of this transfer function. This returns a vector of the transfer function’s poles, residues, and the direct term, if applicable.

Knowledge of the poles, residues, and direct term is used to construct the A, B, C, and D matrices of the state-space model. The state-space model will express states that reflect some of the internal parameters of the cell, such as concentration of charged carriers at either electrode, as well as an integrator for measuring battery SOC. It is the evolution of the latter state during battery operation that gives the SOC estimate.

The Luenberger observer estimates the SOC by minimizing the error between the measured voltage and the voltage predicted by the observer, for the same current input as that applied to the actual battery. As long as the poles of this observer are in the left half of the complex plane, this error will converge to zero, and the estimate will converge to the actual value of the SOC.

General Example

The following is an overview of observer design from the knowledge of the impedance transfer function of a lithium-ion cell. The impedance transfer function can be obtained from the EIS testing of the cell, as described in the previous section. The technique described below is based on that described in *Battery Systems Engineering* by Rahn and Wang (2013).

The following is an example of an impedance transfer function obtained from the EIS testing of a Li-ion cell. The transfer function may be of the following form:

$$\frac{V(s)}{I(s)} = \frac{(b_1 s^3 + b_2 s^2 + \ b_3 s + b_4)}{(a_1 s^3 + a_2 s^2 + \ a_3 s)} \tag{3}$$

On applying the RESIDUE command to this transfer function, one obtains the poles, residues, and direct term associated with the transfer function. Therefore, the transfer function is factorized and represented as follows:

$$\frac{V(s)}{I(s)} = \frac{r_1}{(s - p_1)} \frac{r_2}{(s - p_{2)}} \frac{r_3}{(s - 0)} + K \tag{4}$$

The RESIDUE command returns a vector of residue term, r_i, a vector of poles p_i, and a direct term, K. It is important to understand the significance of each term obtained here. Consider the state-space representation obtained from this impedance transfer function. The state-space representation appears as follows:

$$\dot{x} = Ax + Bi \tag{5}$$

$$V = Cx + Di \tag{6}$$

where,

i = Current Drawn from the Battery and

V = Terminal Voltage across the Battery.

$$A = \begin{bmatrix} p_1 & 0 & 0 \\ 0 & p_2 & 0 \\ 0 & 0 & 0 \end{bmatrix}; B = \begin{bmatrix} 1 \\ 1 \\ 1/Capacity \end{bmatrix}; C = [r_1 \quad r_2 \quad r_3] \; and \; D = \; [K] \tag{7}$$

The poles p_1 and p_2 dictate the dynamics of the species concentrations in either electrode. Here the current drawn from the cell is in the input for dynamics at both electrodes. Hence the first two elements of the B matrix are 1. The third state of the state-space model is the SOC. Note that the third pole in this case is a zero, which represents a pure integrator or accumulation of charge. Further note that the third term in the B matrix is constructed to scale the current input by the battery's charge capacity.

The C matrix is a 1x3 matrix, implying a single measured output, i.e., terminal voltage. Additionally, the K term represents the battery's DC internal resistance that results in a drop in terminal voltage when current is drawn from the cell. The K term appears in the D matrix, which is a direct feed-through term among current, the input and voltage, and the output.

The objective of this state-space model is to design a Luenberger observer to estimate the third state, SOC. An observer is required because this state cannot be directly measured. This is clear from the structure of the C matrix.

The goal then is to place the poles of the observer in an optimal manner, keeping in mind the following considerations:

- The location of the observer poles will affect the speed at which the estimated value converges to the actual SOC value when there is an initial offset between the estimated and actual value.

- Analogously, the location of the poles will also dictate the response of the observer to sudden high C rates.

- Aggressive pole placement will enable the observer to converge to the actual SOC value very rapidly but will make the estimate very sensitive to noise on the measurements from the voltage transducers.

- Further, slight divergence is expected from the actual SOC value when the battery is operating at the limits of its OCV range. This is because the dynamics are increasingly non-linear in this region, and a linear state-space model that forms the basis of the observer does not capture these dynamics perfectly.

The following section shows results of simulation of the observer constructed in the manner described above. Note that the transfer function used to design the observer only serves as an example.

Simulation

Figure 11 shows simulation results from a demo of the technique described above. The red line indicates SOC estimated by the observer, and the blue line the actual SOC. Here, the actual SOC is computed by Coulomb counting. This simulation shows an accurate estimate of SOC and why this method should be considered as the benchmark for SOC estimation. Note its ability to correct itself in real time by converting with an initial offset.

It is important to notice that the initial SOC estimate has an offset. This offset reflects an error in the initial SOC estimate at the start of battery operation. At the start of battery operation or the initialization of a BMS, the only means of determining SOC is by referencing an OCV versus SOC map. Even if SOC were saved, self-discharge and environmental changes, among others, will have modified SOC. Again, this method has the ability to recover from these disturbances and handle events such as BMS power cycling or long off periods. It is clear from the graph that the estimated SOC “catches up” with the actual SOC in less than ten seconds.

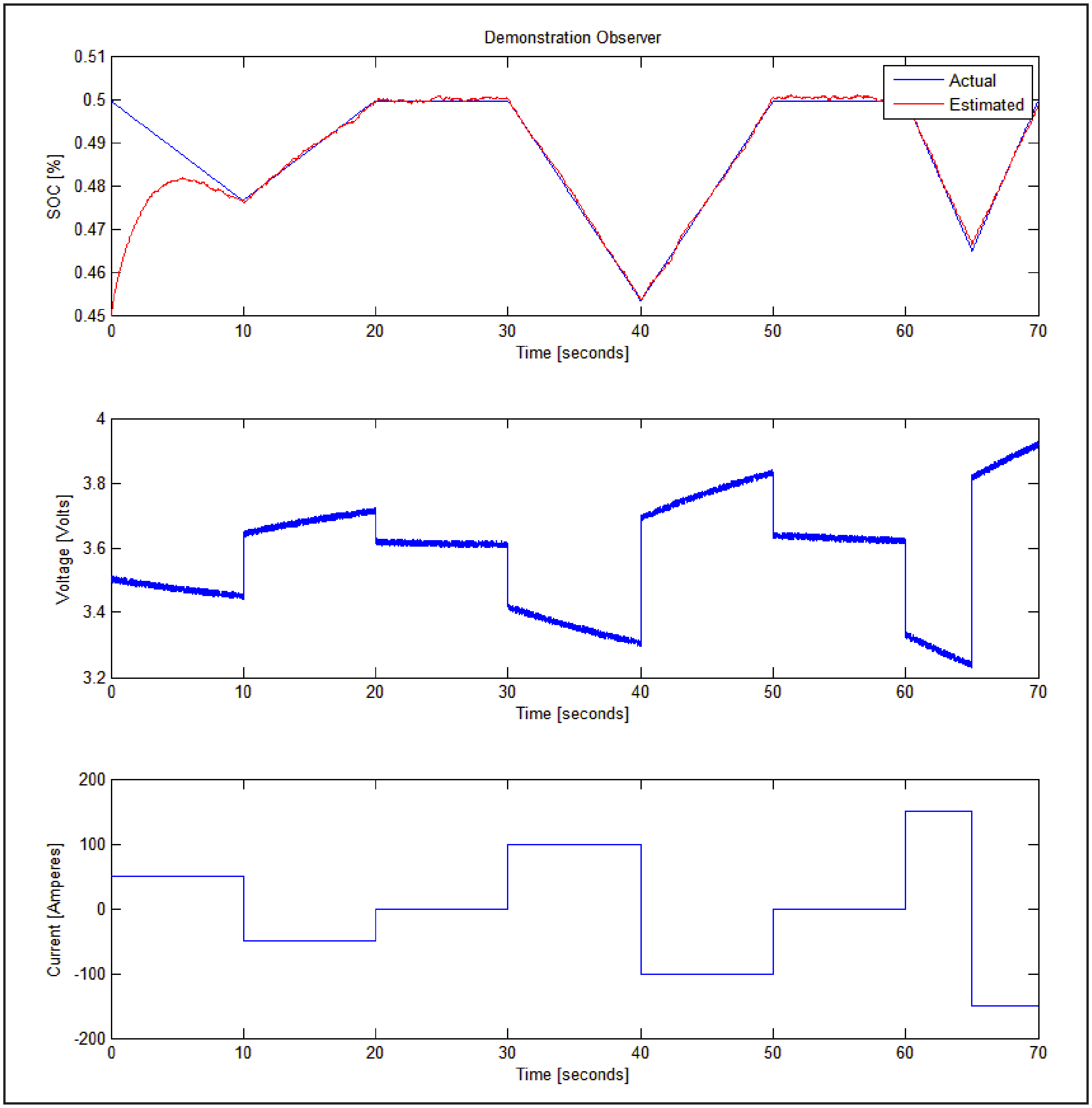

Figure 11. Demonstrated Observer

The time taken for this convergence to happen depends on the closed-loop pole locations of the transfer function. The choice of the pole locations involves a tradeoff between the time taken to converge to the actual SOC and sensitivity to sensor noise. A faster convergence to the actual SOC value may result in poorer noise attenuation and an introduction of errors due to noise voltage and current transducers.

The example presented above utilized data gathered by others using EIS testing on a similar chemistry. Because of limitations due to the large format nature of the LTO system studied in this work, high-frequency EIS testing was not reasonable. High-frequency testing is typically performed on low capacity/power cells. The battery system investigated in this research requires high power to fully exercise. High-frequency battery testing equipment is typically not also capable of high power. The researchers were limited to 10 Hz on their 125 and 250 kW power processing equipment. Instead of EIS testing, the research team took an alternative approach, using an equivalent circuit model to determine the transfer function of the LTO system under investigation. This is discussed in the following chapter.

IV. BATTERY MANAGEMENT SYSTEM SENSITIVITIY ANALYSIS

This section of the report discusses concerns about sensor accuracy relative to BMS functionality.

SENSOR ACCURACY

Battery management systems rely heavily on the sensors within a battery pack. Without this information, passenger safety and battery performance are sacrificed. These sensors typically include cell voltage, pack and/or string current, and a select distribution of temperature. A BMS will process these data and make a few decisions, adjusting how the pack is managed and if it will stay connected to the vehicle's loads. For example, if a cell's voltage is measured to be approaching an unsafe voltage or one that is highly sensitive to accelerated degradation, the BMS will likely warn other systems of this issue through its digital communication bus. This will notify other systems on the high-voltage bus that the electrical energy storage (EES) is approaching a limit. The nominal response should be that the other systems within the vehicle accommodate by reducing their load on the battery. If the issue isn't acknowledged by the other systems or if the load is not reduced in a sufficient time, then the BMS will attempt to protect the battery system by removing the system from external loads. It does this by opening a contactor inside the battery system. This is the only means a battery system has to protect itself. Ultimately, a typically BMS has control only over the contactors connecting it to the other high-voltage systems, such as drive motors, generators, or heating, ventilation, and air conditioning systems.

If inaccurate voltage, current, or temperature is measured, then a pack may be allowed to operate when it is unsafe or unhealthy for the cells. A BMS should and often does include substantial validation of measured data. For example, an electrochemical model of the particular cell can be relied on as a reference during SOC and SOH determination, but also as a validity check of measured data.

The research team investigated the effects of current sensor accuracy on SOC estimation in the eight-module pack. Because all ten cells of each module are in series, and each of the eight modules is also in series, current measured by each of the four sensors is identical to the current through each cell. Based on this understanding and the assumption that each cell has relatively the same SOC as all the others in the pack, cell SOC is then the same as pack-level SOC. In reality, each cell has slightly different capacity, ESR, and SOH, and it operates at a slightly different temperature. Because of this, each cell has a slightly different SOC. For the purposes of this study, the research team assumed all cells to be equal in ESR, SOH, capacity, and temperature.

A SOC value during operation is typically an estimation because the only way to know it with certainty is to perform a controlled discharge until the pack is empty. Integrating power out of a battery under discharge will determine the effective capacity the battery was holding prior to the discharge. Because this is not reasonable while in use, and any unnecessary discharge is avoided to maintain the highest possible system efficiency and fuel economy, BMS units estimate this value.

The only way to determine a pack SOC is by estimating based on real time and logged sensor data. Several different approaches to this algorithm have been used over the years and with different chemistries. In this section we will use the OCV and Coulomb counting method to compare current sensor accuracy effect on SOC. In later sections, the other methods will be discussed, and more accurate algorithms will be presented for SOC estimation.

Prior to each of the following tests, the battery was fully charged. For initial SOC in the analysis, the research team assumed that all 80 cells in the system were at equal SOC and fully charged. The team could have used the initial voltage measurement and results from capacity testing to determine initial SOC using OCV map versus SOC, but this study is interested primarily in the delta values associated with errors in current sensors. SOC determination is covered in more detail later in this report. Let's assume initial SOC equals 100 percent. The following equation was used to calculate the energy removed/added to the pack in terms of SOC in this 50 Ah pack.

$$SOC = SOC_{initial} + \frac{\int I \, dt}{C} \qquad (8)$$

Here I is measured current and C is the battery's nominal capacity. Note that equation (8) is used for each current measuring sensor, resulting in four different SOC estimations.

Figure 12 shows a 1C or 50 Amps constant current discharge and the SOC drift associated with this loading. Note that during the cycle, the battery system's current sensor and the laboratory-calibrated current sensor differ by 5.374 amperes. This offset error results in an SOC drift of 10.14 percent.

Similarly, Figure 13 shows a 2C or 100-ampere constant current discharge and the SOC drift associated with this loading. During this cycle, the battery system current sensor and the laboratory calibrated current sensor differ by a slightly smaller error of 4.217 Amps. This offset error then results in a lower SOC drift of 3.81 percent.

The BMS included with this battery is using its own current sensor, not monitoring any laboratory sensor data. Because of this configuration, the BMS resulting SOC value is expected to and clearly follows the "pack sensor – BMS" estimated SOC. Note that after the load is removed, the BMS then corrects itself based on pack voltage.

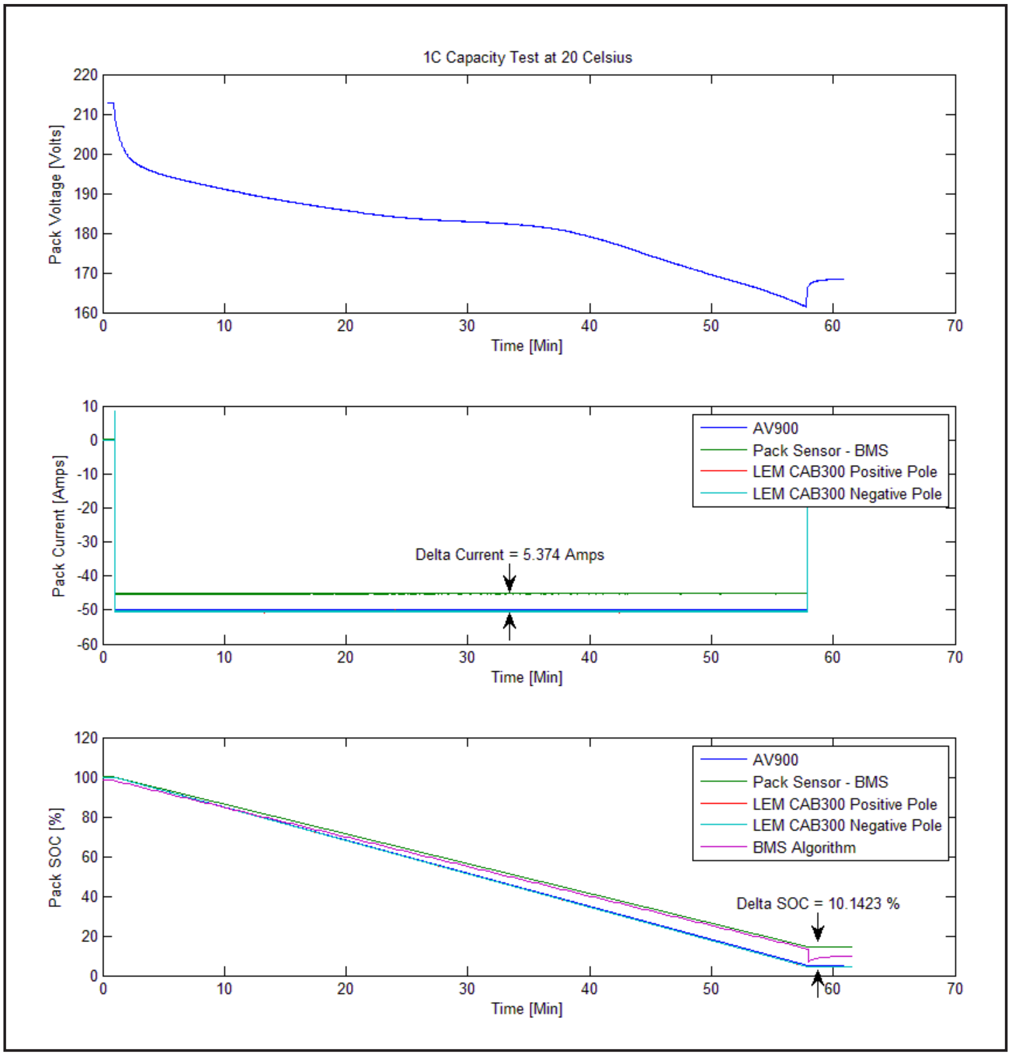

Figure 12. Current Sensor Accuracy during 1C Discharge

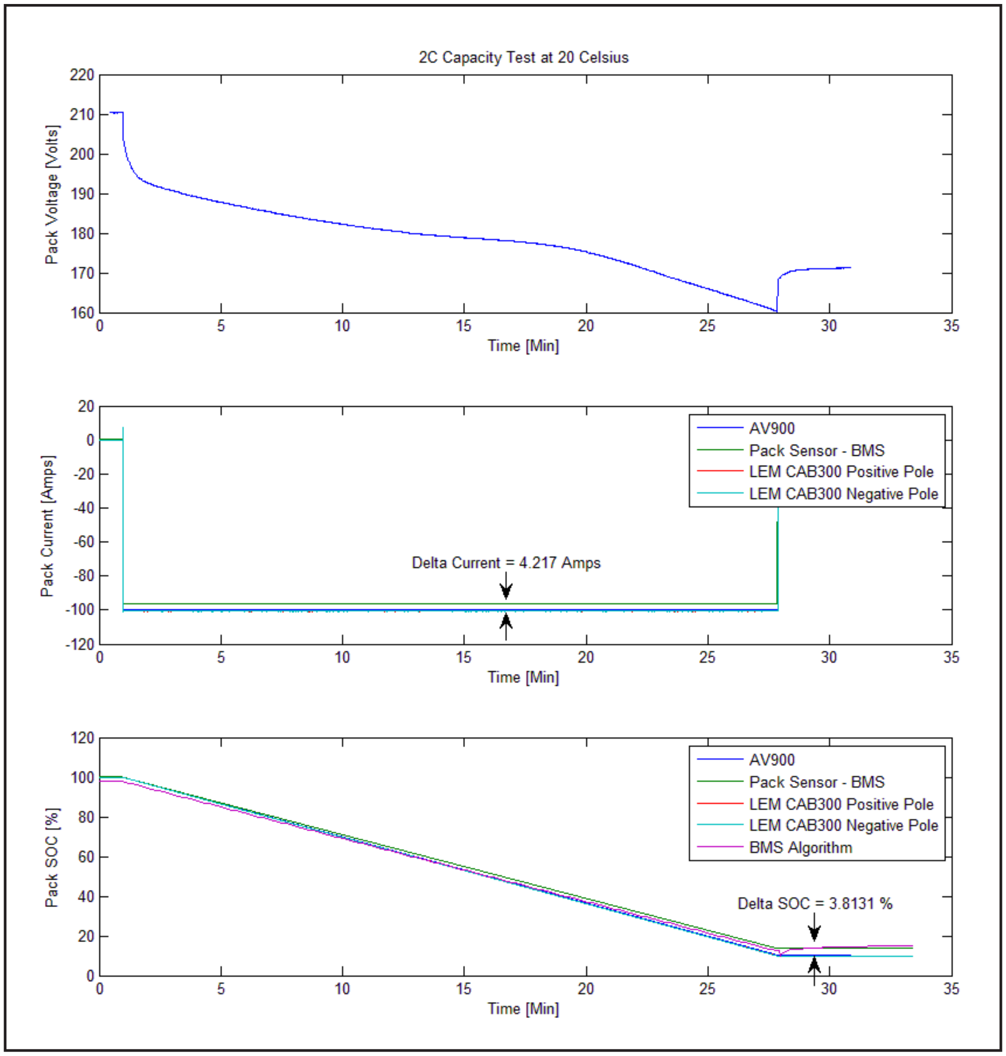

Figure 13. Current Sensor Accuracy during 2C Discharge

The constant current discharges show a reasonable drift in SOC due to the inaccurate current measurement. The same analysis was also performed on pulse power testing data with greater error measured during these higher C-rate loading profiles. Figure 14 shows the pack voltage, current, and integrated current over time. As with the constant current discharges, current is integrated to calculate the energy added/removed in terms of pack SOC.

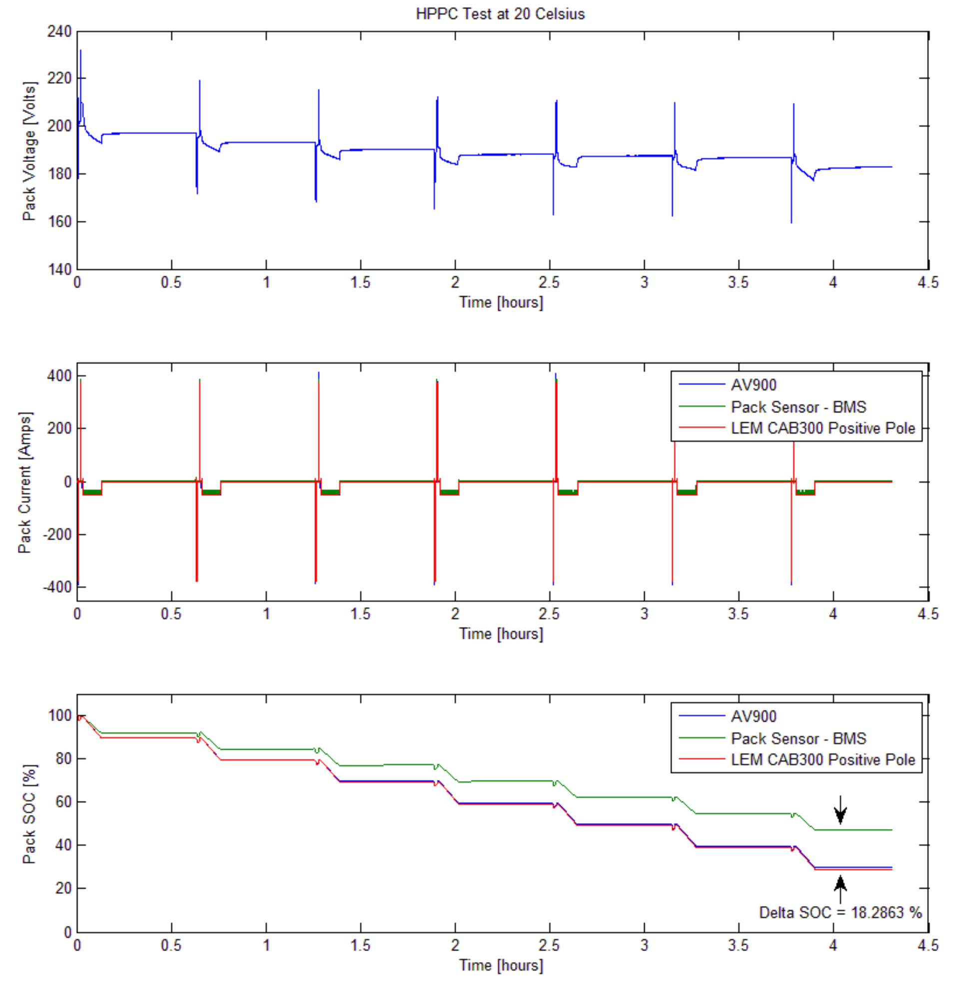

Figure 14. Current Sensor Accuracy during Pulse Power Testing

Using a different discharge profile and including some charge events results in additional error, as shown in these plots. Note that during the HPPC testing performed at 20°C, the estimated SOC was off by 18.29 percent by the end.

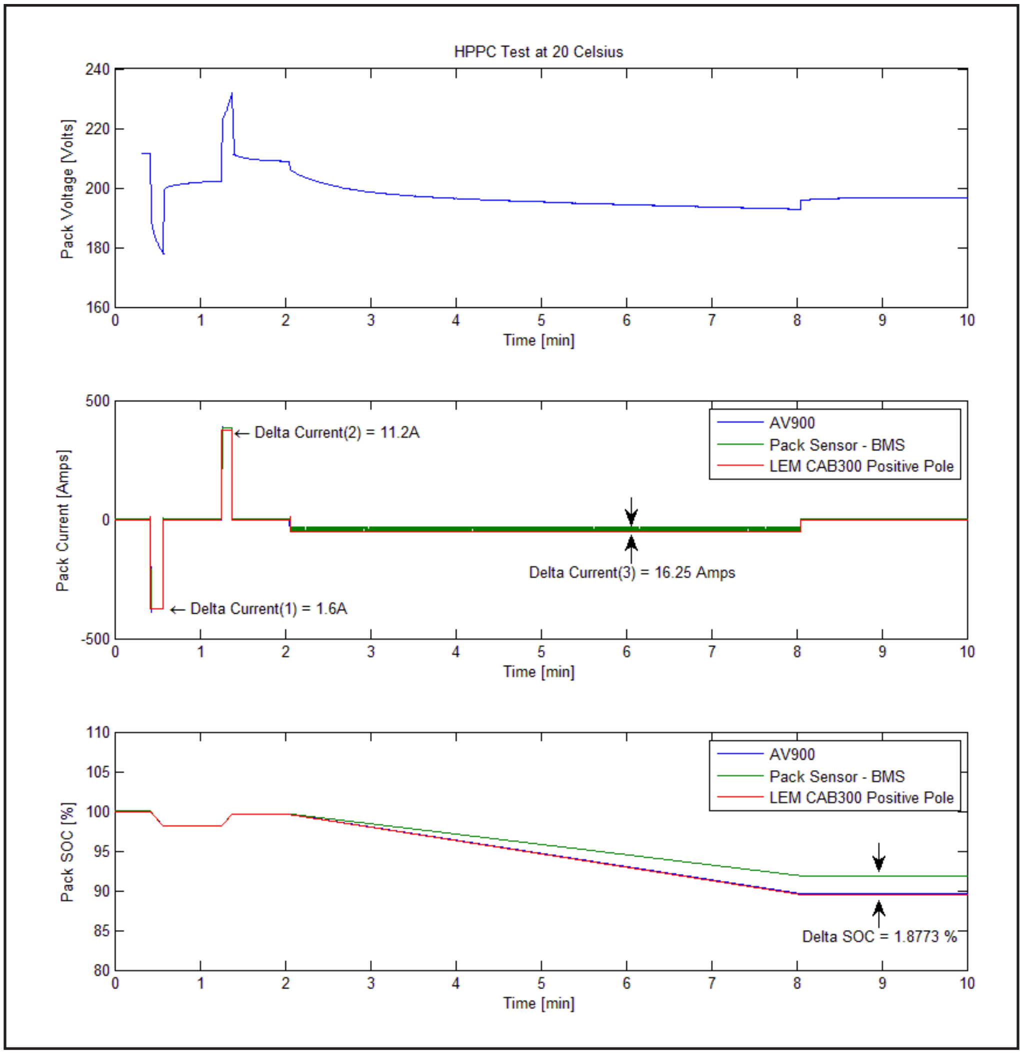

Figure 15. Current Sensor Accuracy during the First Ten Minutes of HPPC

Taking a closer look at HPPC data, Figure 15 shows the first set of pulses and a constant rate discharge. With current sensor errors of 1.6, 11.2, and 16.25 Amps, the resulting delta SOC value is about 1.9 percent after eight minutes.

Therefore, current sensor accuracy is critical in determining SOC while the battery is in use. If an SOC algorithm is relatively simple, as assumed in this sensitivity study, large error may build. One way to solve this problem is by continually correcting the SOC based on an OCV map. But with lithium chemistries, this cannot always be performed accurately, as seen above. Also, vehicle-level control decisions based on SOC may be affected by this adjustment.

The research team recommends more accurate sensors and adherence to manufacturer specifications when integrating these systems. Beyond the above recommendations, this report also covers more improved estimation processes and discusses them in detail to assist battery system engineers.

V. EQUIVALENT CIRCUIT MODEL

To avoid the complexities of a first-principles model, often an equivalent circuit model and measured data are used. Exercising the LTO 50 Ah modules of this research at both high power and high frequency is difficult for many laboratories. It is typically performed on small, low power cells, not high power modules. Because the research team's laboratory is equipped with the environmental and power processing equipment capable of high power but relatively low frequencies, a linear regression approach was taken to fit the selected Dual Polarization (DP) model to the measured data.

Battery terminal voltage response is often modeled using electrical components such as resistors, capacitors, inductors, and voltage sources. Several equivalent circuits are commonly used, and they range from simple series resistor and voltage source element systems to similar but slightly more complicated systems with additional and multiple parallel resistor/capacitor elements. An equivalent circuit model is much simpler when compared with first-principle models with partial differential equations (PDEs) and lengthy detailed efforts to capture the many complex activities within a cell (Hongwen He, 2011). This approach requires only a few parameters to accurately capture a cell's voltage response due to a known current load, and it is a realistic candidate for the low processing power of typical BMS microprocessors.

DUAL POLARIZATION MODEL

The Li-ion battery modeling literature consists of several examples showing the effectiveness of various equivalent circuit models in capturing dynamics of a Li-ion battery. Specifically, Hongwen He (2011) shows that the best capture of this voltage response for lithium chemistries is the Dual Polarization Model. The Dual Polarization model has the ability to simulate concentration polarization and activation polarization using two RC branches in series with a static series internal resistance. The Dual Polarization model (Hongwen He, 2011) has been applied to this work and is discussed in detail.

Activation and Concentration Polarizations

Two significant dynamics are those associated with Activation and Concentration Polarization. Both of these effects result in a voltage drop across the cell terminals, in addition to the cell's DC internal resistance. Furthermore, these dynamics occur at speeds that are a typically an order of magnitude apart from each other. Thus, these two effects must be captured to accurately predict a cell's voltage response under all load profiles.

Two Resistor–Capacitor (RC) branches in the equivalent circuit give the model sufficient fidelity to capture these dynamics because the two RC branches can have time constants that are orders of magnitude apart.

Activation Polarization

Activation polarization refers to the voltage drop due to various factors that retard electrochemical kinetics within the cell. The most dominant contributor to this polarization is the work required to overcome the impedance to charge-transfer that is presented by the electrode-electrolyte interface. Activation polarization is thus associated with electrochemical phenomena (Saha & Goebel, 2009). It is primarily related to charge-transfer dynamics under the action of an electric field or potential gradient. Most notably, these dynamics are typically fast.

Concentration Polarization

On the other hand, concentration polarization refers to voltage drop due to various factors that retard the diffusion-driven mass-transfer dynamics within the cell. In addition to ion-transfer due to a potential gradient, mass transfer takes place in the electrolyte due to concentration gradients. This process is typically slower than electrochemical processes (Saha & Goebel, 2009). When current to a Li-ion battery is cut off, the ion transfer within the electrolyte affects the voltage measured across the battery's terminals. This ion transfer is due to diffusion whose dynamics are typically an order of magnitude slower than those due to potential gradients. This is typically known as battery "relaxation."

EQUIVALENT CIRCUIT

Typically, cell characterization is based on EIS testing, in which a sinusoidal load is applied and cell responses measured. In the case of the research, team members were limited on their ability to cycle large-format battery packs at these high frequencies, some well above 1 kHz. Because of this, and to simplify the effort, the research team utilized standard pack-level testing and linear regression analysis to determine the parameters of the DP model similar to the method followed by Robyn Jackey (2013).

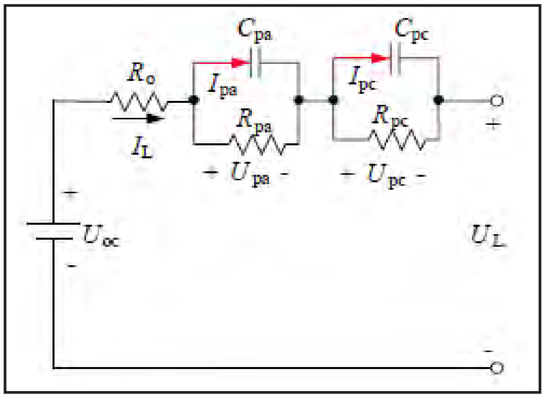

Figure 16. Dual Polarization Equivalent Circuit Battery Model

The dual polarization model shown in Figure 16 can be summarized by its three electrical components. First, there is a fixed voltage source, which is defined by a battery's open circuit voltage. Then there is a resistive load, R_o, representing the cells' Ohmic resistance, while R_{pa} and R_{pc} represent the cells' resistance due to activation polarization and concentration polarization, respectively. Finally, there are capacitance terms, C_{pa} and, C_{pc}, which characterize the transient response of the activation polarization and concentration polarization separately.

The dual polarization model can be expressed by the Equations - (Hongwen He, 2011), where U_{oc}, R_o, R_{pa}, C_{pa}, R_{pc}, and C_{pc} are all defined by maps that are functions of SOC and temperature, while Figure 17 represents the Simulink® model equivalent used for parameter estimation.

$$\dot{U}_{pa} = -\frac{U_{pa}}{R_{pa}C_{pa}} + \frac{I_L}{C_{pa}} \tag{9}$$

$$\dot{U}_{pc} = -\frac{U_{pc}}{R_{pc}C_{pc}} + \frac{I_L}{C_{pc}} \tag{10}$$

$$U_L = U_{oc} - U_{pa} - U_{pc} - I_L R_o \tag{11}$$

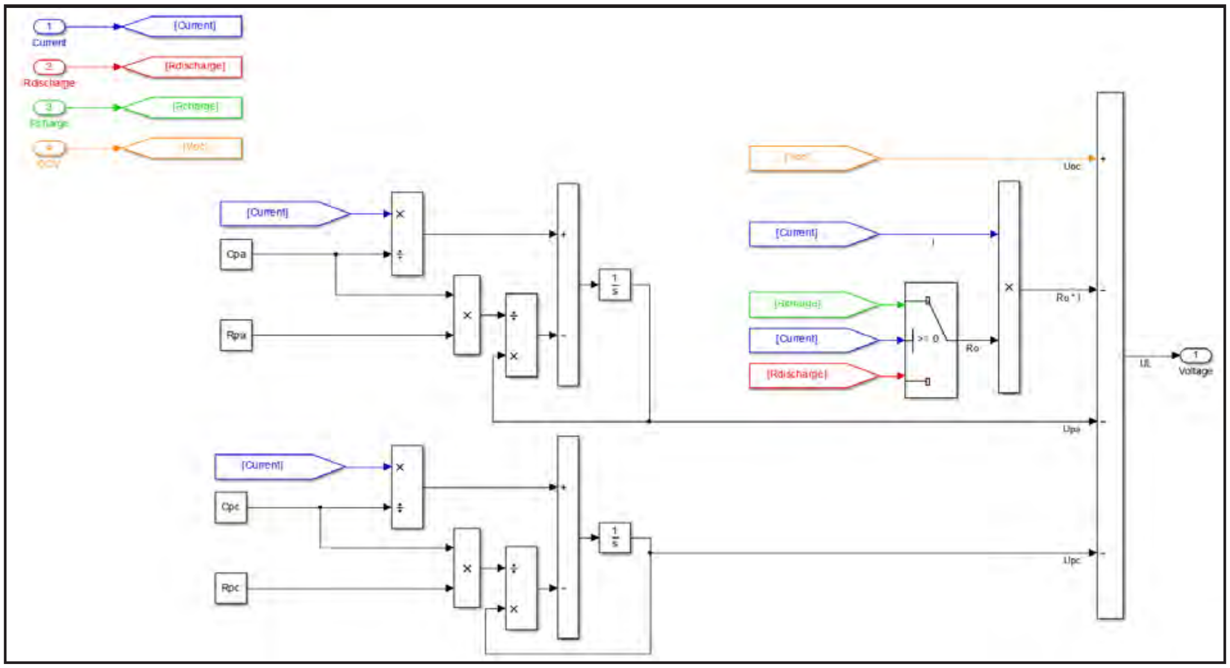

Figure 17. Dual Polarization Simulink® Model

Parameter Estimation

Measured data from HPPC testing were relied upon to run a series of parameter estimation tasks. Figure 18 and Figure 19 illustrate the HPPC load profile used during the test. They also illustrate how different parts of the terminal voltage response profile can be used to infer different parameters.

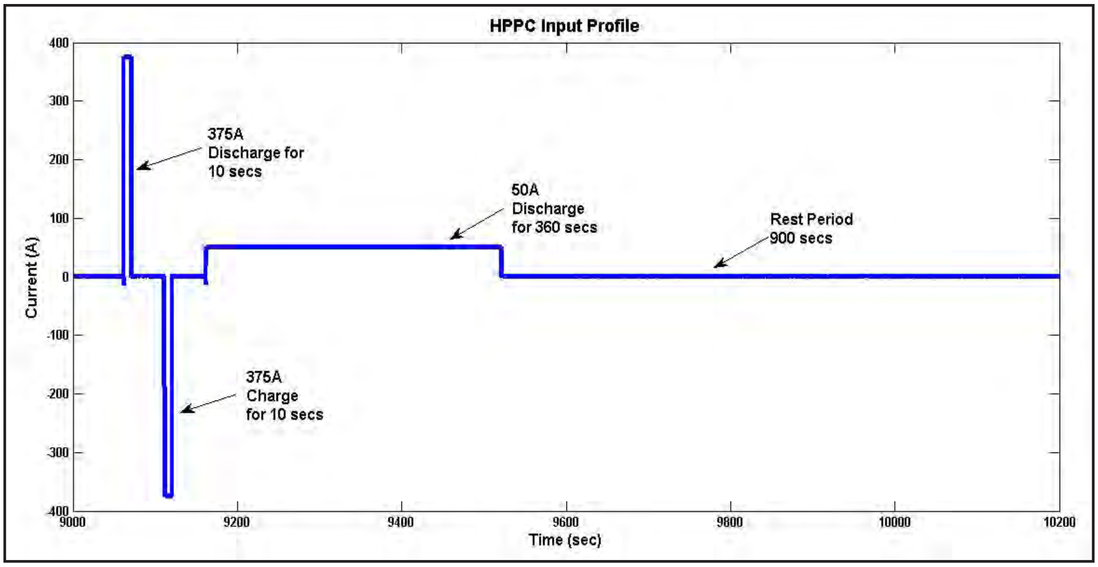

Figure 18. Current Profile of a Single HPPC Pule

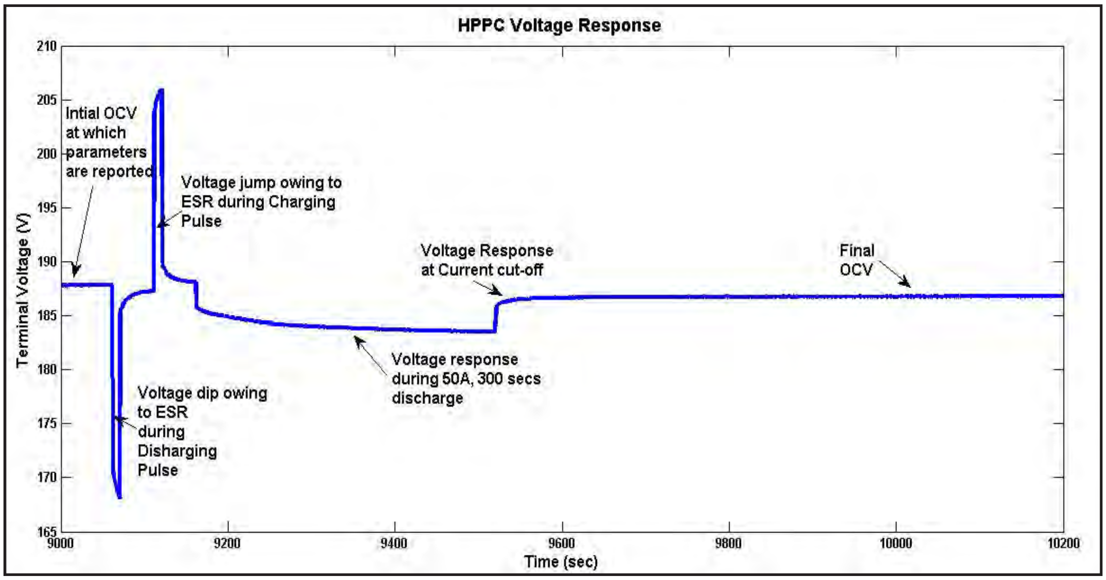

Figure 19. A Typical Terminal Voltage Response to an HPPC Load Profile

The HPPC load profiles shown in Figure 18 and Figure 19 were applied to the battery pack at four different temperature set points and across the entire SOC range for each temperature set point.

These parameter estimation tasks were executed using the model shown in Figure 16, with the help of the Simulink® Design Optimization Toolbox. Specifically, a Trust-Region-Reflective, Least-Squares optimization (The MathWorks, 2013) was performed for each measured data set and at each HPPC SOC pulse set. The resulting two time-constant (two RC branch) equivalent circuit model parameters capture very well the measured responses from test data. Figure 20 shows the resulting parameters for the pack at 40°C. A complete list of ESR values for charge and discharge is provided in Appendix B – ERS Tables.

SOC	Ra	Ca	Rc	Cc
13.17%	0.02460	109.80	0.05881	7203.0
23.24%	0.02423	207.89	0.04246	12199.0
33.31%	0.02054	235.40	0.03255	11025.0
43.38%	0.01424	296.02	0.02228	4205.2
53.45%	0.01398	309.54	0.01130	3158.6
63.52%	0.01128	354.31	0.01030	2645.8
73.59%	0.00991	436.17	0.01039	2446.6
83.66%	0.01016	437.13	0.01040	2456.5
93.73%	0.01006	468.56	0.00819	2146.6

Figure 20. Model Parameters at 40°C

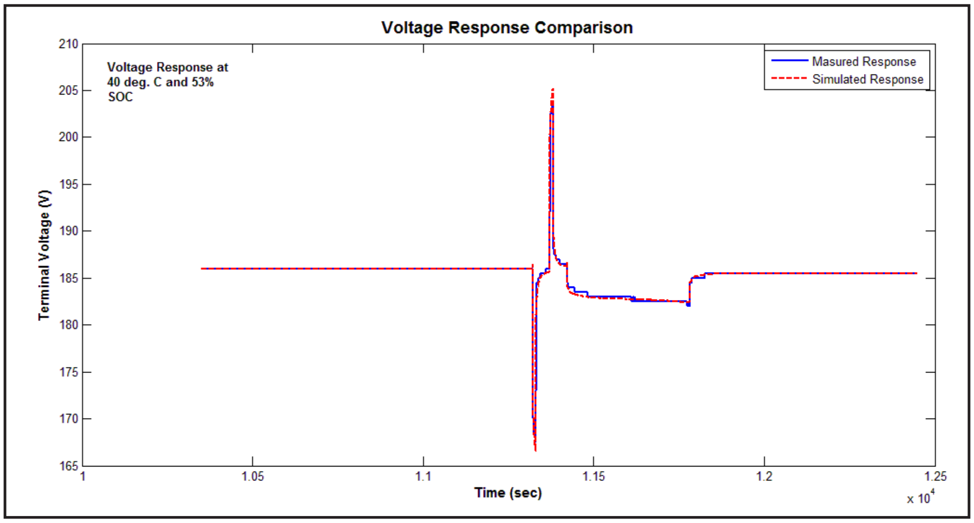

Figure 21. Voltage Response from 40˚C HPPC Testing at 53 Percent SOC

Figure 21 shows the voltage response of both the LTO battery under test and simulated voltage response of the ECM with estimated parameters.

Upon further analysis it is clearly seen that one time constant is an order of magnitude slower than the other. The slower time constant is the one associated with concentration polarization and the fast time constant is the one associated with activation polarization. The slower time constant provides additional fidelity to the model, enabling it to capture the voltage response during the relaxation process when current to the battery pack is cut off.

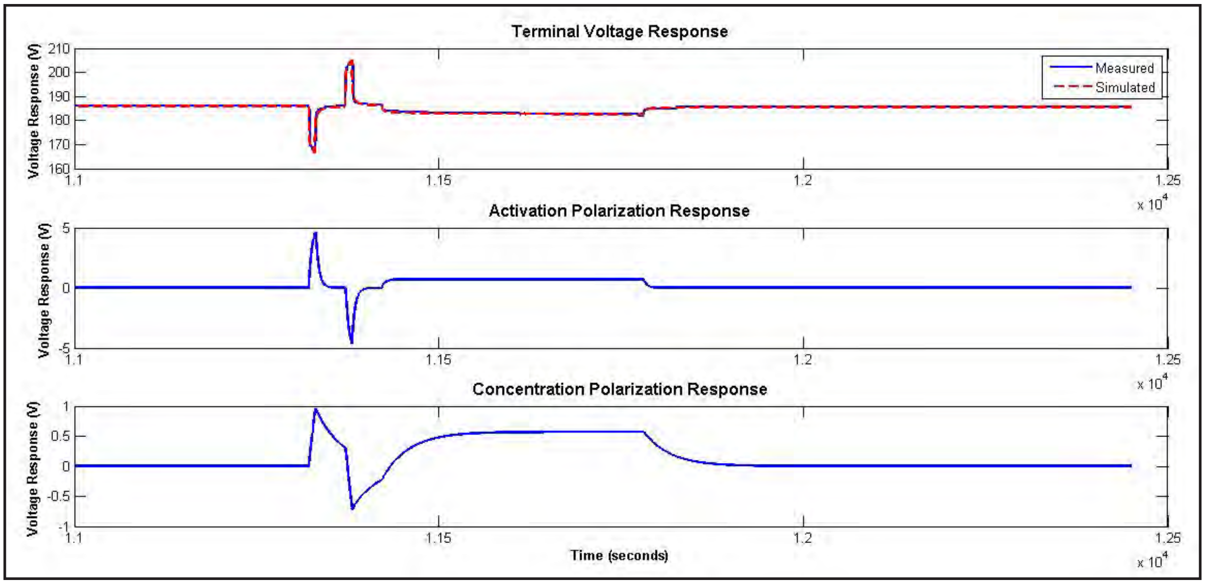

Figure 22. Activation and Concentration Response from 40˚C HPPC Testing

In Figure 22, notice the concentration polarization response between 1.15x10^4 and 1.2x10^4 seconds. When current is cut off, all voltage responses show a relaxation. The concentration polarization response is clearly much slower compared with that of the activation polarization. Also notice that the magnitude of the concentration polarization is smaller than that of activation polarization.

Consequently, when current is cut off, the terminal voltage does go through an initial rapid relaxation because of the relaxation in activation polarization response, with an approximate time constant of five seconds. However, the final part of the relaxation is much slower because it is driven by the concentration polarization. This analysis shows the closing of the final 0.5 V gap between the measured terminal voltage and the OCV during the relaxation phase has a time constant of approximately 400 seconds.

Figure 23 shows the comparison between the activation and polarization time constants at different SOCs at 40°C for the battery pack under study.

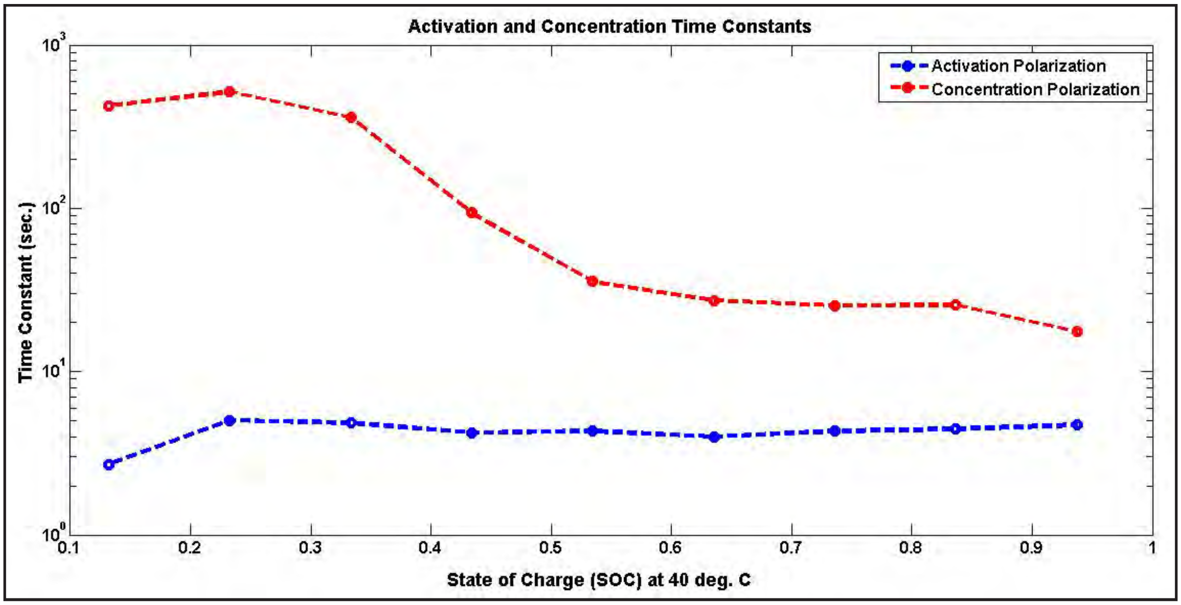

Figure 23. Comparison of Activaton/Polarization Time Constants w.r.t. SOC

Additional Results

Beyond 40˚C testing, both -20˚C and 20˚C parameters were estimated and compared to measured voltage responses. Figure 24 and Figure 25 show the voltage response results for 20˚C and -20˚C respectively. Also, a FUDS cycle was performed and the fitness of the resulting model compared in Figure 26.

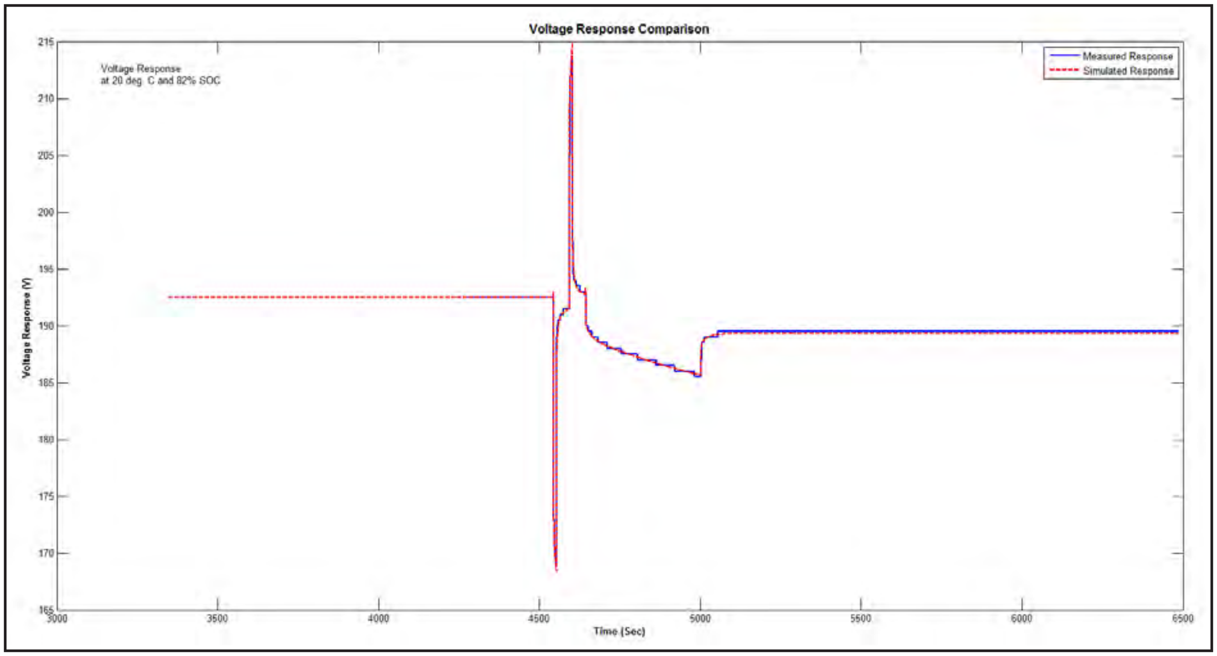

Figure 24. Voltage Response from 40˚C HPPC Testing at 82 Percent SOC

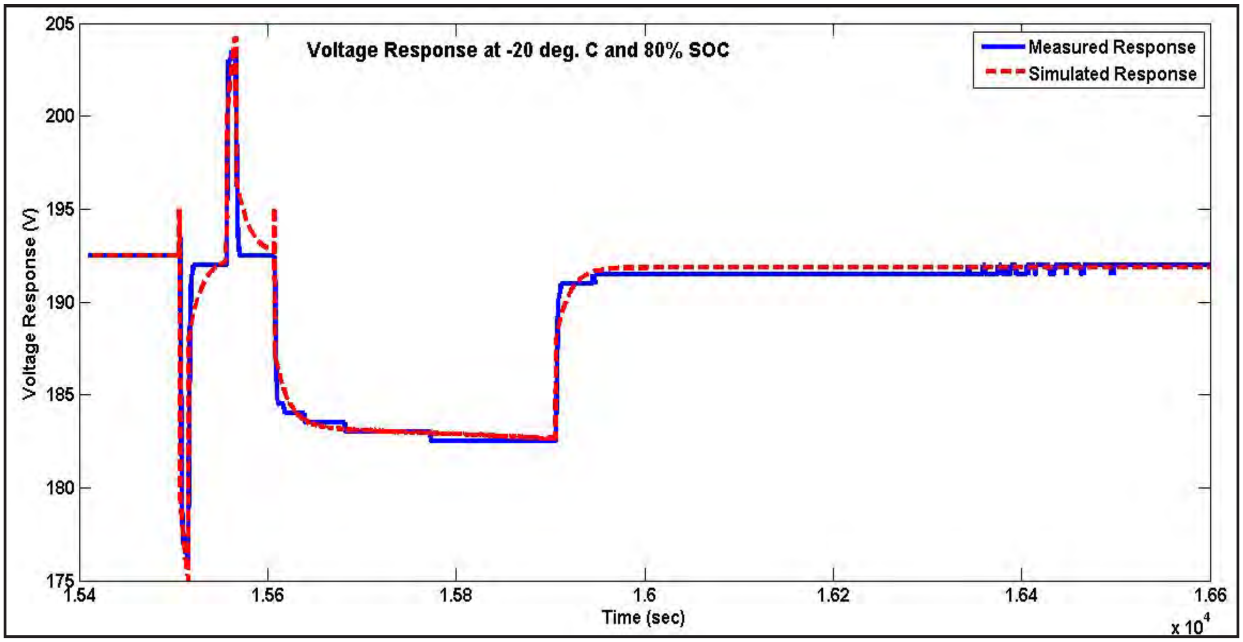

Figure 25. Voltage Response from 40˚C HPPC Testing

Figure 25 shows unexpected spikes in simulation voltage response. The source of this behavior is unfiltered current data input, and it represents an example of some difficulties faced by BMS algorithms. No filtering was performed on input data.

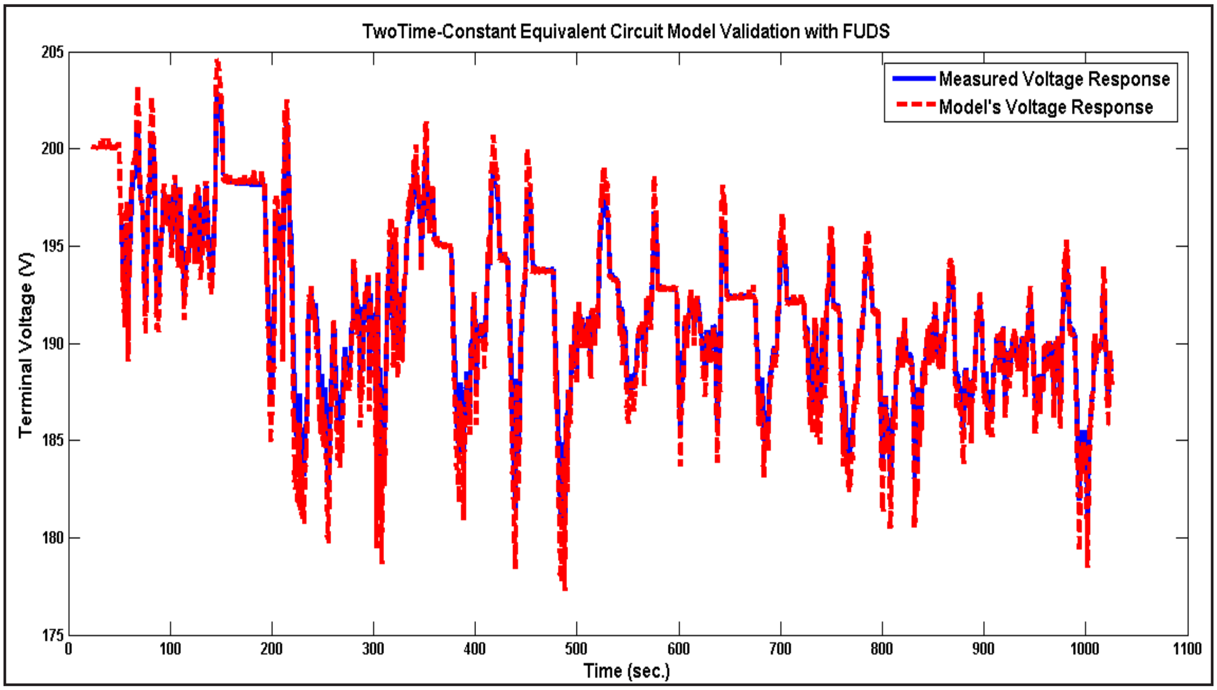

Figure 26. Voltage Response from FUDS Cycle

The results seen here, especially in Figure 26, show a good fit to measured data, indicating that the model, method, and estimated parameters for electrical modeling were successful.

VI. STATE-OF-CHARGE ESTIMATION USING EXTENDED KALMAN FILTER

In the previous section, the research demonstrated the development and utility of a dual-polarization model (two-time-constant equivalent circuit model) to capture all voltage response dynamics of the battery pack. The parameters used in the model are determined by empirically established functions of the battery's bulk temperature and SOC, thereby increasing model fidelity, as demonstrated previously.

However, this dependence of model parameters on the SOC and temperature introduces non-linearity into the model. Furthermore, because the end goal of estimator design is to implement it on a microprocessor, the model must be discretized. Discretization of the model further introduces a non-linearity into the governing equation.

Typically, discrete-time Kalman filters are used as optimal state estimators using noisy measurements of input and output. However, they can be used only for linear systems or for non-linear systems that have been linearized around a nominal operating point. Thus, the discrete-time Kalman filter cannot be constructed for SOC estimation on the equivalent circuit model the research team developed in this work. Therefore, an EKF is used. The non-linear model is linearized at every time-step, thus resulting in a linear time-variant system representation. Then a discrete-time Kalman filter can be implemented. This process forms the foundation of the EKF (Simon, 2006).

In the case at hand, the time-varying nature is introduced by the fact that model parameters, even after linearization, depend on the SOC and temperature. Therefore, all the model parameters must be refreshed at every time-step using the current value of SOC and temperature.

The following section describes the implementation of an EKF for SOC estimation using the team's equivalent circuit model for the battery pack under study. In this section, however, the team ignores dependence of the model parameters on temperature and instead presents an isothermal case in which model parameters depend only on SOC. Accounting for the temperature dependence of model parameters required the team to augment the heat-transfer dynamics model with this equivalent circuit model. This significantly increased the complexity of the estimation process. While this area is a subject of the team's ongoing effort, it is not covered in this report, which is restricted to model parameters being dependent purely on SOC.

EQUIVALENT CIRCUIT MODEL AND GOVERNING EQUATIONS

The equivalent circuit diagram and equations can be seen earlier in Figure 16 and Equations 9 through 11.

First, the non-linear equations governing the dynamics of this equivalent circuit model are set up. These equations are set up such that the system can be simulated in discrete time. Note that in the following equations, the superscript k represents the values at the k^{th} time step. The $k+1^{th}$ time step is treated as the current time step, and T denotes discrete time, although A^T indicates the transposition of matrix A.

MATHEMATICAL DESCRIPTION OF THE NON-LINEAR MODEL

State Vector

$$State\ Vector\ at\ time\ step\ k: x^k = (V_a^k \quad V_c^k \quad SOC^k)^T \tag{12}$$

Where,

V_a^k = Potential drop across Activation RC branch

V_c^k = Potential drop across Concentration RC branch

SOC^k = State of Charge of the Battery.

Model Input

i^k = Measured value of battery current at the k^{th} time step.

Model Output

$V_{terminal}^k$ = Terminal Voltage at the k^{th} time step.

Model Parameters

$T_a(SOC^k)$ = Activation Polarization Time-Constant as a function of SOC

$R_a(SOC^k)$ = Activation Resistance as a function of SOC

$T_c(SOC^k)$ = Concentration Polarization Time-Constant as function of SOC

$R_c(SOC^k)$ = Concentration Resistance as a function of SOC

$R_o(SOC^k)$ = DC Resistance as function of SOC

$V_{oc}(SOC^k)$ = Open Circuit Voltage as a function of SOC.

ΔT_s = Discrete time-step size

W^k = Zero-mean Gaussian white process noise k^{th} time-step

V^k = Zero-mean Gaussian white measurement noise at k^{th} time-step

Non-Linear Governing Equations

State Transition Functions

$$x^{k+1} = f_k\left(x^k, i^k, w^k\right) \tag{13}$$

$$V_a^{k+1} = \exp\left(\frac{-\Delta T_s}{\tau_a(SOC^k)}\right) V_a^k + \ R_a\left(SOC^k\right)\left(1 - exp\left(\frac{-\Delta T_s}{\tau_a(SOC^k)}\right)\right) i \tag{14}$$

$$V_c^{k+1} = \exp\left(\frac{-\Delta T_s}{\tau_c(SOC^k)}\right) V_c^k + \ R_c\left(SOC^k\right)\left(1 - exp\left(\frac{-\Delta T_s}{\tau_c(SOC^k)}\right)\right) i \tag{15}$$

$$SOC^{k+1} = \ SOC^k + \frac{\eta \Delta T_s i}{C_n} \tag{16}$$

Measurement Function

$$y^k = g_k\left(x^k, i^k, v^k\right) \tag{17}$$

$$V_{terminal}^k = -V_c^k - V_a^k \ -i^k R_o\left(SOC^k\right) + V_{OC}\left(SOC^k\right) \tag{18}$$

IMPLEMENTATION OF THE EXTENDED KALMAN FILTER

Initializing the Kalman Filter

The Kalman filter must be initialized with the best possible guess of the state estimate x^0 and the error covariance matrix p^0. The error covariance matrix is defined as follows:

$$P^0 = E\left[\left(\boldsymbol{x} - \boldsymbol{x^0}\right)\left(\boldsymbol{x} - \boldsymbol{x^0}\right)^T\right] \tag{19}$$

Computing the F Matrix

The matrix F is used by the EKF at every time step. It is computed as per the following:

$$F^k = \begin{bmatrix} \frac{\partial V_a^{k+1}}{\partial V_a}\Big|_{x^k} & \frac{\partial V_a^{k+1}}{\partial V_c}\Big|_{x^k} & \frac{\partial V_a^{k+1}}{\partial SOC}\Big|_{x^k} \\ \frac{\partial V_c^{k+1}}{\partial V_a}\Big|_{x^k} & \frac{\partial V_c^{k+1}}{\partial V_c}\Big|_{x^k} & \frac{\partial V_c^{k+1}}{\partial SOC}\Big|_{x^k} \\ \frac{\partial SOC^{k+1}}{\partial V_a}\Big|_{x^k} & \frac{\partial SOC^{k+1}}{\partial V_c}\Big|_{x^k} & \frac{\partial SOC^{k+1}}{\partial SOC}\Big|_{x^k} \end{bmatrix} \tag{20}$$

It is important to note that this matrix varies with time. Its entries depend on the state estimate at every time-step. Owing to the nature of the non-linear system, the entries of these matrices will in fact depend on the estimate of SOC at the k^{th} time-step.

Since the parameters R_a, T_a, T_c, and R_c depend on SOC, the estimate of the SOC at the k^{th} time-step is used to compute the value of these parameters at the k^{th} time-step. These values are then used in computing the above matrix. This introduces the time- variable. nature of this matrix.

Time Update Stage

In this stage, the *a priori* estimate of the state vector (x_-^{k+1}) and the error covariance matrix (P_-^{k+1}) is calculated based on the system model, covariance of process-noise (Q^k) (representative of modeling uncertainty), and the estimated values of x^k *and* P^k from the previous time-step. The equations used are as follows:

$$P_-^{k+1} = F^k P^k (F^k)^T + Q^k \tag{21}$$

$$x_-^{k+1} = f_k\left(x^k, u^k, w^k\right) \tag{22}$$

The next stage of the algorithm is the Measurement-Update Stage. In this stage, a second estimate of the states and error covariance matrix is calculated. This second estimate involves a correction based on system output at the current time-step. The new estimates are more accurate because they capture the information obtained at this time-step.

Computing the H^{k+1} Matrix

To execute this second stage, the following output matrix must be evaluated. This matrix is evaluated using the state estimates, not from the previous time-step, but those from the "time-update" stage of the algorithm for the current time-step.

$$H^{k+1} = \left[\frac{\partial V_{terminal}^k}{\partial V_a} \Big|_{x_-^{k+1}} \quad \frac{\partial V_{terminal}^k}{\partial V_c} \Big|_{x_-^{k+1}} \quad \frac{\partial V_{terminal}^k}{\partial SOC} \Big|_{x_-^{k+1}} \right] \tag{23}$$

Computing Kalman Gain at the K^{th} Time-step

Using H^{k+1} and error covariance matrix (P_-^{k+1}) computed in the "time-update" stage matrices, the Kalman gain K^{k+1} matrix for this time-step is evaluated per the following equation:

$$K^{k+1} = P_-^{k+1} (H^{k+1})^T \left(H^{k+1} P_-^{k+1} (H^{k+1})^T + R^{k+1}\right)^{-1} \tag{24}$$

Here, the matrix R^{k+1} is the discrete-time covariance matrix of the measurement noise. This matrix is constructed by obtaining covariance of noise on all measurement signals.

Computing Measurement-Updated State Estimate

In this stage, the measurement function is used along with the *a priori* estimate of the state, and zero measurement noise, to compute the terminal voltage predicted by the EKF. This is compared against the terminal voltage measurement made at the current time-step to obtain the innovation term.

This innovation term is multiplied with the Kalman gain (K^{k+1}) to obtain the correction factor added to the time-update stage state estimate. This correction factor is derived from the voltage measurement at this time-step, thus making the measurement-update stage estimate more accurate than that from the time-update stage.

$$x^{k+1} = x_-^{k+1} + K^{k+1}\big(V_{terminal}^{k+1} - h(x_-^{k+1}, i^{k+1}, 0\big) \tag{25}$$

Computing Measurement-Updated Error Covariance

The error covariance matrix (P^{k+1}) is corrected using the following equation. Thus, an updated and more accurate value of the error covariance is obtained, which is used for the estimation process in the next time-step:

$$P^{k+1} = \big(I - K^{k+1}H^{k+1}\big)P_-^{k+1} \tag{26}$$

Implementation of the Extended Kalman Filter in Simulink®

The extended Kalman filter is essentially a "virtual sensor" to sense state of charge. It is based on the dual-polarization model developed earlier and on the equations derived above. The end-goal of developing the extended Kalman filter is to deploy it as firmware on the bus' BMS. From this perspective the implementation is carried out in Simulink® in a manner that C code can be generated from it.

The filter is first designed, implemented, and validated using the dual-polarization battery model developed by the authors. The Voltage Response from this model is taken, and simulated white noise having the same covariance as that of the voltage transducer is added to it. This serves as the voltage sensed by the EKF. The high-level implementation is seen Figure 27.

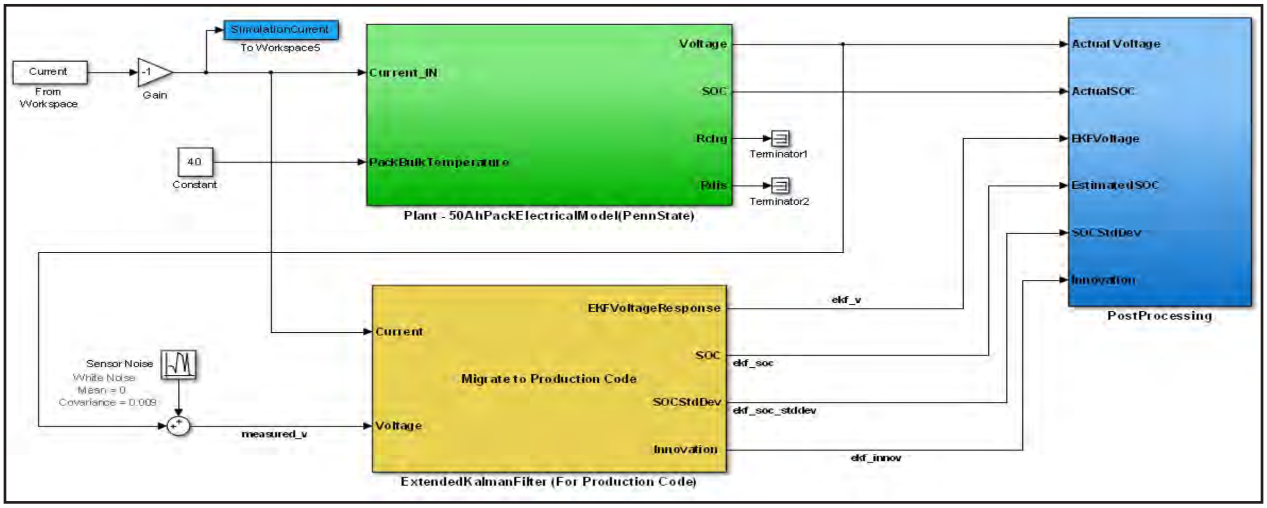

Figure 27. Overview of the Simulink® Implementation of the SOC Estimator

Figure 28 shows the detailed implementation of the extended Kalman filter. It shows two MATLAB function blocks – one that implements the time-update Stage and another that implements the measurement update stage of the extended Kalman filter.

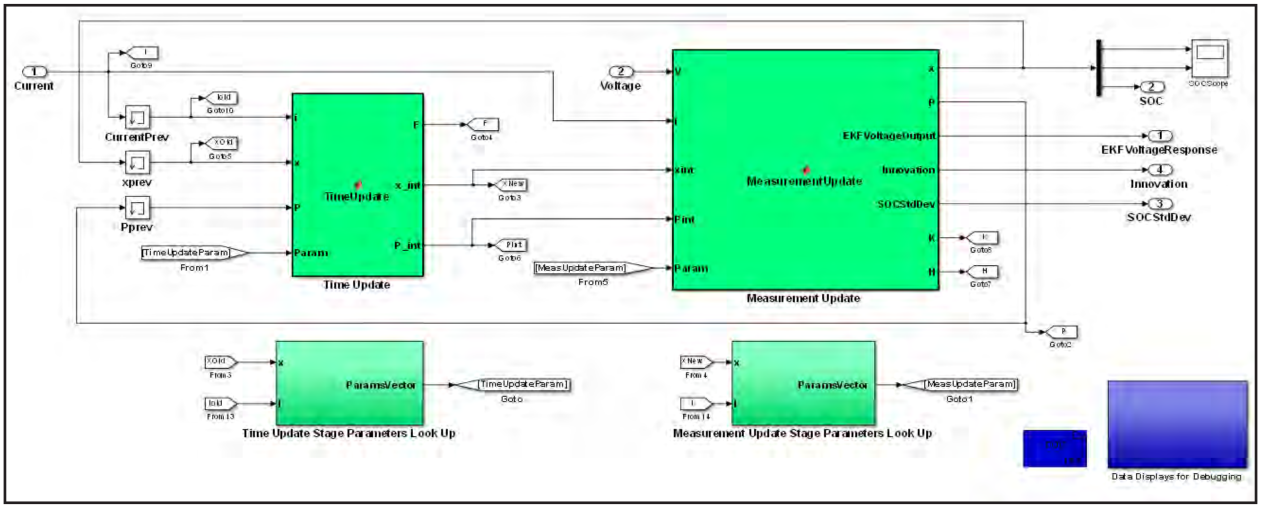

Figure 28. Time-Update and Measurement-Update Stages

At every time step, all parameters of the discretized state and measurement equations of the battery model are evaluated as a function of SOC. This is done through a series of lookup tables that contain maps of variation of different model parameter values, with respect to SOC. Figure 29 is the implementation of these lookup tables.

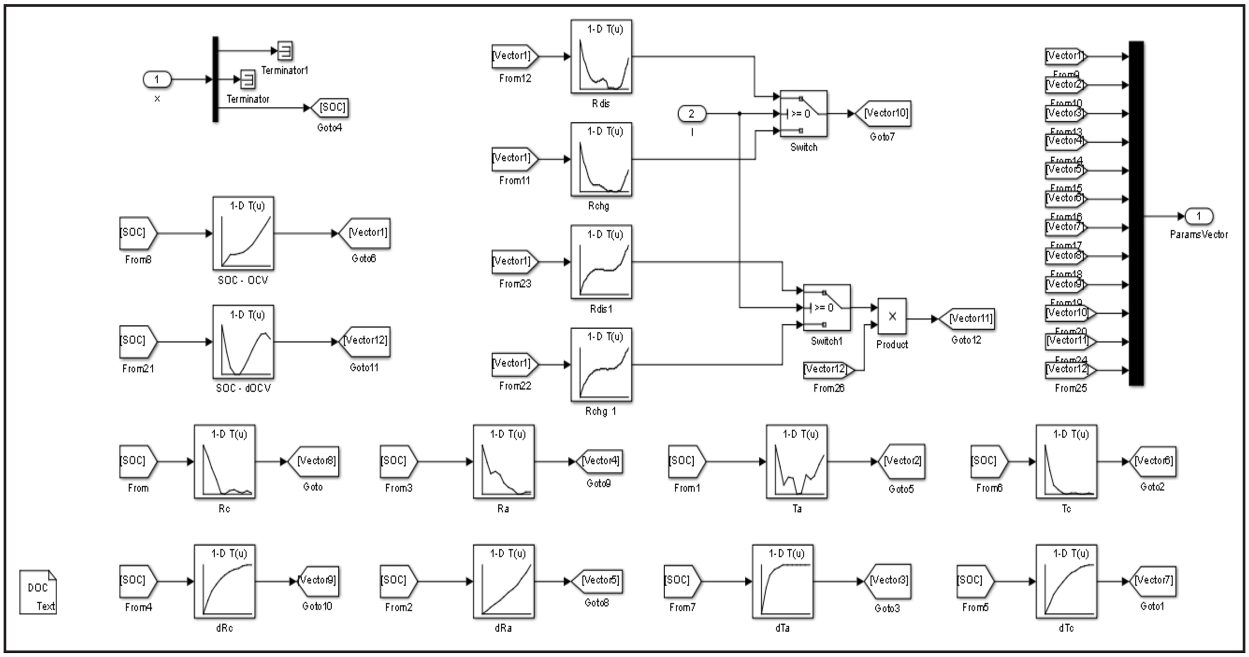

Figure 29. Implementation of Parameter Maps Using Simulink® Tables

Performance of the Extended Kalman Filter

The EKF is tested with a variety of load profiles and performance metrics, including innovation, state estimation error, and state estimate covariance. This section shows the performance of the filter for a single 3C discharge pulse and for a Federal Urban Driving Schedule with an initial state estimate error of ~30 percent.

Verification with a 3C Discharge Profile

Figure 30 shows the load profile of a single 200-second 3C discharge pulse. Note that before applying this load profile, the voltage estimation is initialized with an estimate that has a 30 percent error. Within just a few seconds, the estimator is able to overcome this 30 percent error and produce a rather stable response with negligible error throughout the remainder of the profile. The researchers consider this a successful validation of the EKF voltage estimator.

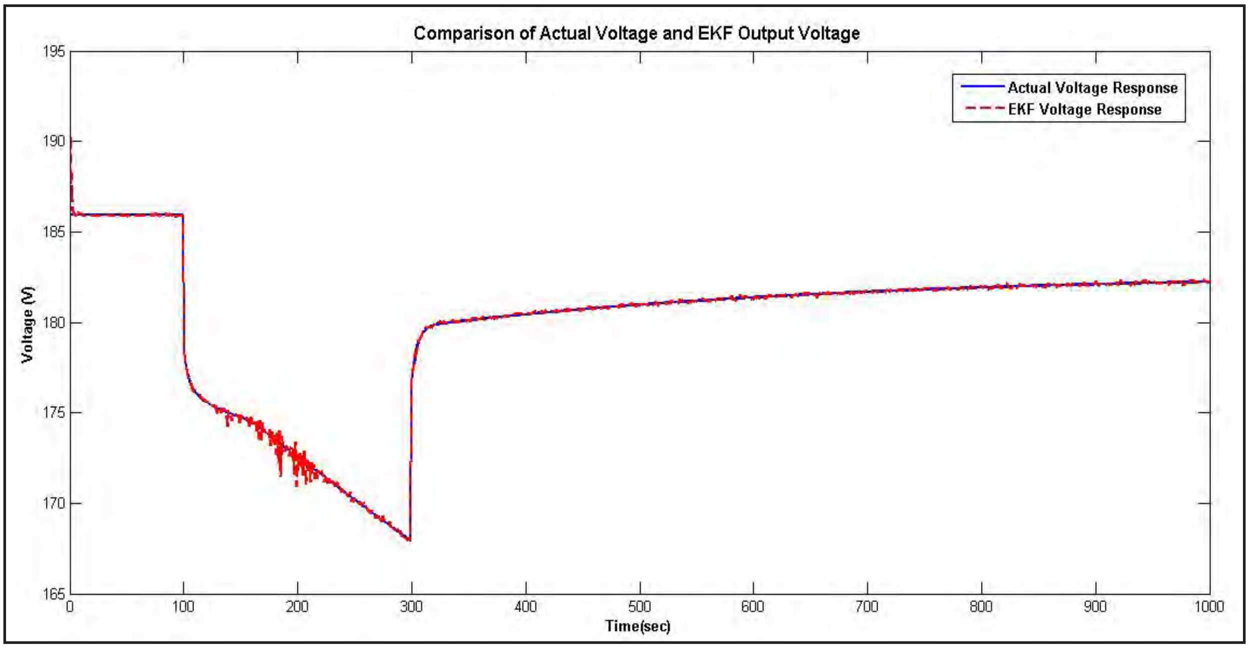

Figure 30. Comparison of Actual Voltage and EKF Voltage Output

Figure 31 shows a comparison between SOC obtained by current counting from the battery model (which is treated as the “Actual SOC”) and that estimated by the EKF. The initial estimate of SOC has an error of ~30 percent. The error reduces to under ~10 percent very rapidly, in the first ~8-10 seconds of operation. The estimation error reduces with time and the SOC estimate closely matches, with negligible error, the actual SOC from ~200 seconds onward.

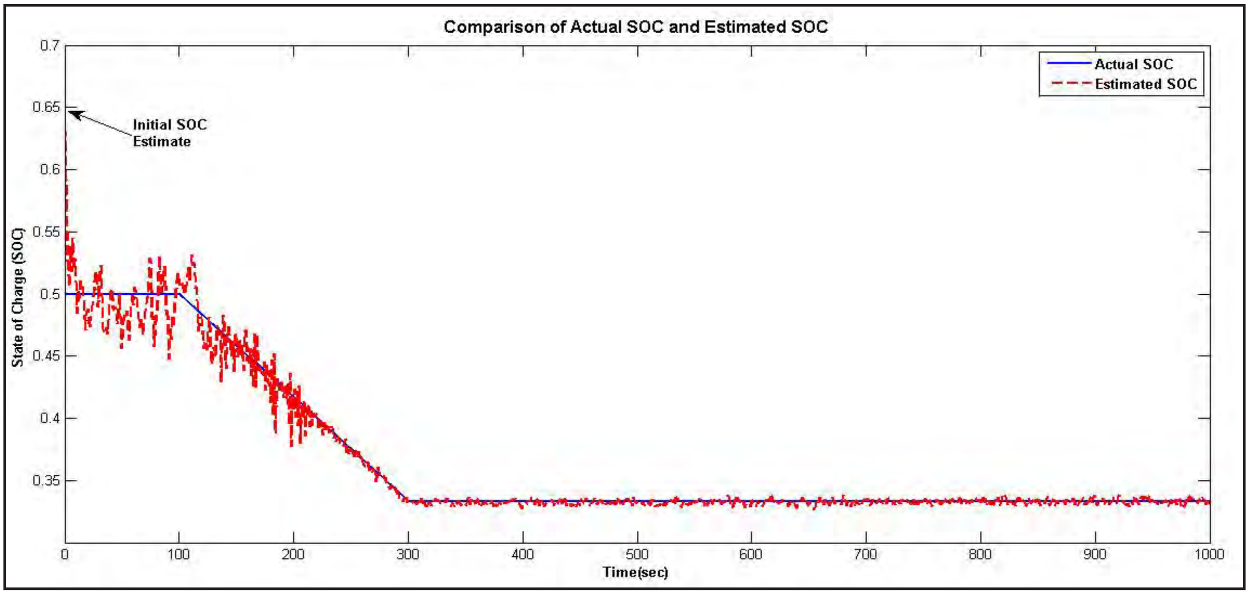

Figure 31. Comparison of Actual SOC and Estimated SOC

Figure 32 shows the evolution of the SOC estimation error with time. It is clearly seen that the SOC estimation error settles down to under ~2 percent after 200 seconds of operation. Further, the graph shows a moving average of the SOC estimation error. SOC estimate value filtered through a low-pass filter/moving average filter is the best SOC estimate that can be used for other downstream control decisions. Thus, it is important to evaluate the moving average of the estimation error. The moving average of the estimation error starts at ~-25 percent but quickly settles at 0 percent, as seen in Figure 32.

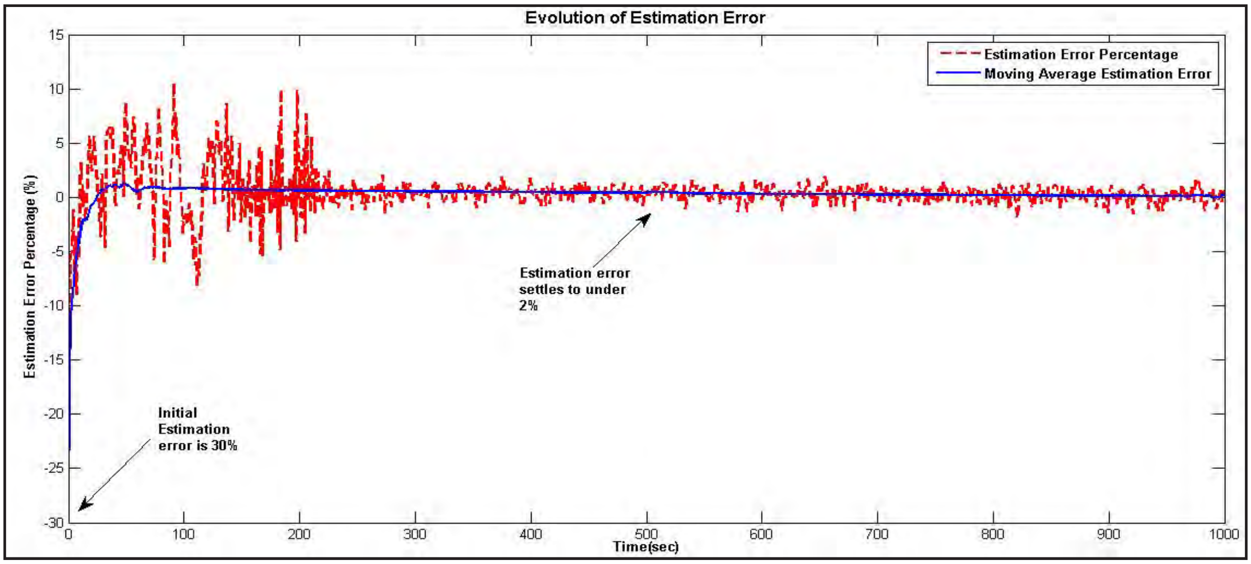

Figure 32. Evolution of Estimation Error Percentage and Its Moving Average

Verification with the FUDS Cycle

Using the Federal Urban Driving Schedule was another step in the validation process. This is a real-world driving cycle, far removed from the “ideal” single current pulse input profile demonstrated above. This was an important and critical step in testing the performance of the EKF and its ability to rapidly respond in the event of an aggressive driving cycle. In addition, the EKF was initialized with an erroneous state estimate. Figure 33 represents the equivalent FUDS load profile of current based on the battery system under test.

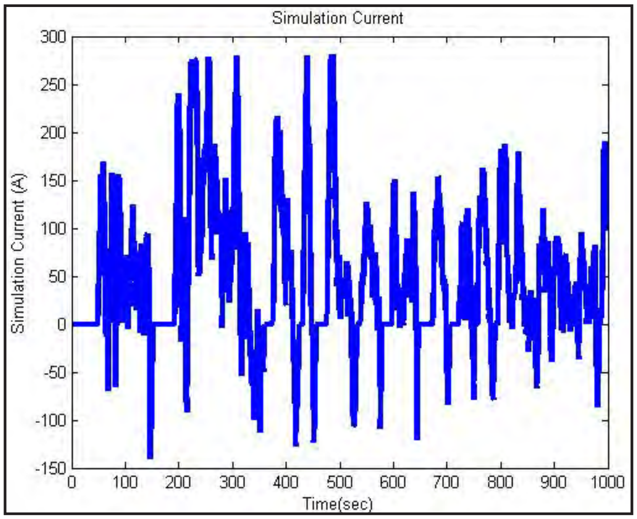

Figure 33. Load Profile for the FUDS Cycle

Figure 34 shows a comparison of the voltage from the battery model and EKF. As before, the EKF’s voltage response starts with an initial error due to an erroneous state estimate initialization. However, it quickly converges to the actual voltage response and follows it closely throughout the 15-minute cycle.

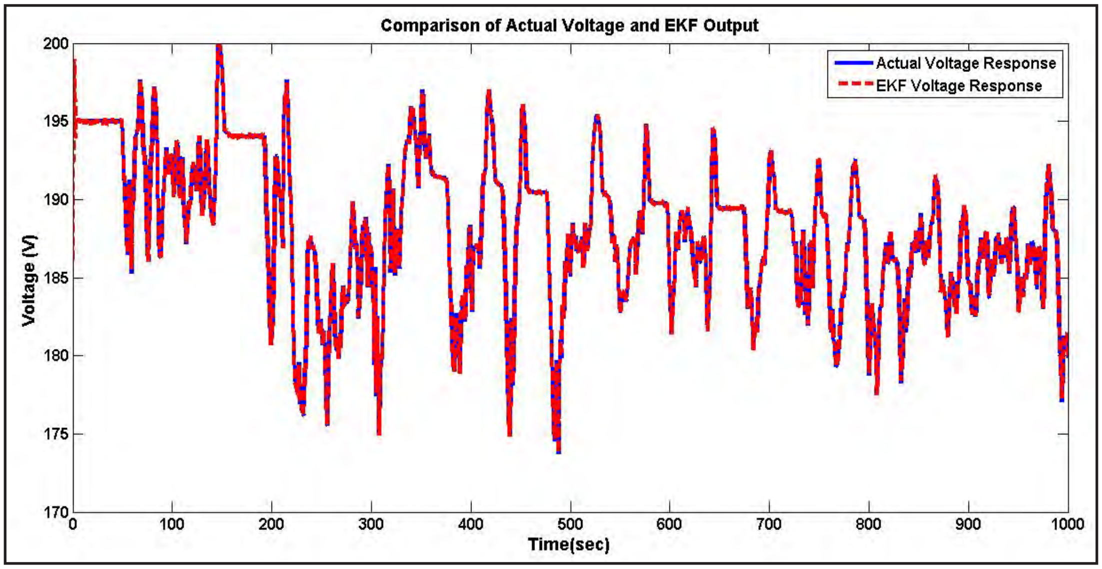

Figure 34. Comparison of Measured Voltage and EKF Voltage Response

Figure 35 shows the evolution of the innovation term, i.e., the error between the actual voltage output from the battery model and the voltage prediction by the EKF. It can be seen that there is an initial error due to the fact that initial state estimate has a ~30 percent error. However, predicted voltage quickly converges to the measured value and the error remains under 2 percent for the remainder of the simulation. The error between the voltage measured from the battery model and that from the EKF is known as "innovation" in Kalman filtering jargon.

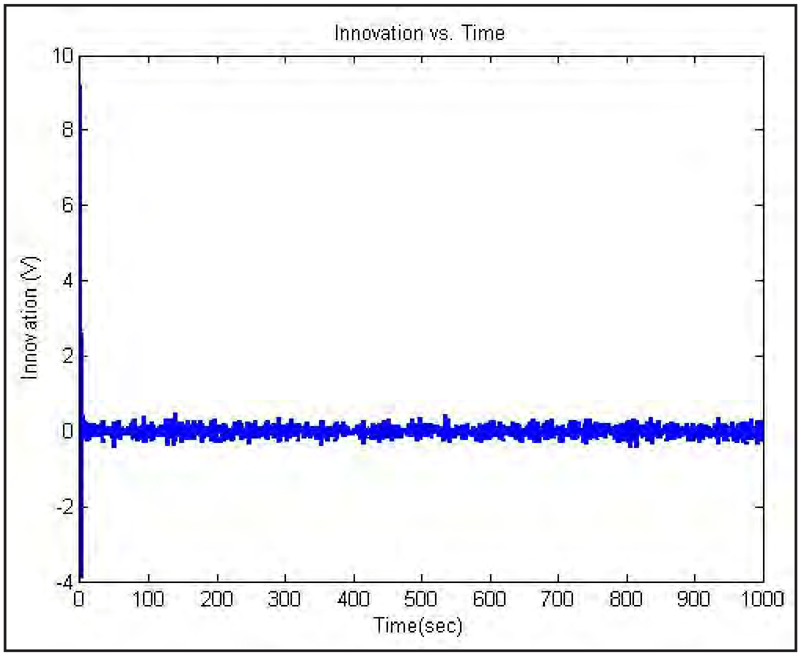

Figure 35. Evolution of the Innovation Term with Time

Figure 36 shows a comparison of the estimated SOC with the actual SOC obtained from the battery model. The initial estimation error of ~10 percent is rapidly corrected, and the estimate closely matches the actual SOC.

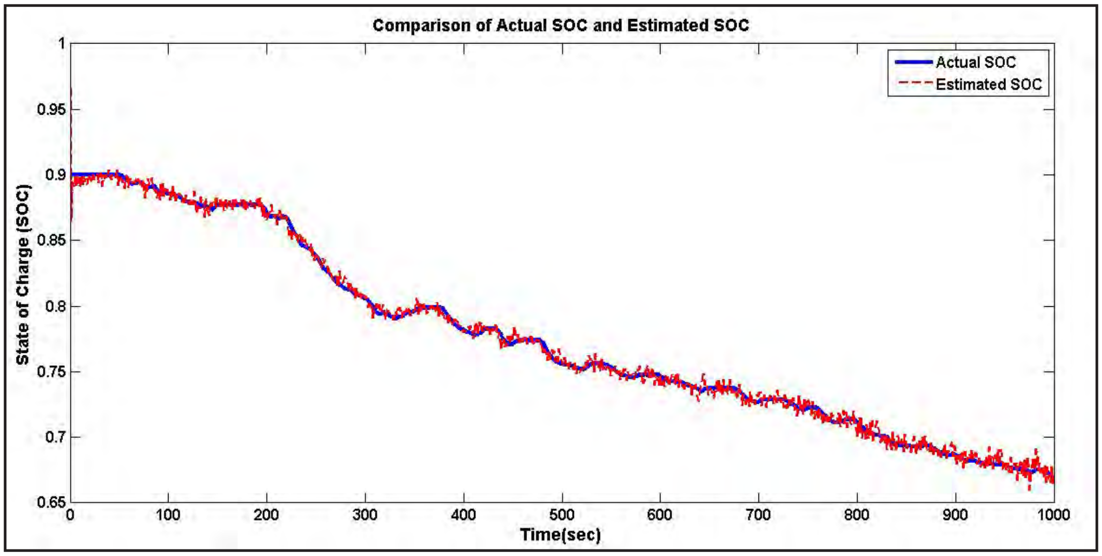

Figure 36. Comparison of Actual SOC and Estimated SOC for FUDS Cycle

Figure 37 plots the evolution of the estimation error with time. The error starts at ~10 percent and settles to under ~2 percent in the 20 seconds of operation. It then remains within these limits throughout the drive cycle. Further, the moving average of the estimation error is ~0 percent across the entire drive cycle. This is important because it is the moving average of the SOC estimate from the EKF that will be used for downstream decision and control logic.

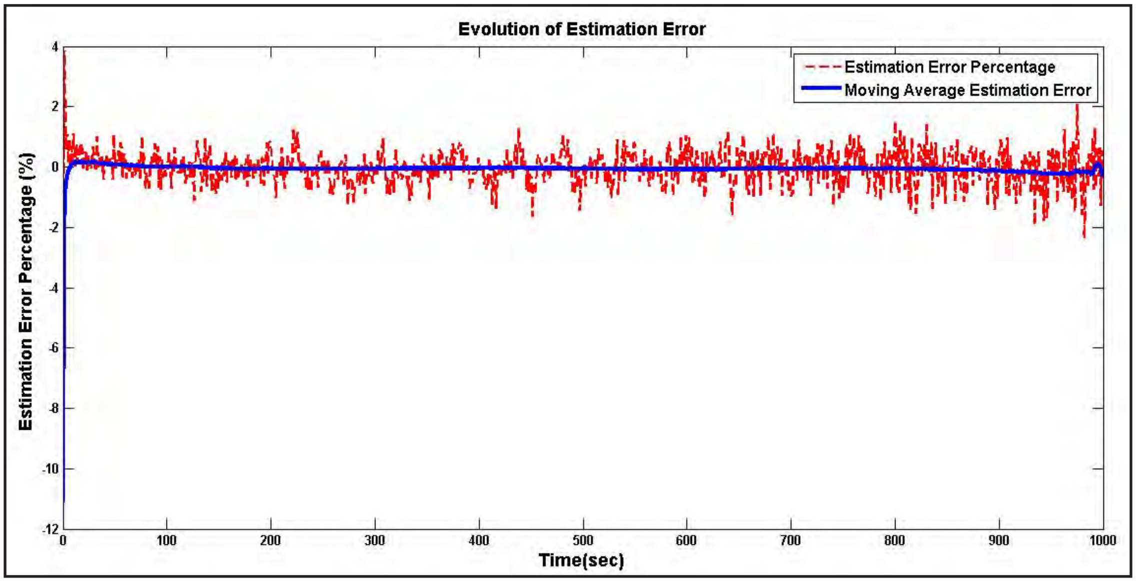

Figure 37. Estimation Error and Its Moving Average over FUDS Cycle

VII. THERMAL TESTING

The research team performed extensive thermal testing to feed into a physics-based empirical model. This chapter covers the testing, setup, and procedures, while the next chapter discusses the model developed from this testing.

Figure 38 details the general layout of the battery system being investigated. As discussed above, the system is made of eight modules connected electrically in series. As seen in Figure 38, the thermal load is broken into two symmetrical four-module strings, all with in the same metal enclosure. This battery system relies on liquid-cooled plates and conduction from the battery modules through a thermal connection to a heat sink within the liquid-cooled battery enclosure.

BATTERY PACK LAYOUT

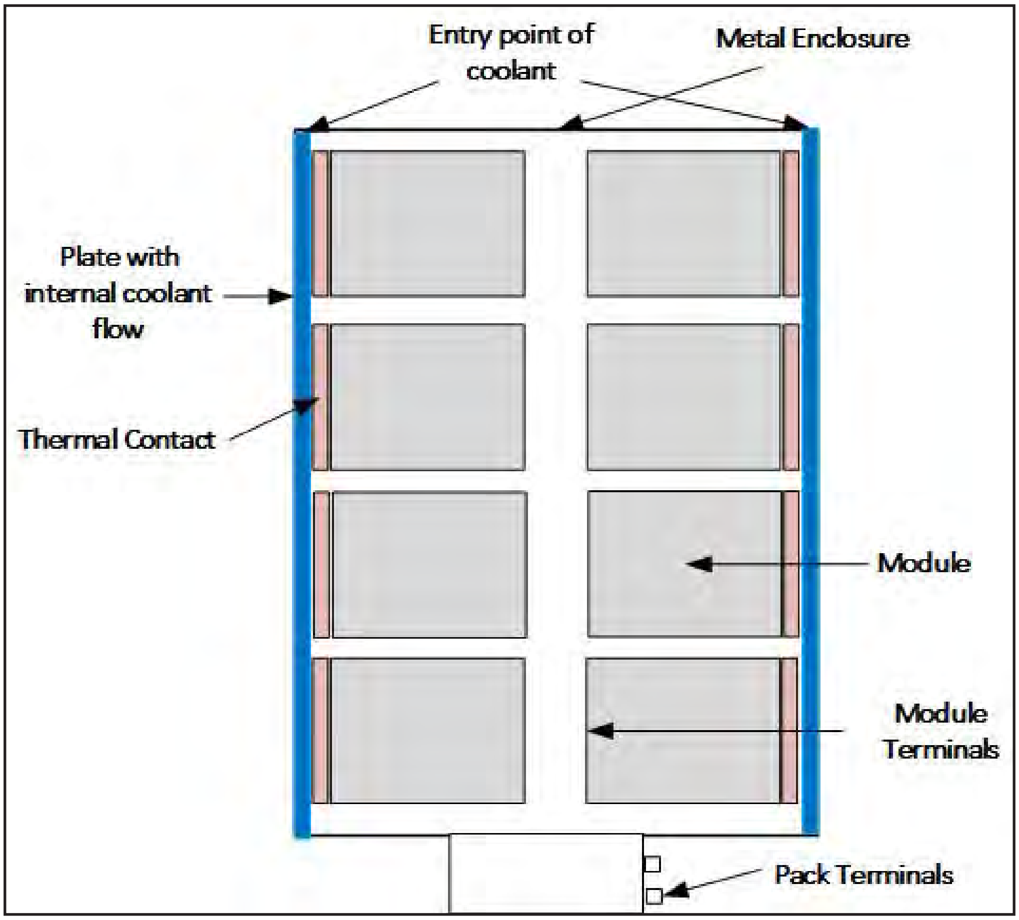

Figure 38. Battery Pack Layout

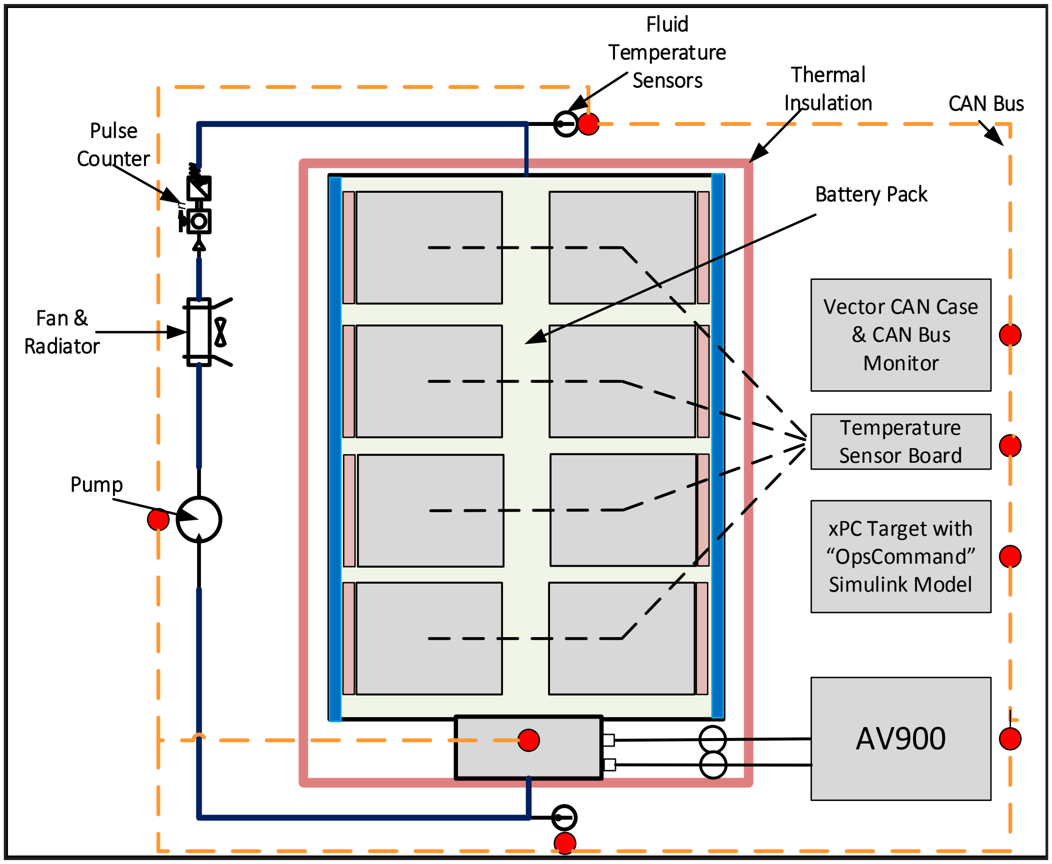

Figure 39. Experimental Setup

Figure 39 details the entire thermal test setup. As discussed earlier, the battery pack is a liquid-cooled system with a pump, fan/radiator, and flow sensor comprising the coolant loop. Note that during specific phases of thermal testing, thermal insulation was installed to eliminate transfer due to any mechanism other than the liquid coolant loop. The electrical loading is as described in chapter 1, a direct connection to the AV900 power processing machine, while data acquisition is executed through CAN bus communication of the temperature scanners, xPC, and CAN data logger.

TEST PHASE 1 – BATTERY PACK CYCLING

Description of Test

The first set of tests involved exercising the fully insulated battery pack with a two-minute time period, square wave type current signal of 2C amplitude. Fifteen counts of this square wave type current trace were applied to the pack through a test that lasted roughly 30 minutes. During this test, the cooling system was being operated according to specifications, i.e., using 50 percent ethylene glycol at a steady flow rate of two gallons per minute.

Figure 40 shows the current trace that was used to exercise the pack during this test.

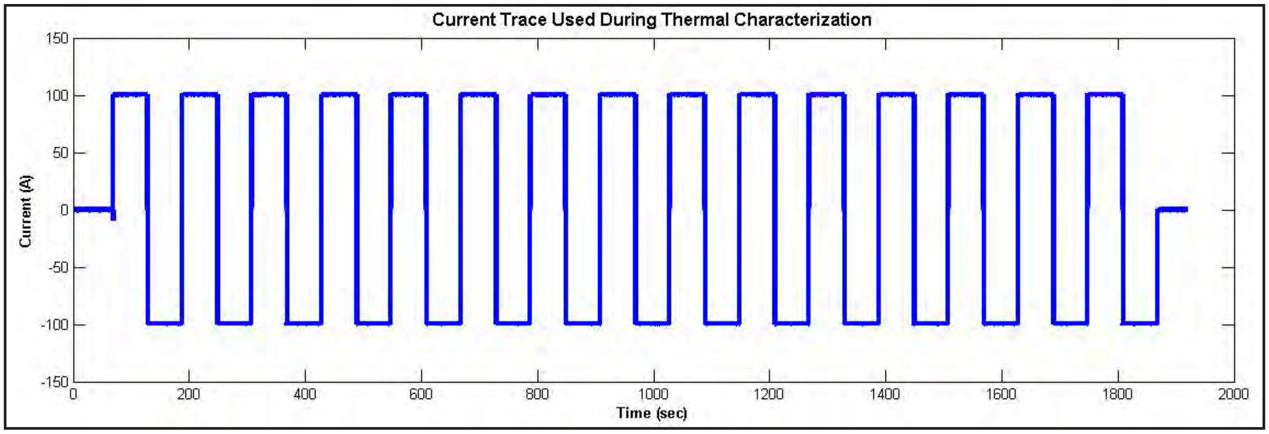

Figure 40. Load Profile Used for Thermal Characterization Testing

Thermal insulation was installed around the pack to ensure zero thermal interaction between the pack and the surrounding environment. All the heat generated from the pack was retained inside the pack or removed from it by the cooling system only.

During this testing, all sensor data were recorded. Some key data traces of importance include coolant temperature at the battery pack inlet and outlet, temperatures of different locations on the cooling plate, temperatures near the terminals of the modules, etc.

Observations

Analysis and processing of the test data provided some valuable insights into the pack’s thermal behavior. The results from the data analysis served to characterize the pack’s behavior, and it provided a strong basis for some of the assumptions that have been made in developing the thermal model in the following chapter. The next section elaborates on some of the key observations from the above-described tests.

Coolant Temperature

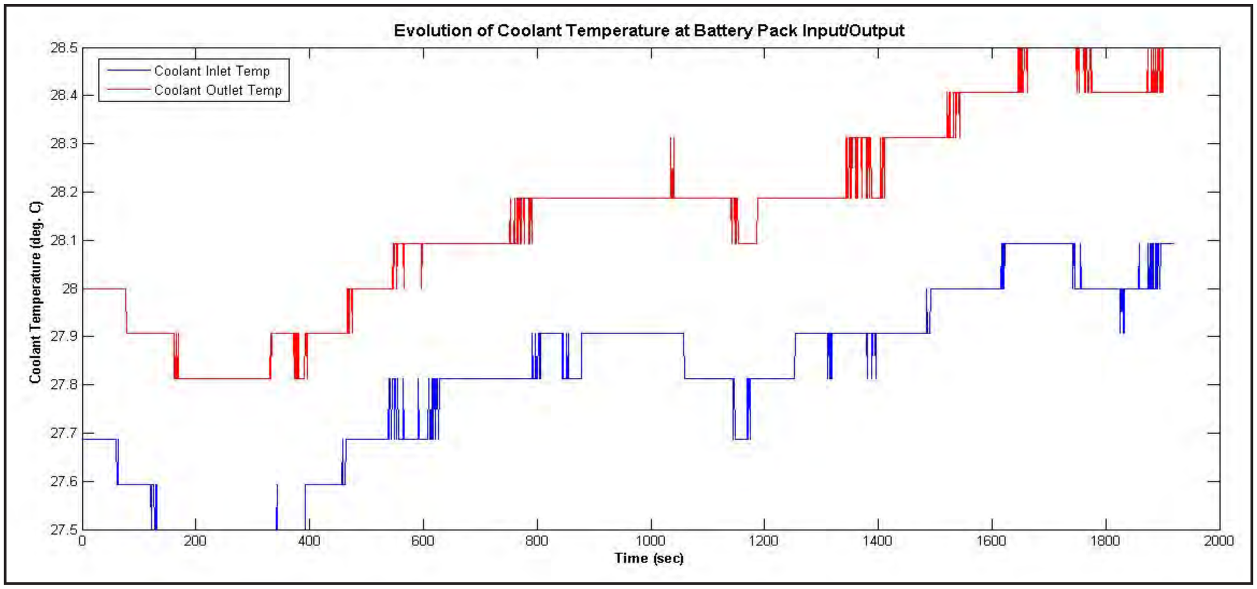

Figure 41. Coolant Temperature Variation at Pack Inlet and Outlet during a Single Test

RTD temperature sensors were used to record temperature of the coolants at the battery pack inlet and outlet. These measurements can be seen in Figure 41. Note that throughout the entire test, a nearly constant temperature difference was seen between the battery pack inlet and outlet. Also, the temperatures at both the coolant inlet and outlet increased during the course of the test, as expected.

A slight decrease in coolant inlet temperature was noticed in the initial few minutes of the test. This may be due to the pump being started just at the beginning of the test, and the moving coolant fluid is expected to affect the temperature detected by the sensor probe.

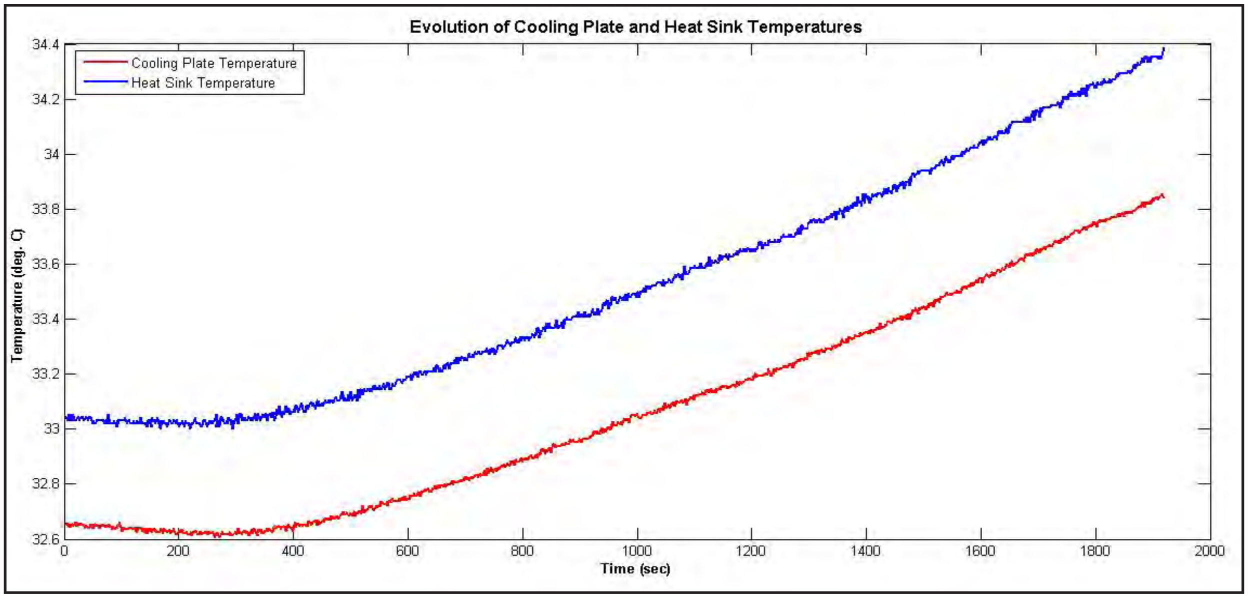

Figure 42. Evolution of Heat-Sink and Cooling-Plate Region Temperatures

Figure 42 shows traces of average cooling plate and heat sink temperature. The temperature traces from all sensors located on the cooling plates and heat sinks were averaged to obtain these traces. Average values were taken to show a representative trace. This was sufficient to understand the temperature and heat transfer characteristics in these two zones of the battery pack.

Both temperature traces show a significant increase in temperature by ~1.4°C during the test.

There is a nearly constant temperature difference between the heat sink and cooling plate regions. Two important conclusions can be drawn from this. First, the nearly constant temperature difference indicates near-perfect conduction between the two regions. Second, it indicates the existence of a sharp thermal gradient between the two regions.

It is important to notice that the temperature increase, while noticeable, is not very high compared to other regions in the pack. This is because there is a strong heat removal effect at the cooling plate due to convective heat transfer to the coolant. Further, there is a strong conduction effect from the heat sink of a module to the liquid-cooled plate.

Temperature Distribution across the Pack

Figure 43 is a top-view representation of the pack with a temperature distribution overlaid upon it. The graph shows spatial distribution of the temperature rise between the start and end of the test.

Temperatures were recorded using an array of temperature sensors placed across the pack. A cubic spline interpolation scheme was utilized to generate the distribution seen in Figure 43.

It is important to note that while the plot shows a continuous temperature distribution, a thermal contact, other than air, does not exist between two separate modules (Figure 38). Thus, conductive heat-transfer set up by these gradients can exist only in the lateral direction from the centerline of the pack toward either edge.

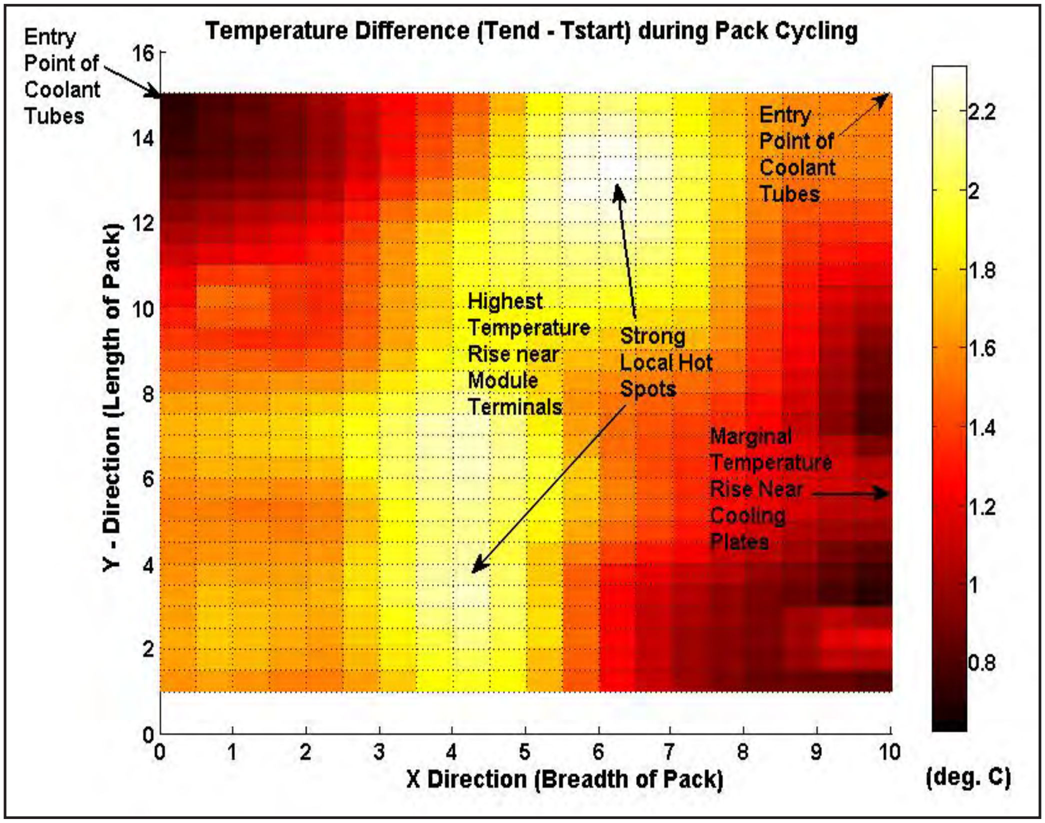

Figure 43. Spatial Distribution of Temperature Rise between Start and End of Test

As seen in Figure 43, the temperatures are the highest along the centerline of the pack. This is expected, as both electrical module terminals, + and -, are located along the same module face as well as the centerline of the pack. Typically electrical terminals are where the majority of the heat generation is expected to take place, especially in this case, as they are on the same face of the module, unlike a module with opposing terminals. Fundamentally, the module follows cell geometry, and this behavior propagates from the physical configuration of the cell to the module enclosure.

The lowest temperatures occur at the top corners of the pack. These are the zones in which the cooling fluid enters the cooling plates and is at its lowest temperature and fastest flow rate. Thus, the heat extraction is expected to be strongest here; hence, the lower temperatures.

In keeping with the above observation, temperature hot spots (~43°C) occur near the lower part of the graph along the centerline. This is the region nearest to the module terminals and farthest away from the entry of the coolant into the battery pack. This region is expected to show the highest temperature rise during operation.

It is important to notice the range of temperature across the pack, which is roughly 8°C. Given this wide temperature range, it is important to study all temperature dynamics in the module and not just work with a “bulk” pack temperature. This is covered in the next chapter and is the justification for modeling both minimum and maximum pack temperature nodes of the system.

Figure 44 shows surface plots of the temperature distribution across the pack at the start of the test and at the end of the test. This graph gives important insights into the rate and magnitude of temperature increase in different regions of the pack. Figure 45 shows a comparison between the two spatial distributions, in the top view. Note that both plots have been generated using a cubic spline interpolation scheme from the data measured by the battery pack’s internal temperature sensors. The approximate locations of these sensors are indicated by markers on the graph.

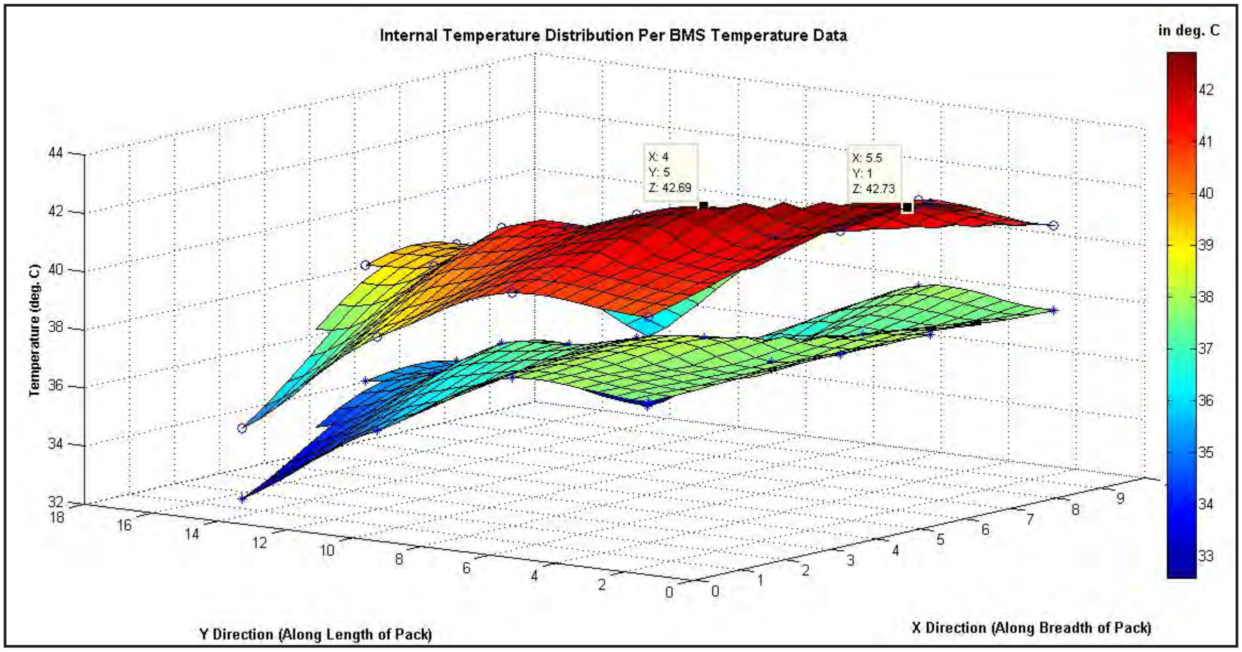

Figure 44. Internal Temperature Distribution at Start and End of Test

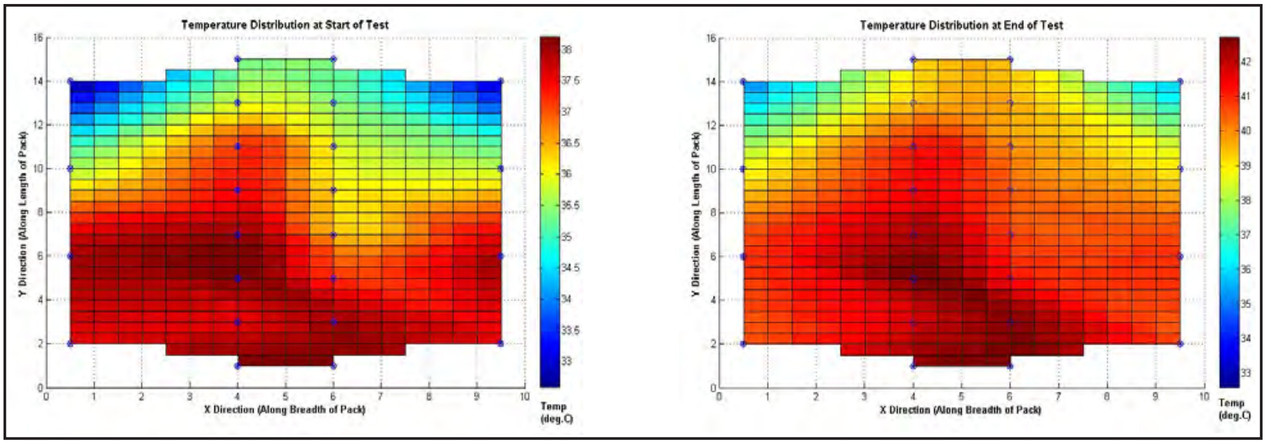

Figure 45. Temperature Distributions at Start and End of Test

Temperature increase is significantly higher at the center of the pack than in the region near the cooling plates. The region near those plates consists of strong conductors, and there is a heat extraction effect from the cooling system. Further, it is not the primary heat source in the pack. That primary heat source is near the module terminals, which are located along the pack centerline. Consequently, the lower temperature increase and the modest rate of temperature increase are expected.

The magnitude and rate of temperature increase is highest in the region farthest away from the entry point of the cooling tubes. Once again, this is expected because the heat removal from the cooling system is marginally lower, and heat sources are located in this region.

It is thus important to capture the temperature and heat-transfer dynamics of this region accurately, especially in the high-temperature regime. This region is thus a significant zone of interest from the perspective of the thermal mode.

Evolution of Temperatures in Important Regions of Battery Pack

To obtain an overview of the temperature evolution in different regions of the pack, a spatial average of temperature data from different sensors located in a particular region of the pack was taken, and a time trace was plotted. As shown in Figure 46, this was done for the regions near the module terminals, the region inside the module near the heat sink, the exterior region of the heat sink, and the cooling plate and the coolant.

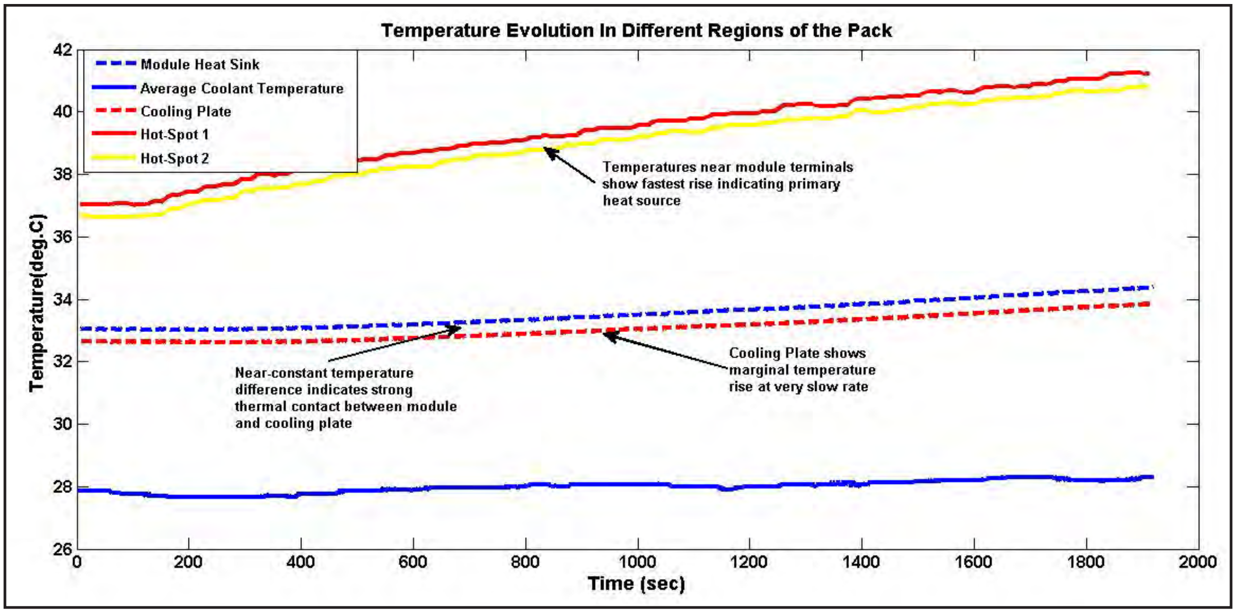

Figure 46. Temperatures in Different Regions of the Battery Pack

As expected, the regions near the module terminal showed the fastest rate of temperature increase.

The region inside the module near the heat sink also had a noticeable rate of temperature increase. However, it was the lesser when compared to the region near the terminals. This is attributed to the heat conduction from the terminals, which are the primary heat source region, all the way to the module heat sinks.

The temperature gradient of the heat sink and cooling plate region is similar to that of the heat sink region inside the module. This indicates a strong conduction heat transfer between these regions. This is attributed to the fact that these regions are plates of aluminum in thermal contact with each other through highly conductive filling materials. The efficacy of these materials and the systems design is validated by this observation of the thermal gradients.

Last, the average coolant temperature shows a marginal increase during the test. This indicates that the radiator system used to extract heat from the coolant is unable to remove all the heat the coolant has extracted from the pack. While the temperature increase is only marginal in this case, it is expected to be significant during longer operations and may be a cause for concern.

TEST PHASE 2 – BATTERY PACK COOL DOWN

Description of Test

The second phase of thermal testing involved allowing the fully insulated battery pack to cool down using only the cooling system in a pseudo-adiabatic scenario. For this testing phase, the battery was completely insulated with a two-inch thick R-10 rated insulation sheathing. During this test, the cooling system was operated according to manufacturer specifications, i.e., using a 50/50 mixture of ethylene glycol and water at a steady flow rate of two gallons per minute. Because the pack was thermally insulated from the surrounding air, it is assumed that all heat extraction from the pack took place through the cooling system only. Figure 47 shows the insulated battery and cooling tubes carrying the 50/50 mixture of ethylene glycol and water.

Figure 47. Insulated Battery

As before, all sensor data were recorded during the test. Some key data traces of importance include coolant temperature at the battery pack inlet and outlet, temperatures of different locations on the cooling plate, temperatures near the terminals of the modules, etc. All data were recorded for approximately 2,400 seconds, or 40 minutes.

The primary objective of this test was to observe and capture the temperature and heat transfer dynamics at work in the pack during the cool-down process. The dynamics of the cool-down process were a key factor in determining the best approach to modeling the thermal behavior of the pack, and hence their understanding was critical. It was also important for validating the efficacy of the cooling system design.

Observations

Analysis of the test data brought forth several important insights that were not intuitively obvious. These insights heavily dictated the approach used to model the pack's thermal behavior. The following section discusses some of these key observations.

Temperature Distribution across the Pack

As completed for the first phase of the test, the temperature distributions are represented as a surface plot. In Figure 48, the upper surface shows the distribution at the start of the test, and the lower surface shows the distribution at the end of the test. The markers on the graph indicate the location of the temperature sensors. MATLAB's 2-D cubic spline interpolation scheme has been used to generate the surface plot.

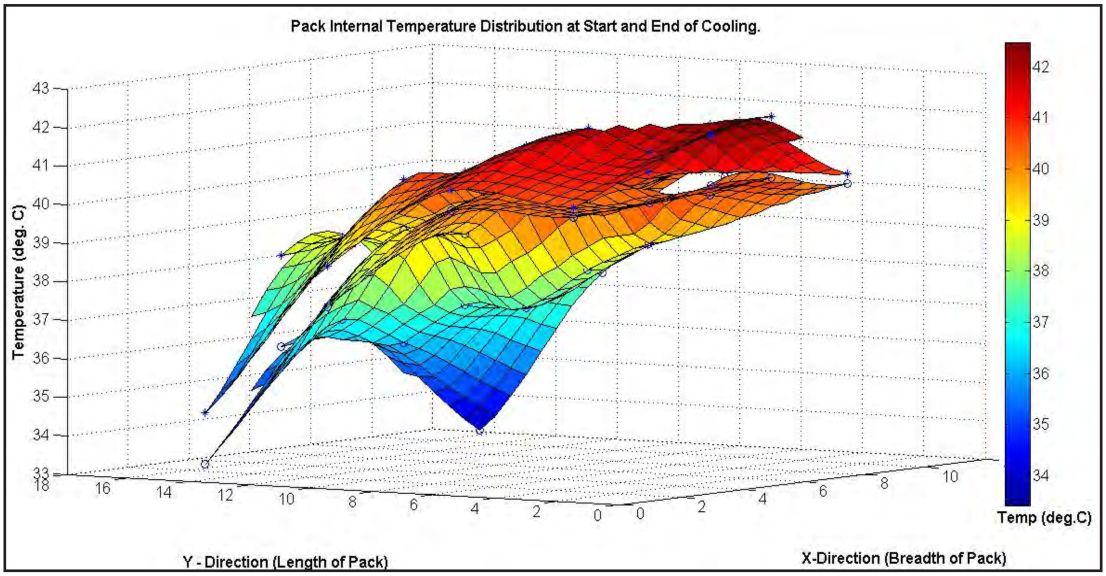

Figure 48. Temperature Distributions at Start and End of Cooling

Furthermore, Figure 49 shows the temperature distributions at start and end of cooling tests, in the top view.

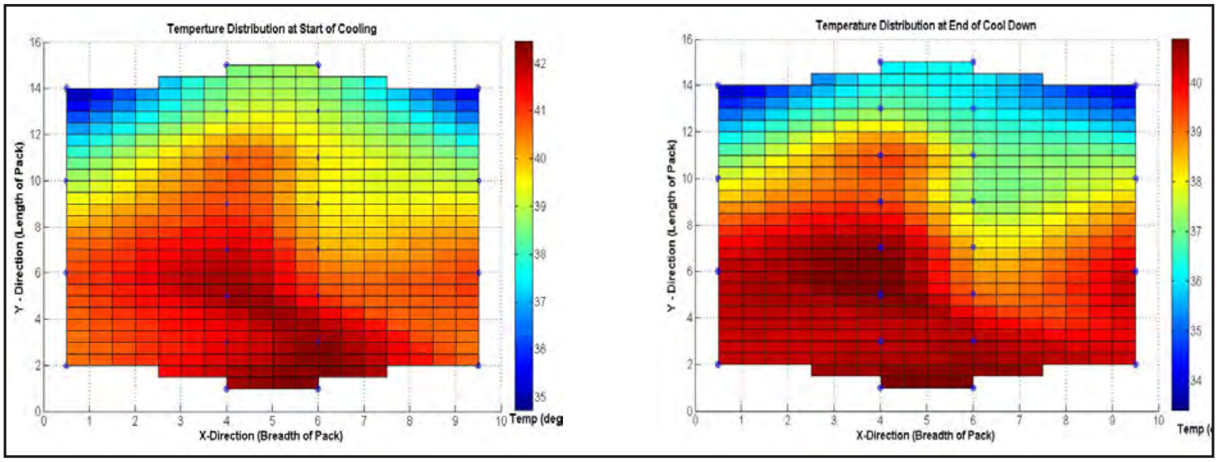

Figure 49. Temperature Distributions between Start and End of Cooling

Figure 50 shows another representation of the temperature change during the cool-down process. The plot shows the spatial distribution of the temperature drop the cool-down process. Several inferences can be derived from studying these spatial distributions, as described in the following section.

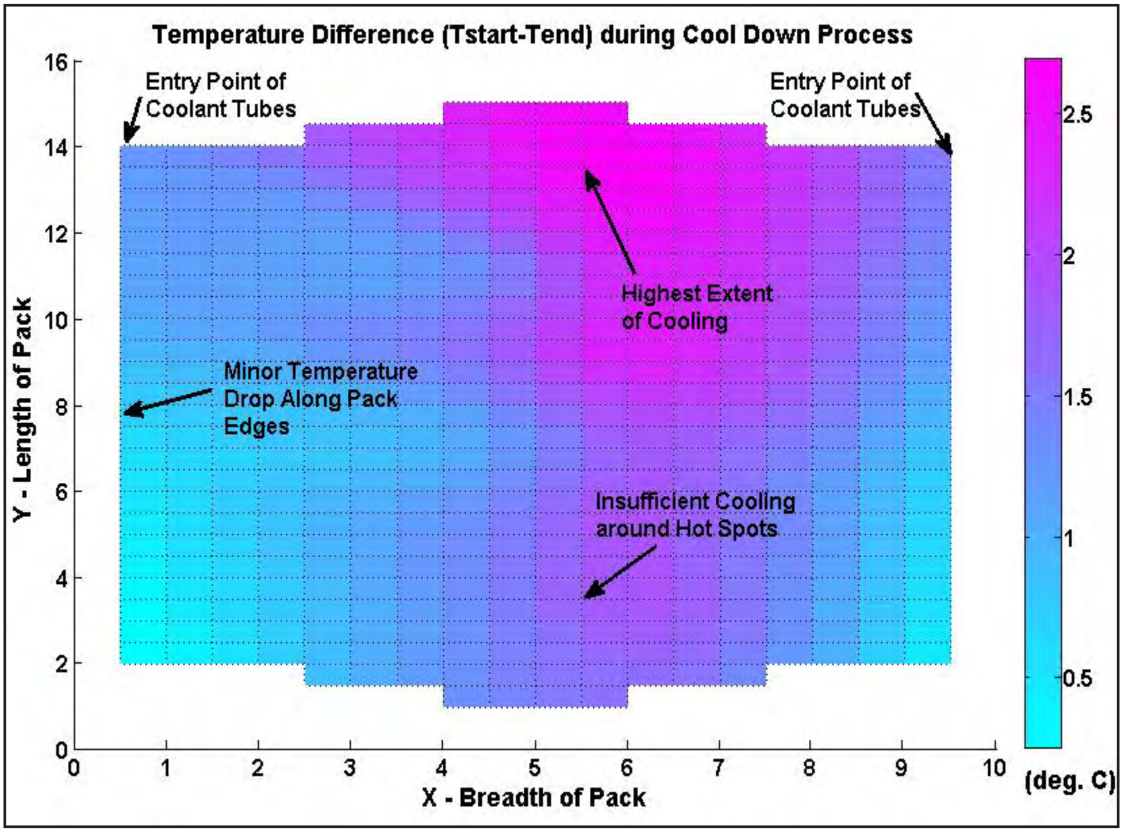

Figure 50. Spatial Distribution of Temperature Drop during Cooling

It is clear that the drop in temperature is the least near the edges of the pack closest to the cooling system/cooling plates. This is expected because the temperature rise in this region, during battery cycling, is much less than in other parts of the pack.

The cooling system extracts heat from the region of the pack closer to the entry-point of the cooling tubes more effectively than from the region farther away. As described previously, this is expected behavior.

Most noteworthy is the difference in temperature drops between different locations on the battery pack centerline. The region closer to the end of the pack where the cooling tubes enter shows a much higher temperature drop (~2.5°C in 40 minutes) as compared with points further down along the centerline.

Thus, the rate of cool-down appears to be lowest near the hot spots (~0.5°C in 40 minutes) described previously. This is a cause for concern during prolonged operation of the pack in urban environments, where small bursts of aggressive charging and discharging are expected, with very little cool-down time.

Evolution of Temperature in Important Regions of the Pack

As completed previously, to obtain an overview of temperature evolution in different regions of the pack, a spatial average of temperature data was taken from multiple sensors located in a particular region of the pack. This time trace was plotted, as shown in Figure 51. This was done for the regions near the module terminals, the region inside the module near the heat sink, the exterior region of the heat sink, and the cooling plate and the coolant.

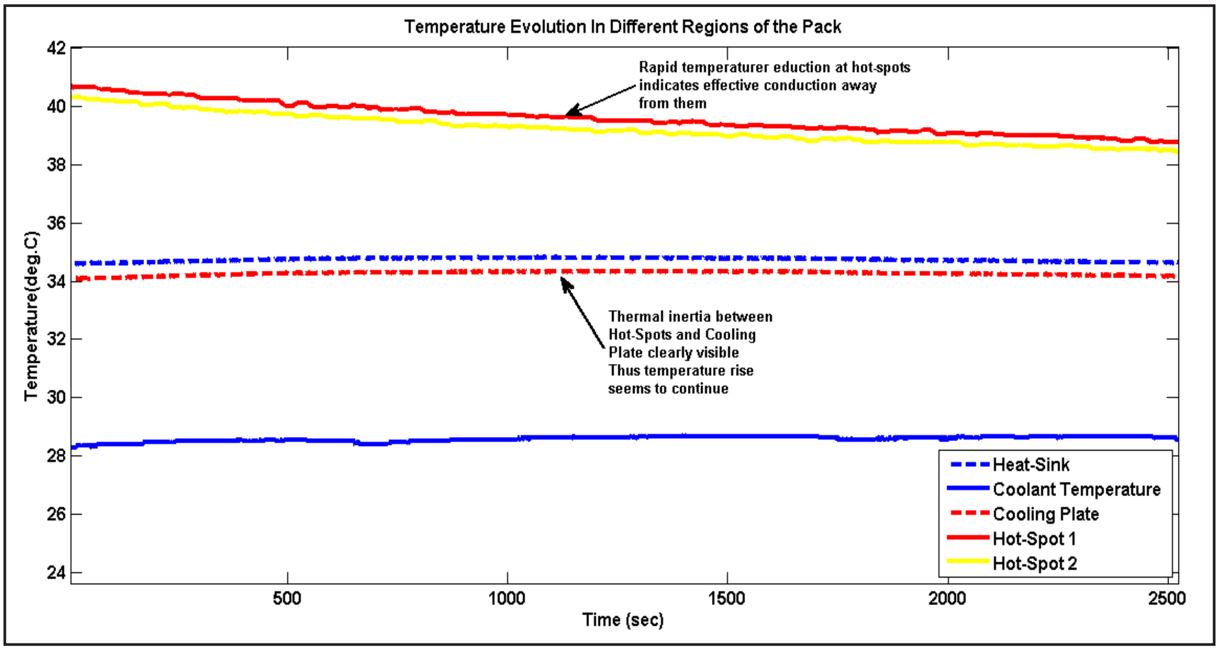

Figure 51. Temperatures in Different Regions during Pack Cool-Down

The region near the module terminals immediately shows decreasing temperatures as soon as cycling of the battery pack has been stopped. This is expected because the primary reason for temperature rise was Ohmic heat generation, which has stopped. Now there is only conductive heat transfer away from this region toward the module's heat sinks.

It is important to note that the temperature decreases faster initially, and the rate reduces with time. This is typical of this type of cool-down process. It is consistent with the exponential temperature decay that is expected as per a first principle analysis.

An extremely noteworthy observation is that the temperature of the heat sink and cooling plate continue to rise for nearly 15 minutes even after cycling of the battery pack has been stopped. This phenomenon is clearly illustrated in Figure 52. While this is not immediately intuitive, it is expected behavior.

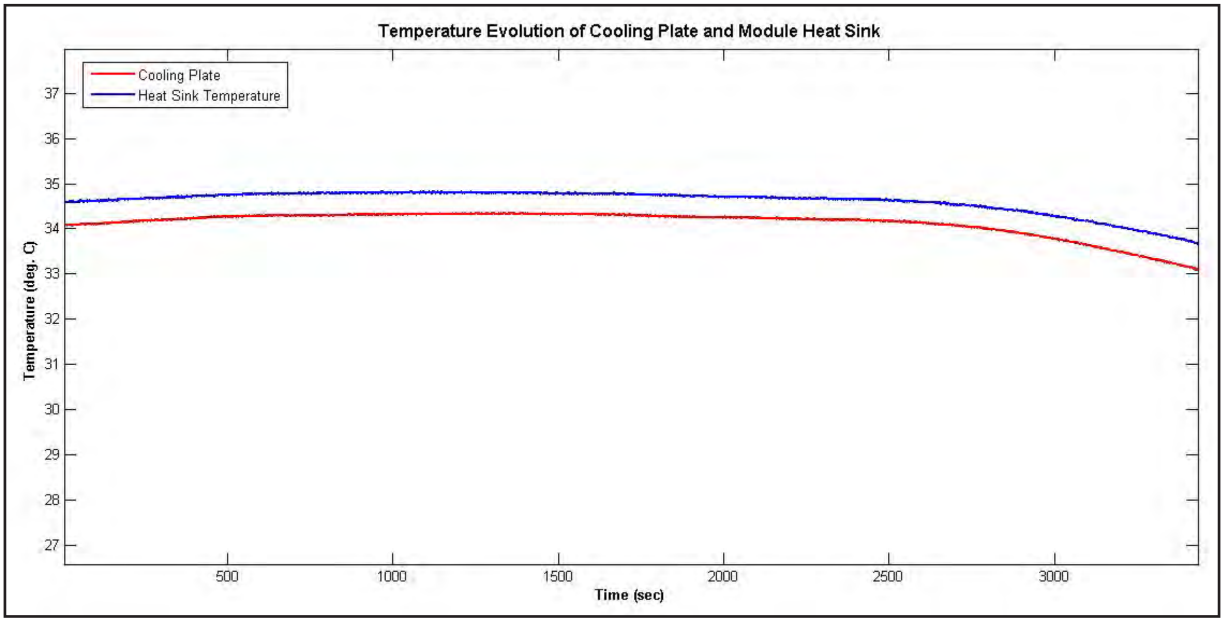

Figure 52. Cooling Plate and Module Heat Sink during Cooling

Heat continues to be conducted into the heat sink due to the thermal inertia between the module terminals and the heat sink/cooling plate region, even after the cycling has stopped. This is the heat that was transferred away from the module terminals. Heat is then conducted into the cooling plate, where it is removed by the coolant.

This behavior prevents the temperature of the cooling plate and heat sink from decreasing immediately after the cycling has stopped. The temperatures first continue to rise, then flatten out, and then start dropping. The time constant of this process depends on a variety of factors ranging from module location, hot-spot temperature, coolant temperature, C-rate at which the pack was cycled, etc.

It is thus imperative to develop a first-principle-based thermal model that is able to capture these complex dynamics accurately and reliably.

VIII. THERMAL MODEL

A thermal model was built and validated, building upon the testing results above and a system understanding, as well as on desired estimation requirements. The details of this work are discussed in this chapter.

Modeling the Convective Heat-Transfer Coefficient

A key physical parameter affecting the performance of the battery pack and cooling system is the convective heat transfer coefficient between the cooling plate and the coolant fluid. It was extremely important to validate the theoretical value of this parameter, used during the design process. Further, it was important to reliably establish this value, as it would be a parameter of significant importance in any modeling effort.

The temperatures of the coolant at the battery pack inlet and outlet were measured. The flow rate of the coolant was set at two gallons per minute but was measured throughout the test, as shown in Figure 53.

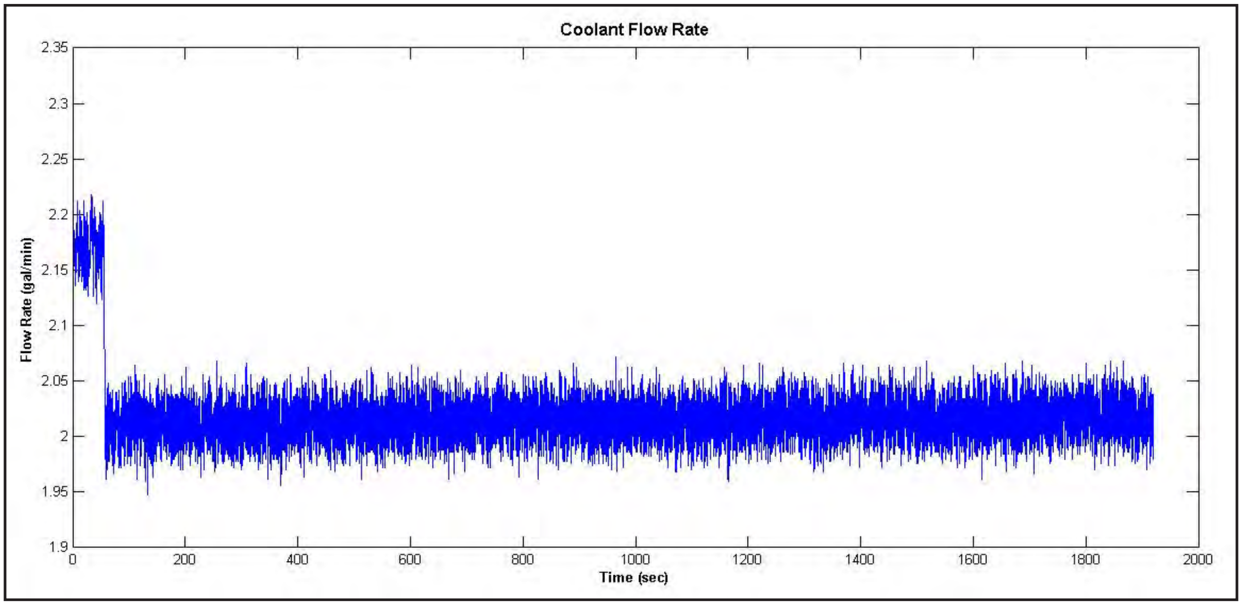

Figure 53. Measurement Trace of Coolant Flow Rate

Using these two traces of data – temperate and flow rate – it was possible to calculate the heat energy extracted from the pack by the cooling system, per unit time. Figure 54 shows a plot of the heat energy extracted. The variations in the plot are due to variations in the signals obtained from the sensor recording coolant inlet and outlet temperatures.

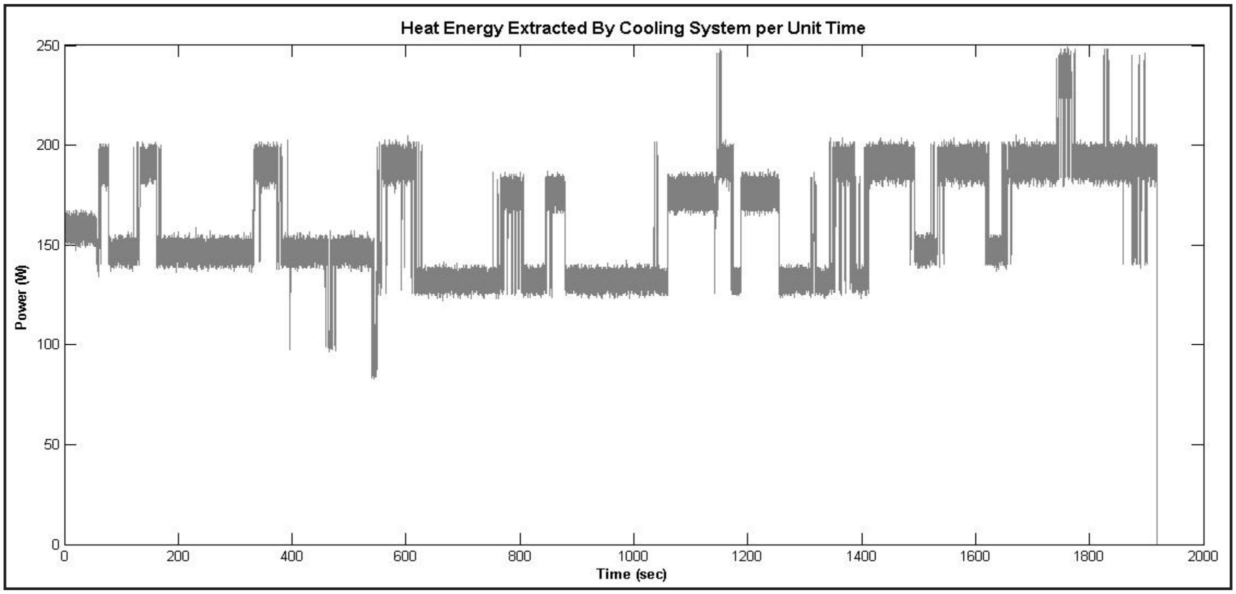

Figure 54. Power Extracted by the Coolant over a Single Test

Given that the coolant temperature was measured at only two locations, the average value of these was used as the representative temperature of the coolant for further analysis. Convective heat transfer takes place along the entire length of the cooling tube. Several temperature sensors were located along the cooling plate. A spatial average of the temperatures recorded by these sensors was used to represent the temperature of the cooling plate. The trace of this average was the trace of the cooling plate temperature in the previous chapter.

The value of convective heat transfer coefficient was extracted using the trace of the heat energy extracted per unit time, the representative temperatures of the coolant and the cooling plate, and information about the geometrical construction of the cooling tubes. The following equation is used for this computation:

$$h_{conv} = \frac{\rho . f . Cp . (T_{out} - T_{in})}{A_s T_{LMTD}} \; where \; T_{LMTD} = \frac{\Delta T_o - \Delta T_i}{\ln(\frac{\Delta T_o}{\Delta T_i})} \qquad (27)$$

where,

p = Coolant Density

f = Coolant Flow Rate

Cp = Coolant Heat Capacity

(T_{out} - T_{in}) = Coolant Temperature Rise

A_s = Area of heat-exchange

Figure 55 represents the convective heat-transfer coefficient versus time. As before, the variation is introduced due to the characteristics of the temperature sensors used and the fact that online filtering of the sensed temperature data was not performed during the test.

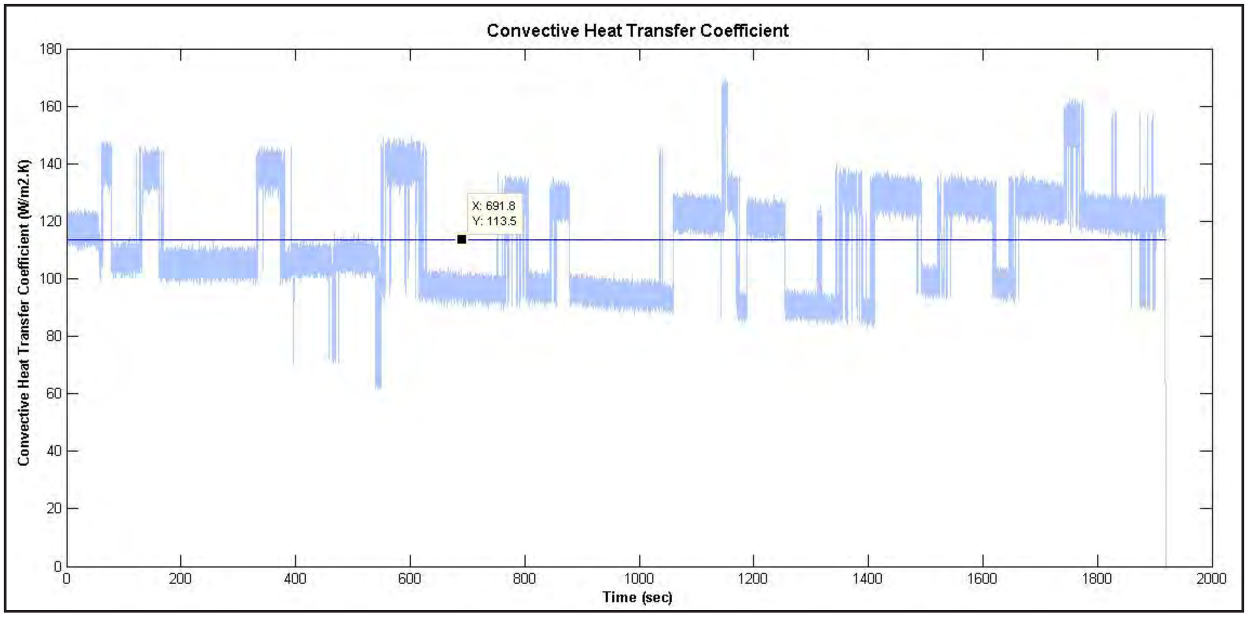

Figure 55. Heat Transfer Coefficient Measurements

Thus, averaging the results, we can say that the convective heat transfer coefficient value is 113.5 W/m^{2}K. This value is used in the modeling work described later in the report.

Modeling the Heat-Transfer Dynamics

Heat transfer across the battery pack system is not expected to be steady state, but instead, transient. Transient models are numerically complex and involve parameters that cannot be estimated readily from real test data. Thus, transient heat-transfer dynamics are often captured using lumped capacitance models.

Lumped capacitance models are valid only under certain conditions. Specifically, the time constants associated with the “lumps” must be much faster than those associated with the heat transfer between the lumps.

A test was run in which the battery pack was allowed to cool down with the influence of the cooling system, and the temperature evolution of a single module terminal and its corresponding cooling-plate location was analyzed. It appears that a lumped capacitance model is accurately able to capture the temperature response of the two locations, as shown in Figure 56.

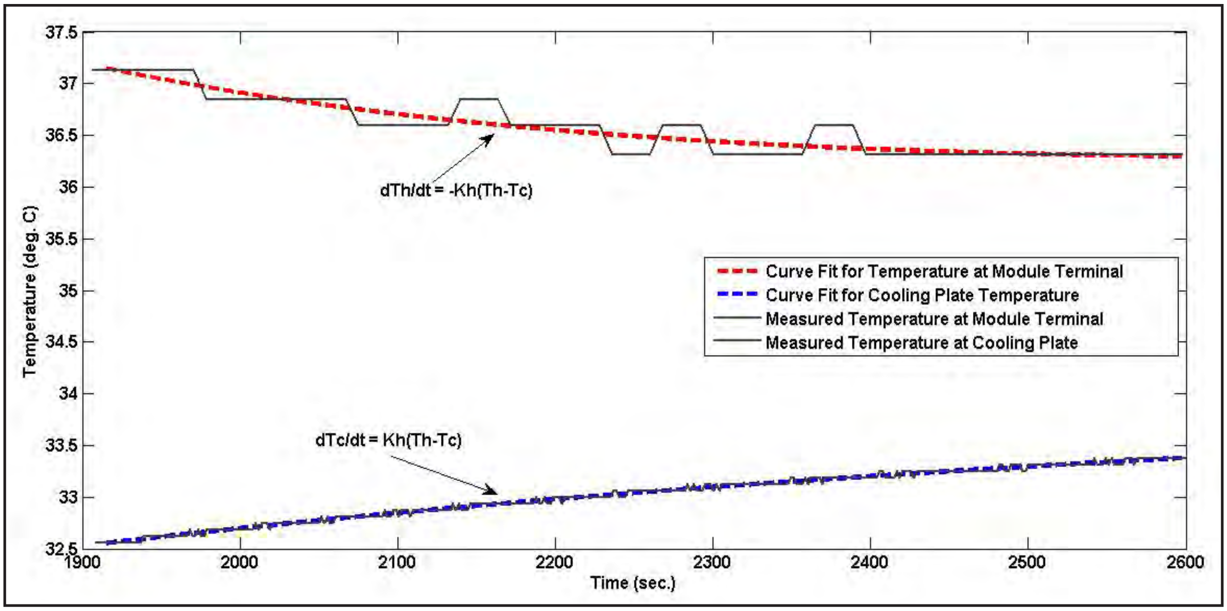

Figure 56. Module Terminal and Cooling Plate Temperature Response

Thus, the following differential equations accurately capture the unforced temperature dynamics of the module terminal (hot-spot) and its corresponding cooling plate region.

$$\frac{dT_c}{dt} = (T_h - T_c)\frac{A}{B} \tag{28}$$

$$\frac{dT_h}{dt} = -(T_h - T_c)\frac{A}{D} \tag{29}$$

Figure 57 shows the lumped-node model of a single module. Here, Ohmic power generated is at the module terminals. It is conducted toward the cooling plate. At the cooling plate, this convective heat-transfer exists between the cooling plate and the coolant. Furthermore, it is observed empirically that the dynamics of the cooling plate temperature are orders of magnitude slower compared to those of heat transfer to the coolant. Thus, the heat transfer to the coolant can be treated as taking place under steady-state wall temperature boundary conditions.

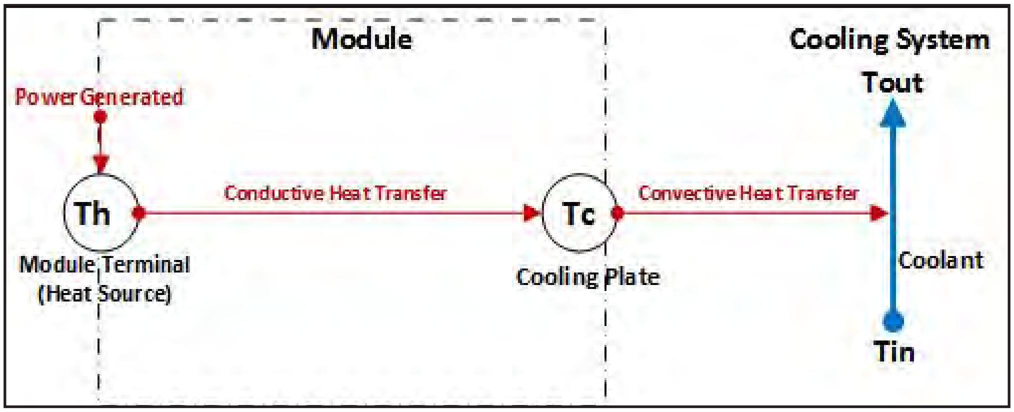

Figure 57. Lumped-Node Thermal Model of a Single Module

Thus, the governing equations for this model are as shown below:

$$\dot{Q}_{generated} = I^2 ESR \tag{30}$$

$$\frac{dT_h}{dt} = \frac{\dot{Q}_{generated}}{Cap_H} - (T_h - T_c)K_H \tag{31}$$

$$\frac{dT_c}{dt} = (T_h - T_c)K_C - \frac{\dot{Q}_{removed}}{Cap_C} \tag{32}$$

The heat transfer to the coolant is modeled using the following equations of a standard heat exchanger at steady state:

$$(T_c - T_{out}) = (T_c - T_{in})\, e^{\left(\frac{-h_{conv}As}{\rho C_p f}\right)} \tag{33}$$

$$\dot{Q}_{removed} = h_{conv}As(T_{out} - T_{in}) \tag{34}$$

All symbols have the usual meaning. $\dot{Q}_{generated}$ is the Ohmic power generated by the respective module. $\dot{Q}_{generated}$ is the thermal power extracted by the cooling system.

The parameters $K_C, K_H, Cap_C, and\ Cap_H$ have been extracted from the test data using a parameter estimation task setup in Simulink®. The Trust-Region-Reflective Least Squares Optimization (The MathWorks, 2013) was used for this parameter identification using the measured temperature response data from different types of thermal characterization tests conducted by the research team. Due to the large number of parameters to be estimated and the large size of data-sets, the Parallel Computing Toolbox was also used to parallelize and consequently speed up the parameter estimation process.

Developing the Simulink® Implementation

The final objective was to develop a Simulink® model that is compatible with a larger “vehicle-level” model and performs the following key functions:

1. Predicts temperature evolution at strategic locations in the battery pack for different drive cycles
2. Predicts thermal gradients evolution between key points in the battery pack
3. Simulates the heat extraction system efficacy currently integrated within the battery pack
4. Provides a framework to accurately simulate different heat extraction system configurations well in advance of their actual implementation
5. Accurately simulates the irreversible Ohmic heat generated in the battery pack at all points in the expected operating range of SOC, OCV, and cell temperature

Model Overview

The model uses the following inputs:

- Current
- Coolant input temperature
- Initial values of temperature at strategic locations in the pack

It provides the following as outputs:

- Temperatures at eight strategic locations on the pack
- Maximum and minimum temperatures
- The average or bulk temperature of the pack
- The coolant output temperature
- Ohmic heat generated at each time-step
- Heat removed by the heat extraction system at every time-step

At the highest level, the model has three components, each captured in a different subsystem, namely, Ohmic heat generation, cooling system, and battery pack.

Ohmic Heat Generation

This subsystem predicts the Ohmic heat generated per unit of time based on the charge/discharge current, nominal cell temperature, and SOC at the current time instant. The SOC and nominal cell temperature are used to look up a value for charge/discharge internal resistance. This is used with the instantaneous value of current to calculate the instantaneous Ohmic power.

Cooling System

This subsystem models the process of heat extraction by the cooling system. The model implements a first principle calculation of heat extracted (by convection) by the coolant from the walls of an internal channel, and the resulting increase in coolant temperature.

Battery Pack

This subsystem uses values of Ohmic heat generated per unit of time and heat extracted by the cooling system per unit of time. It applies to them a model of the battery pack's heat transfer dynamics to predict temperatures at different strategic locations in the pack. See Figure 58 for an overview of the model.

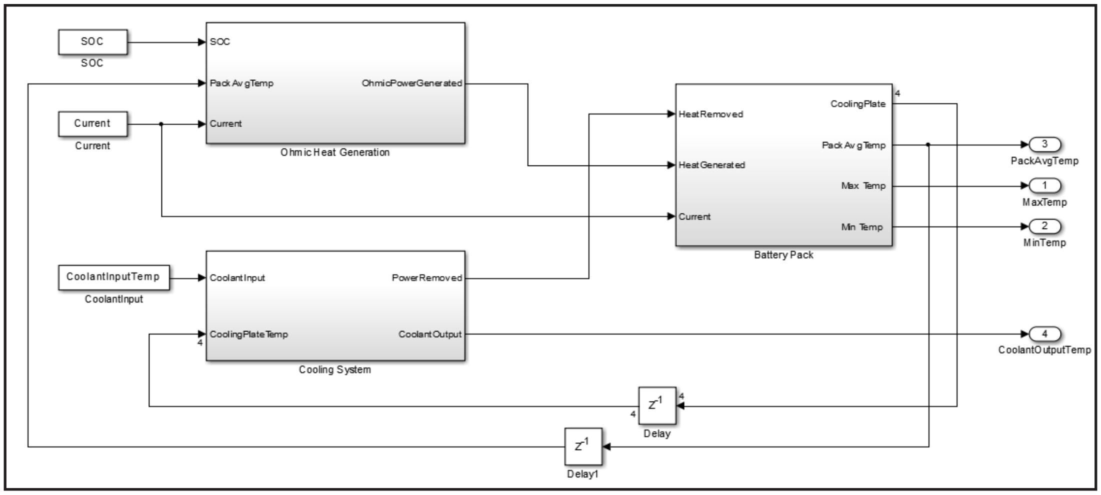

Figure 58. Thermal Model Overview

Ohmic Heat Generation

Ohmic heat (also referred to as I^2R heating) is calculated using the current and an estimate of ESR and Ohms of the pack. The ESR value is calculated from a series of lookup tables whose implementation is detailed later in this section. This ESR value is used along with the current signal (amperes) to calculate the Ohmic heat generation rate given by I^2R in Watts. Figure 59 is a snapshot of the implementation.

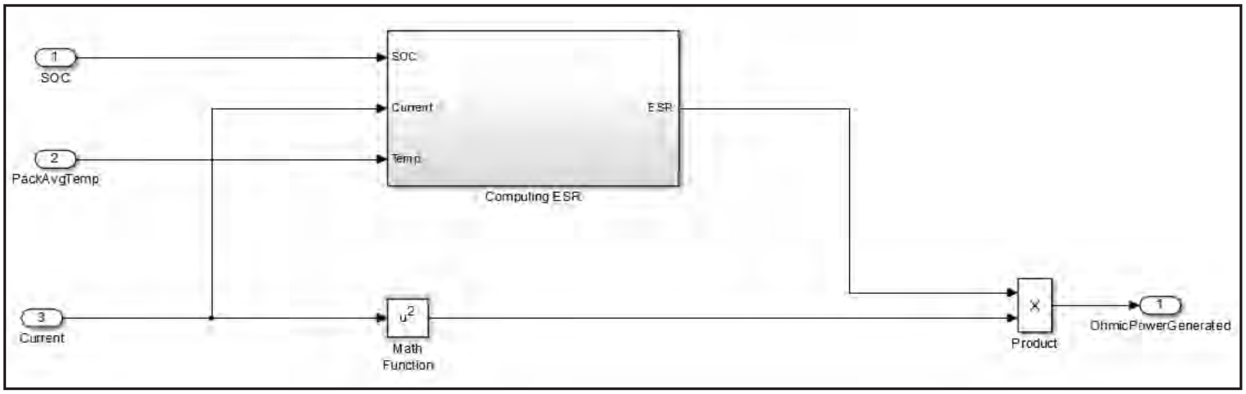

Figure 59. Ohmic Heat Generation Subsystem

The ESR is determined at every time-step based on the instantaneous current (amperes), nominal pack temperature (°C), and SOC. The SOC is used to obtain the corresponding open circuit voltage (OCV). This is done through a 1-D lookup “SOC-OCV Map.” Following this, the nominal pack temperature and OCV signal are used to obtain a value of ESR for charge and discharge, respectively. This is done using lookup tables “ESR Map Discharge” and “ESR Map Charge.” These two lookup tables are based on empirical data and are elaborated upon in the next section. Next, the sign of the current signal is checked to determine whether the pack is being charged or discharged. Depending on whether charge or discharge is taking place, the value obtained from the ESR map charge or ESR map discharge is used as the instantaneous value of ESR. This implementation is shown in Figure 60.

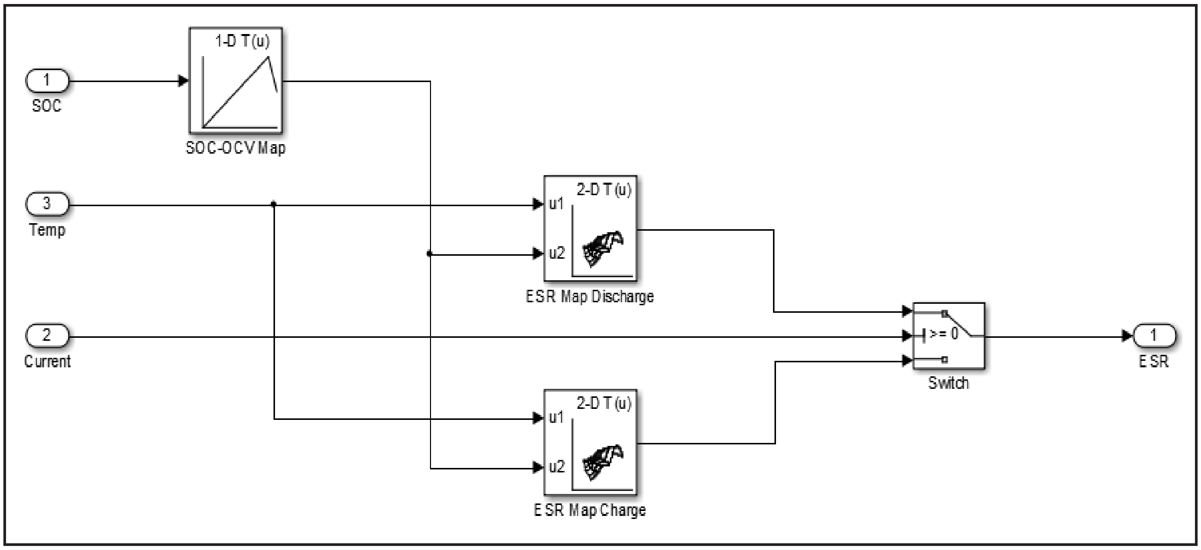

Figure 60. Computing ESR Subsystem

The data used in the ESR map charge and ESR map discharge lookup tables have been obtained empirically. Prior to thermal testing, the pack was subjected to HPPC tests at four different temperatures, namely -20 °C, 0 °C, 20 °C and 40 °C. In each HPPC test, the pack was subjected to the standard HPPC pulse profile at 10 SOC set points spanning the entire range of the pack. The voltage response obtained in each case was analyzed using the standard prescribed USABC Testing Manual (Idaho National Laboratory, 2010) to obtain the ESR for charge and discharge. These results were then interpolated to obtain the distributions shown in Figure 61 and Figure 62 below. These distributions were then used to populate the two lookup tables used in the model.

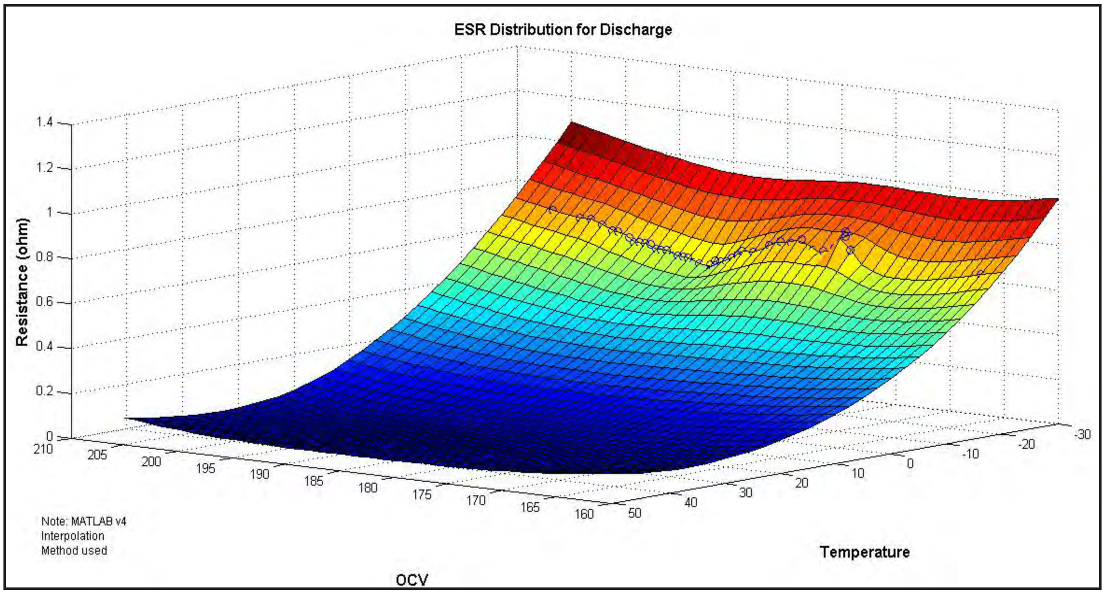

Figure 61. ESR during Discharge vs. Open Circuit Voltage and Temperature

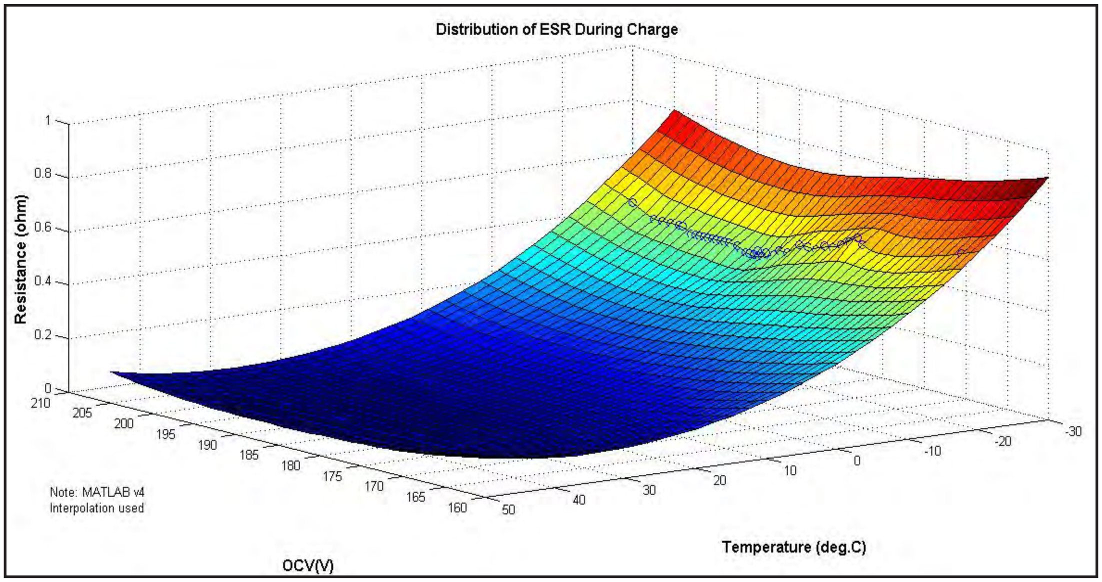

Figure 62. ESR during Charge vs. Open Circuit Voltage and Temperature

Battery Pack Subsystem

This subsystem implements the heat-transfer dynamics for each of the four locations of modules along the length of the cooling plate. Once again, it is assumed, based on experimental observations, that the heat transfer dynamics are symmetrical, and thus simulating the dynamics of only four modules is considered sufficient.

Figure 63 is a schematic illustrating the heat transfer among different regions of the battery pack. This schematic forms the basis of the model used to simulate the heat-transfer dynamics at the pack level.

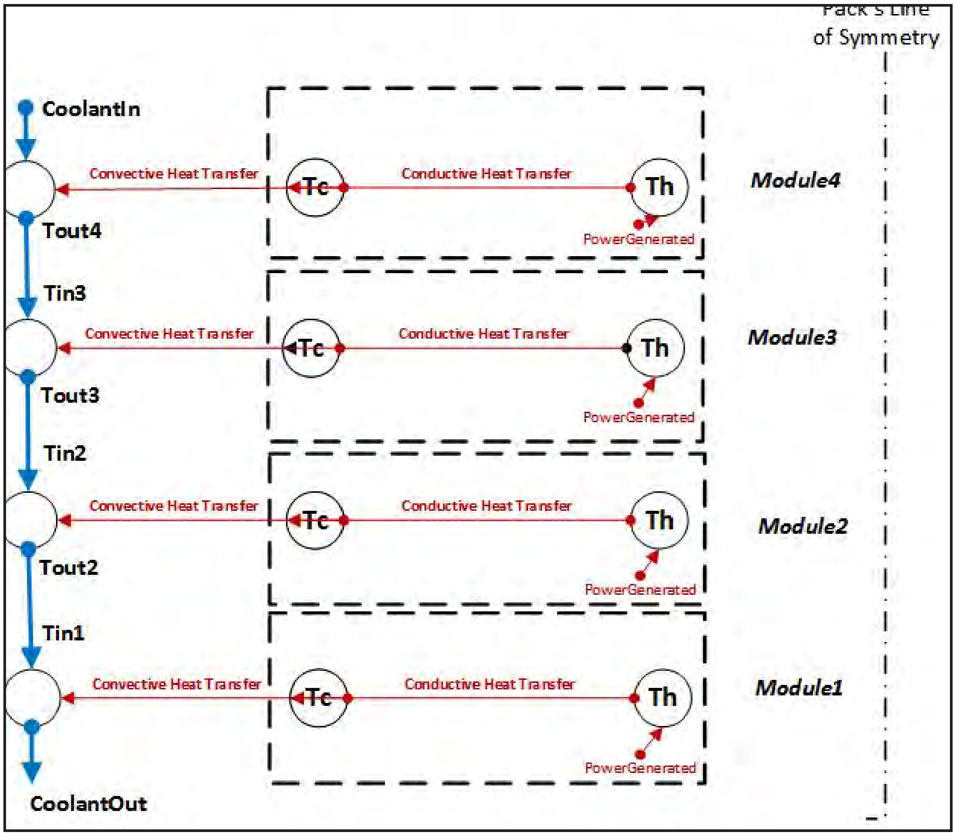

Figure 63. Battery-Pack Level Thermal Model

The subsystem takes the power generated, power removed, and the current at the current time-step as the inputs. It contains four subsystems. Each subsystem models the heat-transfer dynamics of the modules at a different location along the length of the pack. Each subsystem outputs the temperature of the corresponding region of the cooling plate and the temperature of the corresponding hot spot. These two temperatures were chosen as representative outputs because they cover the entire range of temperature values for that module.

Figure 64 shows an overview of the subsystem.

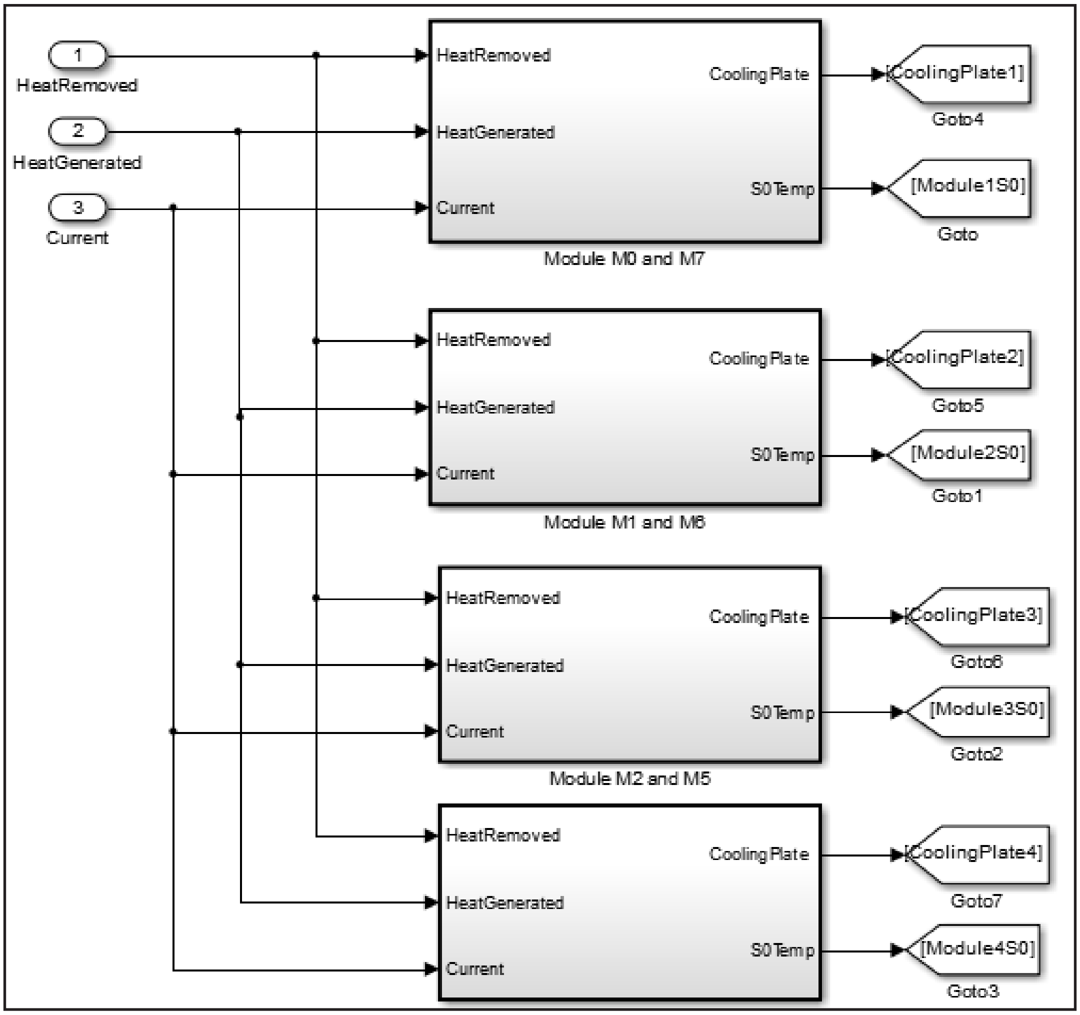

Figure 64. Overview of Battery Pack Subsystem

In every module, the thermal dynamics can be simplified as follows:

- A majority of the heat is generated near the terminals of the module due to Ohmic heat generation. The heat generated in the remainder of the module is negligible. Further, from experimental data, it is clear that a hot spot is located near the terminals of each module. Thus, this model treats the area near the terminals as a heat source. It is assumed that the power generated and calculated from the Ohmic heat generation subsystem is all generated by these heat sources.

- Due to the construction of the modules, heat is conducted away from the above-mentioned hot spots toward the module's heat sink and then into the cooling plate. The zone between the hot spot and the cooling plate is heterogeneous, and it is impossible to reliably obtain a conductive heat-transfer coefficient for this entire region. It is possible to use a simplified version of the Kirchoff's law of heat conduction. It can be said that the conductive heat transfer between the hot spot and the cooling plate is proportional to the temperature difference between the two locations.

- At the cooling plate, there is an input of heat from the heat source at the module terminals. There is also an output of heat due to heat extraction by the cooling system. This heat extraction by the cooling system is obtained from the power removed signal, which is an input to this subsystem.

The heat-transfer dynamics in every module are implemented using the model configuration shown in Figure 65, while Figure 66 details the measured cooling plate and module heat capacity values.

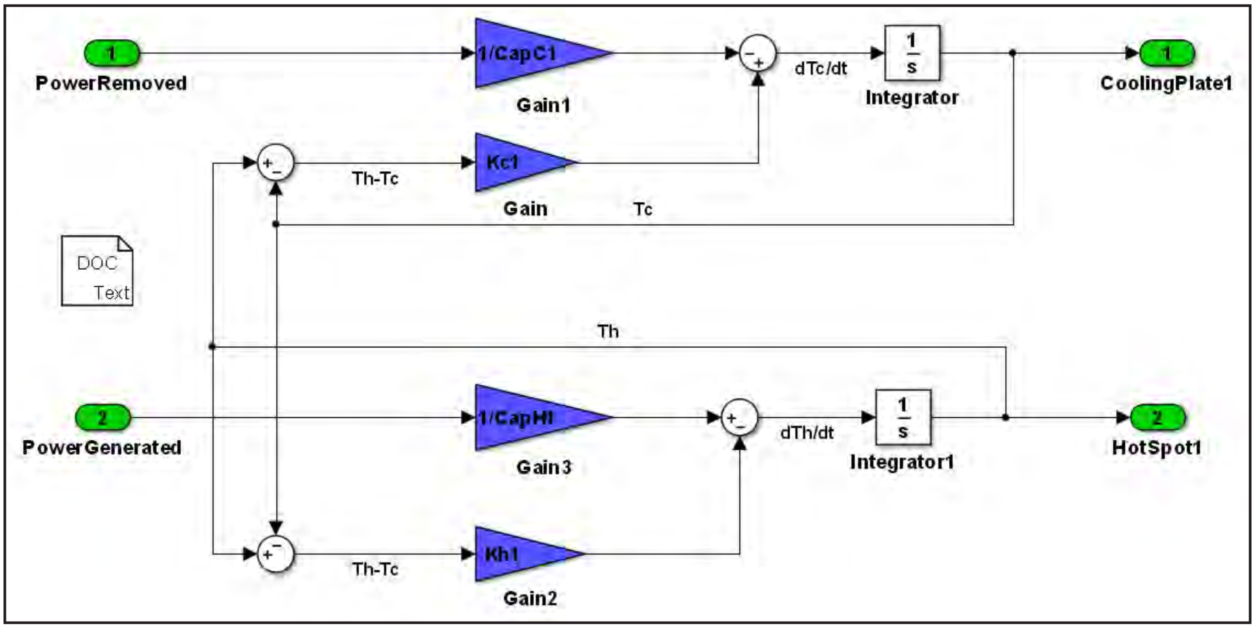

Figure 65. Module Heat Transfer Dynamics

Heat Capacity	[joule / kelvin]
Cooling Plate 1	0.000260192
Cooling Plate 2	0.000244091
Cooling Plate 3	0.000244091
Cooling Plate 4	0.000308835
Module 1	152118.8342
Module 2	168525.7674
Module 3	180846.8161
Module 4	156911.2185

Figure 66. Module Heat Capacity Values

Model Validation

The model is validated against test data recorded during the experiments. To accomplish this, current, SOC, and coolant input temperature profiles recorded during the experiments were used as inputs. The model simulated the evolution of temperatures at all critical locations. The simulated profile was plotted against the measured temperature profile.

The following are some comparative plots. Figure 67 shows a comparison of the measured and simulated temperature response during the transition phase when pack-cycling is stopped and it undergoes forced cooling due to the operational cooling system.

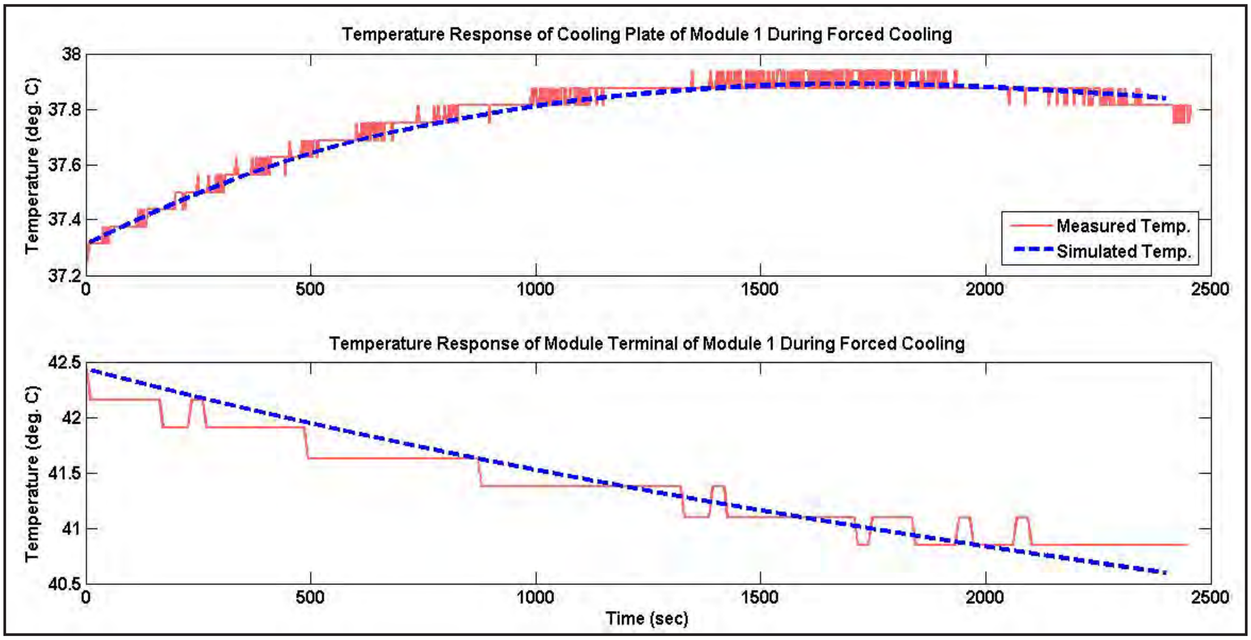

Figure 67. Temperature Responses during Forced Cool-Down

Analogously, Figure 68 shows a comparison of measured and simulated temperature response at the module terminal and corresponding cooling plate during pack cycling.

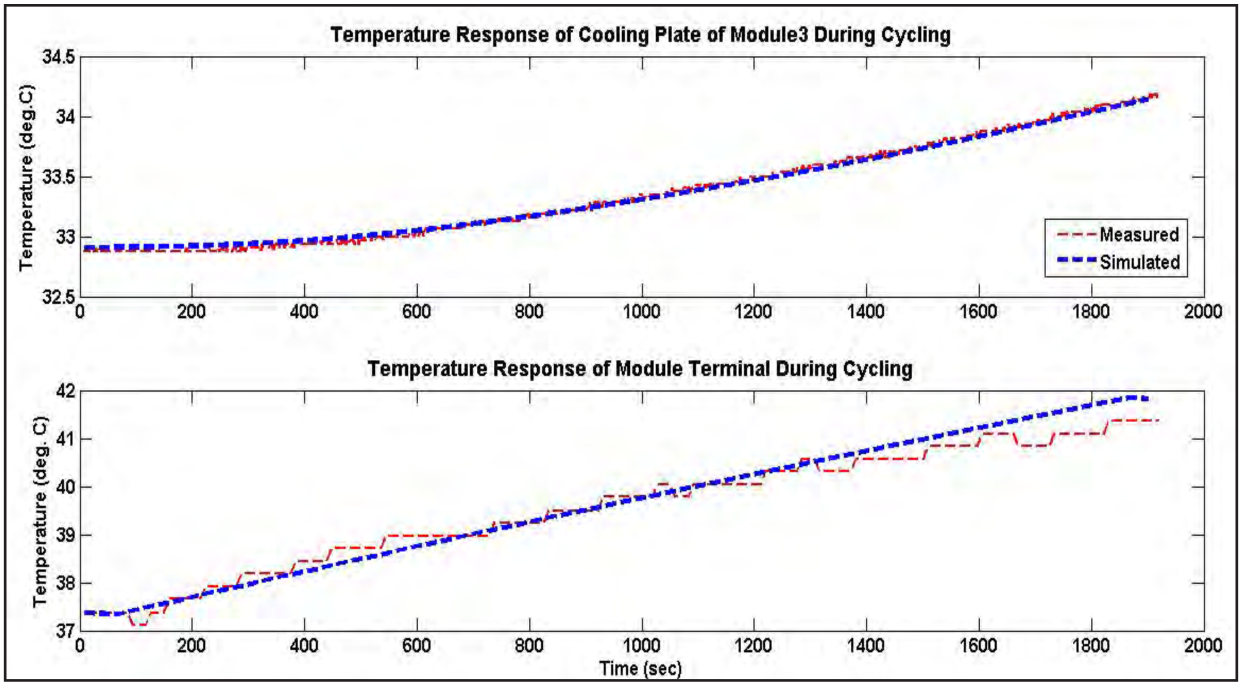

Figure 68. Temperature Response during Pack Cycling

It is clear from both graphs that the model generated from this work can simulate transient temperature responses at all critical locations of the battery system with a high degree of fidelity while maintaining low computational complexity. This model can thus form the basis of a large number of trade-off studies and development of advanced thermal management systems.

Cooling System

This subsystem models the heat extraction performed by the cooling system integrated into the pack. On the pack, the cooling system is architected as a channel machined on a metal plate that is in thermal contact with heat sinks on each module. This plate is referred to as the “cooling plate,” and the channel is referred to as the “cooling tube.” Such a plate is located on both the longer edges of the pack. It has been established through experiments that these two cooling plates behave identically, i.e., the thermal characteristics are symmetrical. Thus, the dynamics of only one side are modeled and the heat extraction effect is doubled. In this model, the coolant is assumed to enter the cooling tube on one end of the longer edge of the pack and leave from the other end.

The cooling tube carries a coolant (50 percent ethylene glycol during the tests). The fluid is driven by a pump controlled over a CAN bus. In the test setup, heat is extracted from the cooling fluid using a radiator.

It has been experimentally observed, as shown in the previous chapter, that there is a temperature gradient along the length of the cooling plate. It is also evident from the evolution of the temperature distribution across the cooling plate that the length of the cooling plate can be divided into approximately four regions of relatively constant temperature. Each of these regions corresponds to the area of the cooling plate in thermal contact with the heat sink of one of the four modules. Further, the region closest to the entry point of the coolant into the cooling tube appears to exhibit the lowest temperature. To capture these dynamics, the heat extraction process is modeled in four units, each corresponding to one of the four regions.

For each unit, the coolant input temperature and the temperature of cooling plate in that specific region are used to calculate the heat removed from that zone and the coolant output temperature. This coolant output temperature is used as the coolant input temperature for the next unit.

This process is repeated until all four units are spanned. The heat removed from each of the four regions is summed to give the total heat removed from the pack per unit of time. The high-level representation of this can be seen in Figure 69.

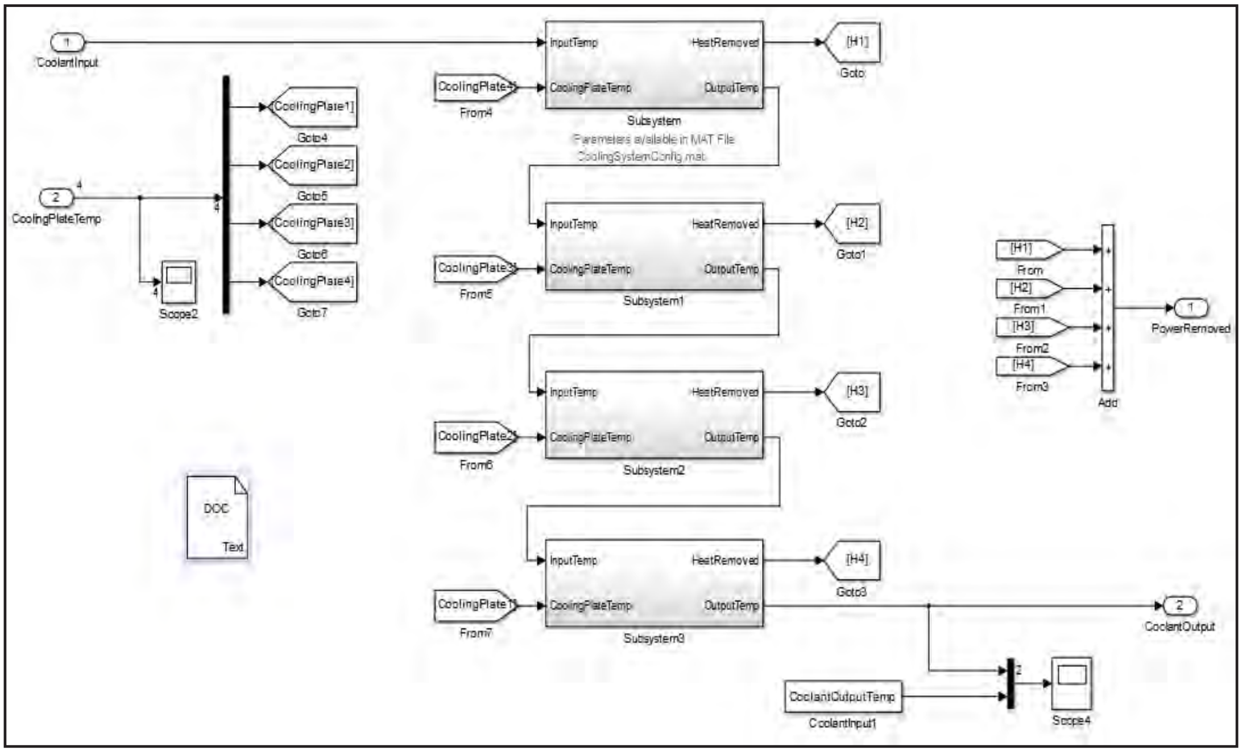

Figure 69. Subsystem Representing Heat Extraction from the Coolant

Each of the four units contains an implementation, as shown in Figure 69. Each unit is modeled as convective heat transfer to the coolant from the cooling tube walls, which are assumed to be at a uniform temperature. The relationships among the cooling plate temperature, coolant input temperature, and coolant output temperature are given by the following:

$$(T_w - T_{out}) = (T_w - T_{in})\, e^{\left(\frac{h_{conv}PL}{\rho C_p f}\right)} \tag{35}$$

where,

T_w = Temperature of cooling tube walls

T_{in} = Coolant temperature at inlet of heat exchange zone

T_{out} = Coolant temperature at outlet of heat exchange zone

h_{conv} = Convective heat transfer coefficient between cooling tube walls and coolant

P = Perimeter of cross section of cooling tube

L = Length of cooling tube

p = Density of coolant

C_p = Heat capacity of coolant

f = Volumetric flow rate of coolant

The Simulink® implementation of this equation is shown in Figure 70.

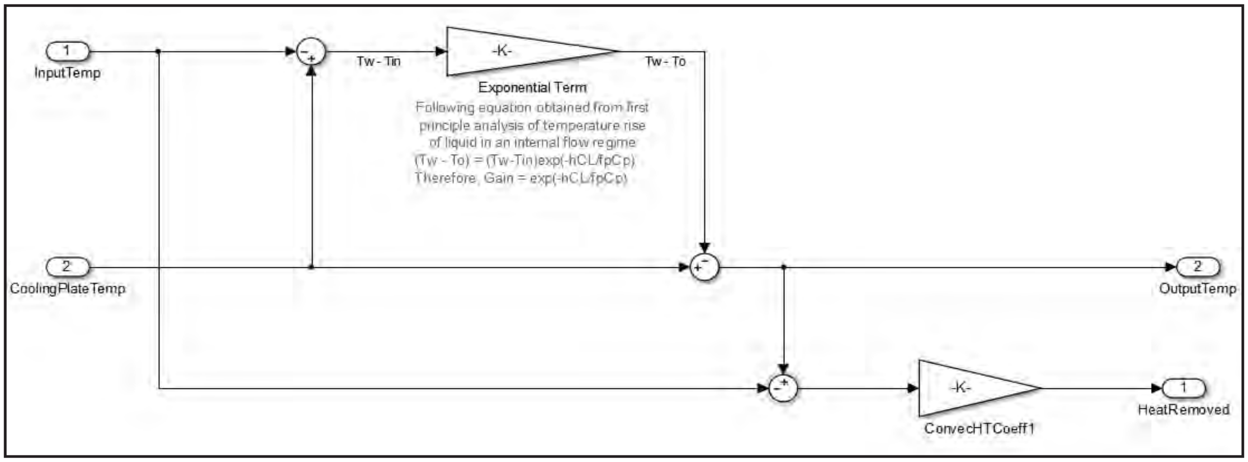

Following equation obtained from first principle analysis of temperature rise of liquid in an internal flow regime
(Tw - To) = (Tw-Tin)exp(-hCL/fpCp)
Therefore, Gain = exp(-hCL/fpCp)

Figure 70. Simulink® Implementation of the Standard Heat-Exchanger

The parameters used in the model are either obtained experimentally or are previously known values. For instance, the convective heat transfer coefficient between the cooling plate and the coolant is obtained from analysis of test data. The perimeter of the cooling tube's cross-section and the length of the cooling tube are known from the system's design specification sheet. In accordance with the system's design specification sheet, the pack was operated with a coolant flow rate of two gallons per minute.

The coolant's density and specific heat capacity are known because a standard coolant is used.

Note that all temperature signals are in degrees Celsius, and all heat-removed signals are in Watts.

ABBREVIATIONS AND ACRONYMS

A / Ah	Ampere / Ampere-Hour
BMS	Battery Management System
CAN	Controller Area Network
C	Degrees Celsius
C Rate	Battery Hourly Power Rate
DC	Direct Current
DP	Dual Polarization
DST	Dynamic Stress Test
EIS	Electrochemical Impedance Spectroscopy
EOL	End of Life
ESR	Effective Series Resistance
ESS	Energy Storage System
EV	Electric Vehicle
Hz	Hertz, a unit of frequency
kW / kWh	kiloWatt / kiloWatt-hour
LFP	Lithium Ion Phosphate
LTO	Lithium Titanate Oxide
mV	micro-Volt
NCA	Lithium Cobalt Oxide
OCV	Open Circuit Voltage
PHEV	Plug-in Hybrid Electric Vehicle
RTD	Resistance Temperature Detectors
RC	Resistor-Capacitor
VAC	Variable Alternating Current
V	Volt

APPENDIX A: AEROVIRONMENT TEST SCRIPTS AND FUNCTIONS

```
/*%%%%%%%%%%%%%%%%%%%%%%%%%%%%%%%%%%%%%%%%%%%%%%%%%%%%%%%%%%%%%%%%%%%%%%%%
% CAN Communication Setup                       %
%%%%%%%%%%%%%%%%%%%%%%%%%%%%%%%%%%%%%%%%%%%%%%%%%%%%%%%%%%%%%%%%%%%%%%%%*/

/* CAN Messaging Setup (CAN1 should be set to 125kbps) */
/* Bit order is odd......... expect to see motorala, but needs to be set to Intel (odd) */
#request name=CAN1 /* requesting name for CAN port */
#Custom:MSBFirst   /* Motorola type of CAN message for Intel its LSBFirst */

/* USE timerstamp variables */
/* #NoTimestamps */


/* Pack Status Info (ID’s = 50Ah Pack: 0x120h, 60Ah Pack: 0x121h)
/* The following messages are received by ROS */
#CANSetupLink _Min_Cell_Voltage, 0x120, 2, u8
#CANSetupLink _Max_Cell_Voltage, 0x120, 0, u8
#CANSetupLink _Max_Cell_Temperature, 0x120, 5, u8, 0.5, -40.0

/* AV900 Status Message */
/* The following messages are sent by ROS */
#CANSetupEncoding *ABCCurrent,i16,0.01, 0.0
#CANSetupEncoding *ABCVoltage,u16, 0.1, 0.0
#CANSetupEncoding *ABCPower,i16, 0.1, 0.0
#CANSetupEncoding *ABCCommandMode,u8, 1.0, 0.0
#CANSetupEncoding *ABCStatus,u8, 1.0, 0.0
#CANSetupMsg 0x050,8,*ABCCurrent,0,*ABCVoltage,2,*ABCPower,4,*ABCCommandMode,6,*ABCStatus,7

/* AV900 Ah Message */
/* The following messages are sent by ROS */
#CANSetupEncoding *ABCAh,i16,0.01, 0.0
#CANSetupEncoding *ABCAhIn,i16, 0.01, 0.0
#CANSetupEncoding *ABCAhOut,i16, 0.01, 0.0
#CANSetupMsg 0x051,6,*ABCAh,0,*ABCAhIn,2,*ABCAhOut,4

/* AV900 kWh Message */
/* The following messages are sent by ROS */
#CANSetupEncoding *ABCkWh,i16,0.01, 0.0
#CANSetupEncoding *ABCkWhIn,i16, 0.01, 0.0
#CANSetupEncoding *ABCkWhOut,i16, 0.01, 0.0
#CANSetupMsg 0x052,6,*ABCkWh,0,*ABCkWhIn,2,*ABCkWhOut,4


/* AV900 Limits_1 Message */
/* The following messages are sent by ROS */
#CANSetupEncoding *ABCVmax,i16, 0.01, 0.0
#CANSetupEncoding *ABCVmin,i16, 0.01, 0.0
#CANSetupEncoding *ABCImax,i16, 0.01, 0.0
#CANSetupEncoding *ABCImin,i16, 0.01, 0.0
#CANSetupMsg 0x053,8,*ABCVmax,0,*ABCVmin,2,*ABCImax,4,*ABCImin,6

/* AV900 Limits_2 Message */
/* The following messages are sent by ROS */
#CANSetupEncoding *ABCPmax,i16, 0.01, 0.0
#CANSetupEncoding *ABCPmin,i16, 0.01, 0.0
#CANSetupEncoding *ABCCommandValue,i16, 0.01, 0.0
#CANSetupMsg 0x054,6,*ABCPmax,0,*ABCPmin,2,*ABCCommandValue,4

/* AV900 Time Message */
/* The following messages are sent by ROS */
#CANSetupEncoding *TestTime,u16, 0.1, 0.0
#CANSetupEncoding *CommandTime,u16, 0.1, 0.0
#CANSetupMsg 0x055,4,*TestTime,0,*CommandTime,2
```

```
/* Script Status Message */
/* The following messages are sent by ROS */
#CANSetupEncoding _log_status,u8, 1.0, 0.0
#CANSetupEncoding _cycle_number,u8, 1.0, 0.0
#CANSetupEncoding CAN_Watchdog,u8, 1.0, 0.0
#CANSetupEncoding delta_time,u16, 0.1, 0.0
#CANSetupMsg 0x060,5,_log_status,0,_cycle_number,1, CAN_Watchdog,2,delta_time,3

/*%%%%%%%%%%%%%%%%%%%%%%%%%%%%%%%%%%%%%%%%%%%%%%%%%%%%%%%%%%%%%%%%%%%%%%%%%*/
```

CAN Watch Dog

```
/*%%%%%%%%%%%%%%%%%%%%%%%%%%%%%%%%%%%%%%%%%%%%%%%%%%%%%%%%%%%%%%%%%%%%%%%%%
%        CAN Watchgog Function                  %
%%%%%%%%%%%%%%%%%%%%%%%%%%%%%%%%%%%%%%%%%%%%%%%%%%%%%%%%%%%%%%%%%%%%%%%%%%%
% Monitors the max cell voltage CAN signal’s time stamp. If that signal %
% isn’t read at least every 5 seconds than the CAN_Watchdog variable %
% will go high indicating a timeout condition                       %
%%%%%%%%%%%%%%%%%%%%%%%%%%%%%%%%%%%%%%%%%%%%%%%%%%%%%%%%%%%%%%%%%%%%%%%%%*/

void CAN_Watchdog_Function()
{
 /* determine current time stamp based on max cell voltage CAN sinal */
 current_time_stamp=CAN1_Max_Cell_Voltage_t;


 /* calculate delta time and determine watchdog status */
 delta_time=TestTime - current_time_stamp;

         if(delta_time < 5)
         {
          CAN_Watchdog=0;
         }

 if(delta_time >= 5)
         {
          CAN_Watchdog=1;
         }
}
/*%%%%%%%%%%%%%%%%%%%%%%%%%%%%%%%%%%%%%%%%%%%%%%%%%%%%%%%%%%%%%%%%%%%%%%%*/
```

Voltage Calculation

```
/*%%%%%%%%%%%%%%%%%%%%%%%%%%%%%%%%%%%%%%%%%%%%%%%%%%%%%%%%%%%%%%%%%%%%%%%%%
%        Calculate Voltages                               %
%%%%%%%%%%%%%%%%%%%%%%%%%%%%%%%%%%%%%%%%%%%%%%%%%%%%%%%%%%%%%%%%%%%%%%%%%%%
% ROS software dosn’t allow for a factor to be greater than 1 in the CAN %
% messaging setup. This function performs cell voltage calculations to %
% apply the factor and offset required for Proterra cell voltage signals %
%%%%%%%%%%%%%%%%%%%%%%%%%%%%%%%%%%%%%%%%%%%%%%%%%%%%%%%%%%%%%%%%%%%%%%%%%*/

void Calculate_Voltages_Function()
{
 /* Calculate Max Cell Voltage */
 Max_Cell_Voltage = ((CAN1_Max_Cell_Voltage*4)+1900);

 /* Calculate Max Cell Voltage */
 Min_Cell_Voltage = ((CAN1_Min_Cell_Voltage*4)+1900);
}
/*%%%%%%%%%%%%%%%%%%%%%%%%%%%%%%%%%%%%%%%%%%%%%%%%%%%%%%%%%%%%%%%%%%%%%%%*/
```

Timer

```
/*%%%%%%%%%%%%%%%%%%%%%%%%%%%%%%%%%%%%%%%%%%%%%%%%%%%%%%%%%%%%%%%%%%%%%%%%%
%        Timmed Functions                        %
%%%%%%%%%%%%%%%%%%%%%%%%%%%%%%%%%%%%%%%%%%%%%%%%%%%%%%%%%%%%%%%%%%%%%%%%%%%
% Run other functions based on the Timer, TimerID         %
% /* Setup and Start Timers to send CAN Messages */ %
%        TimerID=StartTimer(100,Timmed_Functions());      %
%%%%%%%%%%%%%%%%%%%%%%%%%%%%%%%%%%%%%%%%%%%%%%%%%%%%%%%%%%%%%%%%%%%%%%%%%*/

void Timmed_Functions()
{
         CAN_Watchdog_Function();
         Calculate_Voltages_Function();
         CAN1PostMsg(0x050);
         CAN1PostMsg(0x051);
         CAN1PostMsg(0x052);
         CAN1PostMsg(0x053);
         CAN1PostMsg(0x054);
         CAN1PostMsg(0x055);
         CAN1PostMsg(0x060);
}
/*%%%%%%%%%%%%%%%%%%%%%%%%%%%%%%%%%%%%%%%%%%%%%%%%%%%%%%%%%%%%%%%%%%%%%%%*/
```

HPPC Test Script

```
/*%%%%%%%%%%%%%%%%%%%%%%%%%%%%%%%%%%%%%%%%%%%%%%%%%%%%%%%%%%%%%%%%%%%%%%%%%
% Pennsylvania State University        %
%%%%%%%%%%%%%%%%%%%%%%%%%%%%%%%%%%%%%%%%%%%%%%%%%%%%%%%%%%%%%%%%%%%%%%%%%%%
 COPYRIGHT 2013
 Pennsylvania State University
 Pennsylvania Transportation Institute
 201 Transportation Research Building
 University Park, PA 16802
%%%%%%%%%%%%%%%%%%%%%%%%%%%%%%%%%%%%%%%%%%%%%%%%%%%%%%%%%%%%%%%%%%%%%%%%%%%

 FILENAME: HPPC (50Ah)

 DESCRIPTION: This script will charge the a 50Ah LTO 80 cell System
          based on information downloaded from the manufacturers website

 REFERENCES: Include any references used for your script if applicable.
          1.AV-900 Manual 06503-03E]
                   2.ROS Scripting Manual 06633-03_A
                   3.AeroVironment CAN Programming Insert
                   4. Web Data

 DATE AUTHOR REVISION
 09-July-2013 Timothy Cleary New Version
 16-July-2013      Timothy Cleary Edited to run 50Ah Pack

%%%%%%%%%%%%%%%%%%%%%%%%%%%%%%%%%%%%%%%%%%%%%%%%%%%%%%%%%%%%%%%%%%%%%%%%%*/


/*%%%%%%%%%%%%%%%%%%%%%%%%%%%%%%%%%%%%%%%%%%%%%%%%%%%%%%%%%%%%%%%%%%%%%%%%%
% Variable Initialization                                 %
%%%%%%%%%%%%%%%%%%%%%%%%%%%%%%%%%%%%%%%%%%%%%%%%%%%%%%%%%%%%%%%%%%%%%%%%%*/

#global float current_time_stamp = 0;
#global float previous_time_stamp = 0;
#global float delta_time = 0;
#global int CAN_Watchdog = 0;
#global float pack_voltage = 0;

#global int TimerID = 0;
#global int i = 0;
```

```
#global int Max_Cell_Voltage = 0;
#global int Min_Cell_Voltage = 0;

#global int CAN1_log_status = 0; /* init log status */
#global int CAN1_phase = 0; /* init phase                  */
#global int CAN1_cycle_number = 0; /* init phase                      */
#global int max_temp_limit = 55; /* max cell temp limit = 55C */


/*%%%%%%%%%%%%%%%%%%%%%%%%%%%%%%%%%%%%%%%%%%%%%%%%%%%%%%%%%%%%%%%%%%%%%%%%%%%%%%%*/

All functions above inserted here

/*%%%%%%%%%%%%%%%%%%%%%%%%%%%%%%%%%%%%%%%%%%%%%%%%%%%%%%%%%%%%%%%%%%%%%%%%%%%%%%%%%
%         Main Script                             %
%%%%%%%%%%%%%%%%%%%%%%%%%%%%%%%%%%%%%%%%%%%%%%%%%%%%%%%%%%%%%%%%%%%%%%%%%%%%%%%%%%%%*/

void main()
{


/* Setup and Start Timers to send CAN Messages */
          TimerID=StartTimer(100,Timmed_Functions());

/* This list sends the limit values to the machine at the start of the test */
/* When the values hit the limit the test stops;The AV900 will just hold that */
/* value no matter what is requested until it decreases within range. */

          ABCVmin = 120;
          ABCVmax = 232;
          ABCImin = -380;
          ABCImax = 380;
          ABCPmin = -80;
          ABCPmax = 90;

          ChangeLimits();


/* Start Logging (requests logging to toggle on in CANoe) */
          CAN1_log_status = 1;

/* Battery Charging starts here */
          /* Redefine Max Temp Limit */
          max_temp_limit = 55;

/* Phase 1 */
/* Wait 30 Seconds */
          CAN1_phase= 1;
          Standby(0, CommandTime>5);

while(i<20)
{

/* Phase 2 */
/* Discharge Pulse */
          CAN1_phase= 2;
          Current(-375,CommandTime > 10||Min_Cell_Voltage <= 1950||Min_Cell_Voltage == 2912||CAN_
          Watchdog != 0 || CAN1_Max_Cell_Temperature > max_temp_limit);
          Standby(0, CommandTime>40);

/* Phase 3 */
/* Charge Pulse */
          CAN1_phase= 3;
          Current(375,CommandTime > 10||Max_Cell_Voltage >= 2900||Max_Cell_Voltage == 2916||CAN_
          Watchdog != 0 || CAN1_Max_Cell_Temperature > max_temp_limit);
          Standby(0, CommandTime>40);

/* Phase 4 */
/* Discharge 10% SOC */
          CAN1_phase= 4;
          Current(-50,CommandTime > 360||Min_Cell_Voltage <= 1950||CAN_Watchdog != 0 || CAN1_Max_
```

```
         Cell_Temperature > max_temp_limit);

/* Wait 60 min */
         CAN1_phase= 1;
         Standby(0, CommandTime>1800);
i=i+1;
}

/* Stop Logging (requests logging to toggle on in CANoe) */
         CAN1_log_status = 5;


/* Battery Charging Complete */

/* wait for temperature to recover!!*/

/* Stop Timers */
         StopTimer(TimerID);

/* End Test */
}

/*%%%%%%%%%%%%%%%%%%%%%%%%%%%%%%%%%%%%%%%%%%%%%%%%%%%%%%%%%%%%%%%%%%%%%%%%%%%%%%
% Pennsylvania State University        %
%%%%%%%%%%%%%%%%%%%%%%%%%%%%%%%%%%%%%%%%%%%%%%%%%%%%%%%%%%%%%%%%%%%%%%%%%%%%%*/
```

Charge Profile

```
/*%%%%%%%%%%%%%%%%%%%%%%%%%%%%%%%%%%%%%%%%%%%%%%%%%%%%%%%%%%%%%%%%%%%%%%%%%%%%%%
% Pennsylvania State University        %
%%%%%%%%%%%%%%%%%%%%%%%%%%%%%%%%%%%%%%%%%%%%%%%%%%%%%%%%%%%%%%%%%%%%%%%%%%%%%%%%
 COPYRIGHT 2013
 Pennsylvania State University
 Pennsylvania Transportation Institute
 201 Transportation Research Building
 University Park, PA 16802
%%%%%%%%%%%%%%%%%%%%%%%%%%%%%%%%%%%%%%%%%%%%%%%%%%%%%%%%%%%%%%%%%%%%%%%%%%%%%%%%

 FILENAME: Charge (50Ah)

 DESCRIPTION: This script will charge the LTO 80 cell System
          based on information downloaded from the manufacturers website

 REFERENCES: Include any references used for your script if applicable.
          1.AV-900 Manual 06503-03E]
                   2.ROS Scripting Manual 06633-03_A
                   3.AeroVironment CAN Programming Insert
                   4. Web Data

 DATE AUTHOR REVISION
 09-July-2013 Timothy Cleary New Version

%%%%%%%%%%%%%%%%%%%%%%%%%%%%%%%%%%%%%%%%%%%%%%%%%%%%%%%%%%%%%%%%%%%%%%%%%%%%*/

Variable initialization and functions as seen above as well as all functions are inserted here.


/*%%%%%%%%%%%%%%%%%%%%%%%%%%%%%%%%%%%%%%%%%%%%%%%%%%%%%%%%%%%%%%%%%%%%%%%%%%%%%%
%        Main Script                            %
%%%%%%%%%%%%%%%%%%%%%%%%%%%%%%%%%%%%%%%%%%%%%%%%%%%%%%%%%%%%%%%%%%%%%%%%%%%%*/

void main()
{


/* Setup and Start Timers to send CAN Messages */
         TimerID=StartTimer(100,Timmed_Functions());

/* This list sends the limit values to the machine at the start of the test */
```

```
/* When the values hit the limit the test stops;The ABC will just hold that */
/* value no matter what is requested until it decreases within range. */

         ABCVmin = 120;
         ABCVmax = 232;
         ABCImin = -50;
         ABCImax = 120;
         ABCPmin = -30;
         ABCPmax = 30;

         ChangeLimits();


/* Start Logging (requests logging to toggle on in CANoe) */
         CAN1_log_status = 1;

/* Battery Charging starts here */
         /* Redefine Max Temp Limit */
         max_temp_limit = 55;

/* Phase 1 */
/* Wait 30 Seconds */
         CAN1_phase= 1;
         Standby(0, CommandTime>30);

/* Phase 2 */
/* Charge at 100 Amps until Max_Cell_Voltage => 2700mV */
         CAN1_phase= 2;
         Current(100,Max_Cell_Voltage >= 2700||CAN_Watchdog != 0 || CAN1_Max_Cell_Temperature >
max_temp_limit);
         Standby(0, CommandTime>5);

/* Phase 3 */
/* Charge at 50 Amps until Max_Cell_Voltage => 2750V */
         CAN1_phase= 3;
         Current(50,Max_Cell_Voltage >= 2750||CAN_Watchdog != 0 || CAN1_Max_Cell_Temperature >
max_temp_limit);
         Standby(0, CommandTime>5);

/* Phase 4 */
/* Charge at 25 Amps until Max_Cell_Voltage => 2800V */
         CAN1_phase= 4;
         Current(25,Max_Cell_Voltage >= 2800||CAN_Watchdog != 0 || CAN1_Max_Cell_Temperature >
max_temp_limit);
         pack_voltage = ABCVoltage;

/* Phase 5 */
/* Constant Voltage Charge until current is less than 5 amps */
         CAN1_phase= 5;
         Voltage(pack_voltage,CommandTime> 3600||ABCCurrent<5||Max_Cell_Voltage >= 2900||CAN_
         Watchdog != 0 || CAN1_Max_Cell_Temperature > max_temp_limit);

/* Wait 30 Seconds */
         CAN1_phase= 1;
         Standby(0, CommandTime>30);


/* Stop Logging (requests logging to toggle on in CANoe) */
         CAN1_log_status = 5;

/* Battery Charging Complete */

/* Stop Timers */
         StopTimer(TimerID);

/* End Test */
}

/*%%%%%%%%%%%%%%%%%%%%%%%%%%%%%%%%%%%%%%%%%%%%%%%%%%%%%%%%%%%%%%%%%%%%%%%%%%%%%%%%%%%%%%%%%%%%%%%%%%%
% Pennsylvania State University        %
%%%%%%%%%%%%%%%%%%%%%%%%%%%%%%%%%%%%%%%%%%%%%%%%%%%%%%%%%%%%%%%%%%%%%%%%%%%%%%%%%%%%%%%%%%%%%%%%%%%*/
```

APPENDIX B: ESR TABLES

ESR TABLES

-20 Degrees Celsius		
OCV [Volts]	ESR Charge [Ohms]	ESR Discharge [Ohms]
201.5000	0.5200	0.7600
199.0000	0.4800	0.7400
198.0000	0.4800	0.7400
197.0000	0.4800	0.7200
196.0000	0.4800	0.7000
195.5000	0.4800	0.7000
194.5000	0.4600	0.6800
194.0000	0.4600	0.6596
193.5000	0.4600	0.6600
193.0000	0.4600	0.6600
192.5000	0.4600	0.6600
192.0000	0.4600	0.6400
191.5000	0.4600	0.6400
191.0000	0.4600	0.6400
190.5000	0.4600	0.6200
190.0000	0.4600	0.6200
189.5000	0.4400	0.6200
189.0000	0.4600	0.6200
188.5000	0.4400	0.6000
188.0000	0.4400	0.6000
188.0000	0.4400	0.6000
188.0000	0.4400	0.6000
187.5000	0.4200	0.5800
187.5000	0.4400	0.5800
187.0000	0.4400	0.6000
187.0000	0.4400	0.5800
187.0000	0.4200	0.6000
186.5000	0.4400	0.6000
186.5000	0.4600	0.6200
186.0000	0.4400	0.6200
185.5000	0.4600	0.6200
185.0000	0.4400	0.6400
184.5000	0.4600	0.6600
184.0000	0.4800	0.6800
183.0000	0.4800	0.6800
181.5000	0.5200	0.7200
180.5000	0.5200	0.7400
179.5000	0.5200	0.7400

178.5000	0.5400	0.7600
177.5000	0.5400	0.7200
176.5000	0.5600	0.7200
175.5000	0.5800	0.7400
174.5000	0.6000	0.8000
174.5000	0.6000	0.8200
174.0000	0.5800	0.7400
162.0000	0.6400	0.7000

20 Degrees Celsius

OCV [Volts]	ESR Charge [Ohms]	ESR Discharge [Ohms]
196.5000	0.0600	0.0640
192.5000	0.0587	0.0627
189.5000	0.0600	0.0640
187.5000	0.0587	0.0640
186.0000	0.0600	0.0693

40 Degrees Celsius

OCV [Volts]	ESR Charge [Ohms]	ESR Discharge [Ohms]
196.5000	0.0480	0.0493
192.5000	0.0467	0.0480
189.5000	0.0480	0.0493
187.0000	0.0480	0.0493
186.0000	0.0467	0.0493
185.5000	0.0480	0.0520
182.5000	0.0520	0.0587
176.5000	0.0560	0.0560
171.5000	0.0573	0.0573

EQUIVALENT CIRCUIT PARAMETERS

Temp	SOC	Ra	Ca	Rc	Cc
-20	0.514926	0.1909	23.411	0.22316	203.51
-20	0.59305	0.0905	57.826	0.18348	181.28
-20	0.734068	0.1535	36.142	0.16788	214.76
-20	0.827918	0.0184	26.996	0.20006	211.85
-20	0.921656	0.4192	44.103	0.11054	5726.6

-20	0.342734	0.3208	9.9442	0.25056	48.375
-20	0.405272	0.2375	16.405	0.24353	119.16
20	0.937298	0.0134	298.44	0.02291	1887.1
20	0.82792	0.0117	320.79	0.013782	2042.5
20	0.73407	0.0165	297.51	0.024937	4051.4
20	0.60868	0.0146	282.35	0.013273	1727.6
20	0.51493	0.019	229.92	0.038952	4153.2
40	0.131698	0.0246	109.8	0.058811	7203
40	0.232398	0.0242	207.89	0.042464	12199
40	0.333098	0.0205	235.4	0.03255	11025
40	0.433798	0.0142	296.02	0.022281	4205.2
40	0.534498	0.014	309.54	0.011296	3158.6
40	0.635198	0.0113	354.31	0.010301	2645.8
40	0.735898	0.0099	436.17	0.010394	2446.6
40	0.836598	0.0102	437.13	0.010403	2456.5
40	0.937298	0.0101	468.56	0.008193	2146.6

BIBLIOGRAPHY

Hongwen He, R. X. (2011). Evaluation of Lithium-Ion Battery Equivalent Circuit Models. *Energies*, 582-598.

Huria, T., M. Ceraolo, J. Gazzarri, & R. Jackey, (2013). Simplified Extended Kalman Filter Observer for SOC Estimation of Commercial Power-Oriented LFP Lithium Battery Cells. *SAE Technical Paper 2013-01-1544*.

Idaho National Laboratory (2010, December). *Battery Test Manual for Plug-In Hybrid Electric Vehicles*.

Jackey, R., M. Saginaw, P. Sanghvi, J. Gazzari, T. Huria, & M. Ceraolo (2013). Battery Model Parameter Estimation Using a Layered Technique: An Example Using Lithium Iron Phosphate Cell. *SAE Technical Paper 2013-01-1547*.

Lu, J. e. (2012). Single Crystalline Lithium Titanate Nanostructure with Enhanced Rate Performance for Lithium Ion Battery. *Journal of Power Sources*, 246-252.

Mathworks (n.d.). Matlab, Simulink and xPC. Natick, MA, USA.

Maxim Integrated (2008). *DS18B20 Programmable Resolution 1-Wire Digital Thermometer.* San Jose, CA 95134: Maxim Integrated Products, Inc.

Piller, S., M. Perrin, & A. Jossen (2001). Methods of State of Charge Determination and their Applications. *Journal of Power Sources* 96 (1), 113-120.

Plett, G. (2004). Extended Kalman Filtering for Battery Management Systems of LiPB based HEV Battery Packs. Part3. State and Parameter Estimation. *Journal of Power Sources* 134 (2), 277-292.

Pop, V., H. Bergveld, P. Notten, & P. Regtien (2005). State-of-the-art of Battery State-of-charge Determination. *Measurement Science and Technology* 16 R93.

Rahmoun, A., H. Biechl, & A. Rosin (2012). State of Charge Estimation of Li-ion Batteries Based on Equivalent Circuit Diagrams and the Application of a Kalman Filter. Electric Power Quality and Supply Reliability Conference, June 11-13, Tartu, Estonia (pp. 1-4). IEEE.

Rahn, C. D., & C-Y Wang (2013). Battery Systems Engineering. Wiley.

Robyn Jackey, M. S. (2013). Battery Model Parameter Estimation Using a Layered Technique: An Example Using a Lithium Iron Phosphate Cell. *SAE 2013-01-1547*, 1-14.

Saha, B., & K. Goebel (2009). Modeling Li-ion Battery Capacity Depletion in a Particle Filtering Framework. *Proceedings, Annual Conference of the Prognostics and*

Health Management Society, San Diego, CA September 27 – October 1, 2009.

Simon, D. (2006). *Optimal State Estimation - Kalman, H-inifinty, and Nonlinear Approaches.* Wiley.

Smith, K., D. Rahn, & C. Wang. (2010). Model Based Electro-Chemical Estimation of Li-Ion Batteries. Proceedings of *IEEE International Conference on Control Applications,* pp. 714-719.

The MathWorks. (2013). *Least-Squares Algorithm*. Retrieved from The MathWorks Documentation Center: http://www.mathworks.com/help/optim/ug/least-squares-model-fitting-algorithms.html#brrzgus

USABC. (1996). Electric Vehicle Battery Test Procedures Manual. United States Council for Automative Research, LLC.

Vector CANtech, Inc. (n.d.). CANoe / CANcaseXL. Novi, Michigan, USA.

Zhang, C., J. Liu, S. Sharkh, & C. Zhang (2009). Identification of Dynamic Model Parameters for Li-ion Batteries used in Hybrid Electric Vehicles. *International Symposium on Electric Vehicles (ISEV)*, (p. 11). Beijing, China.

ABOUT THE AUTHORS

TIMOTHY CLEARY

Timothy Cleary is the director of the Battery Application Technology Testing & Energy Research Laboratory (BATTERY) at the Larson Institute at Pennsylvania State University.

Mr. Cleary earned his B.Sc. and M.S. degrees in mechanical engineering from Penn State. He was involved in the U.S. DOE-sponsored Advanced Vehicle competitions for five years, culminating in his service as team leader for the 2007-2008 competition. In 2009-2010, he was a vehicle systems and simulation contracted engineer supporting U.S. DOE research in pluggable hybrid electric vehicles. In 2010-2011 he gained Top Secret security clearance and assisted the U.S. Army's Seeker Effects Laboratory in performing infrared countermeasure testing. He concentrates his research in battery system development and application testing for advance chemistry automotive batteries ranging from starter to full electric buses.

HARSHAD KUNTE

Harshad Kunte is a systems design architect engineer for Tesla Motors. He earned a master's degree in mechanical engineering at Pennsylvania State University in May 2014 with a focus on control systems engineering. His research interests are in battery systems modeling and control, primarily for electric and hybrid vehicles. At Penn State's Larson Institute, he served the BATTERY Lab as a research assistant and contributed to its extensive work in testing, modeling, and verification of large-format battery systems.

During undergraduate school, he was deeply involved with a team that developed plug-in electric auto cross race cars. He is experienced in working with and leading teams to develop large-format Li-ion battery systems. Recently, he worked with The MathWorks, Inc. as an engineer on the Control Design and Automation team and possesses strong skills in model-based design and systems engineering using MATLAB and Simulink®.

JAMES A. KREIBICK

James A. Kreibick is a graduate student in electrical engineering at Pennsylvania State University. His interests focus around control systems and power systems. His role in this study included testing setup and data acquisition during battery testing. He has also been actively involved in the Penn State Advanced Vehicle team, including participation in the EcoCAR 2 competition sponsored by General Motors and the Argonne National Laboratory. His role in the team was to improve and develop control algorithms for vehicle development.

PEER REVIEW

San José State University, of the California State University system, and the MTI Board of Trustees have agreed upon a peer review process required for all research published by MNTRC. The purpose of the review process is to ensure that the results presented are based upon a professionally acceptable research protocol.

Research projects begin with the approval of a scope of work by the sponsoring entities, with in-process reviews by the MTI Research Director and the Research Associated Policy Oversight Committee (RAPOC). Review of the draft research product is conducted by the Research Committee of the Board of Trustees and may include invited critiques from other professionals in the subject field. The review is based on the professional propriety of the research methodology.

MTI FOUNDER

Hon. Norman Y. Mineta

MTI/MNTRC BOARD OF TRUSTEES

Founder, Honorable Norman Mineta (Ex-Officio)
Secretary (ret.), US Department of Transportation
Vice Chair
Hill & Knowlton, Inc.

Honorary Chair, Honorable Bill Shuster (Ex-Officio)
Chair
House Transportation and Infrastructure Committee
United States House of Representatives

Honorary Co-Chair, Honorable Peter DeFazio (Ex-Officio)
Vice Chair
House Transportation and Infrastructure Committee
United States House of Representatives

Chair, Stephanie Pinson (TE 2015)
President/COO
Gilbert Tweed Associates, Inc.

Vice Chair, Nuria Fernandez (TE 2014)
General Manager/CEO
Valley Transportation Authority

Executive Director, Karen Philbrick, Ph.D.
Mineta Transportation Institute
San José State University

Thomas Barron (TE 2015)
Executive Vice President
Strategic Initiatives
Parsons Group

Joseph Boardman (Ex-Officio)
Chief Executive Officer
Amtrak

Donald Camph (TE 2016)
President
Aldaron, Inc.

Anne Canby (TE 2014)
Director
OneRail Coalition

Grace Crunican (TE 2016)
General Manager
Bay Area Rapid Transit District

William Dorey (TE 2014)
Board of Directors
Granite Construction, Inc.

Malcolm Dougherty (Ex-Officio)
Director
California Department of Transportation

Mortimer Downey* (TE 2015)
Senior Advisor
Parsons Brinckerhoff

Rose Guilbault (TE 2014)
Board Member
Peninsula Corridor Joint Powers Board (Caltrain)

Ed Hamberger (Ex-Officio)
President/CEO
Association of American Railroads

Steve Heminger (TE 2015)
Executive Director
Metropolitan Transportation Commission

Diane Woodend Jones (TE 2016)
Principal and Chair of Board
Lea+Elliot, Inc.

Will Kempton (TE 2016)
Executive Director
Transportation California

Jean-Pierre Loubinoux (Ex-Officio)
Director General
International Union of Railways (UIC)

Michael Melaniphy (Ex-Officio)
President & CEO
American Public Transportation Association (APTA)

Jeff Morales (TE 2016)
CEO
California High-Speed Rail Authority

David Steele, Ph.D. (Ex-Officio)
Dean, College of Business
San José State University

Beverley Swaim-Staley (TE 2016)
President
Union Station Redevelopment Corporation

Michael Townes* (TE 2014)
Senior Vice President
Transit Sector
HNTB

Bud Wright (Ex-Officio)
Executive Director
American Association of State Highway and Transportation Officials (AASHTO)

Edward Wytkind (Ex-Officio)
President
Transportation Trades Dept., AFL-CIO

(TE) = Term Expiration or Ex-Officio
* = Past Chair, Board of Trustee

Directors

Karen Philbrick, Ph.D.
Executive Director

Hon. Rod Diridon, Sr.
Emeritus Executive Director

Peter Haas, Ph.D.
Education Director

Donna Maurillo
Communications Director

Brian Michael Jenkins
National Transportation Safety and Security Center

Asha Weinstein Agrawal, Ph.D.
National Transportation Finance Center

MNTRC
MINETA NATIONAL TRANSIT
RESEARCH CONSORTIUM

SAN JOSÉ STATE
UNIVERSITY

Funded by U.S. Department of
Transportation